

BIO-INSPIRED CRYSTAL GROWTH AS A ROUTE TOWARDS TUNING
ELECTROMAGNETIC PROPERTIES

A Dissertation

Presented to the Faculty of the Graduate School
of Cornell University

In Partial Fulfillment of the Requirements for the Degree of
Doctor of Philosophy

by

Abby Rachel Goldman

May 2019

© 2019 Abby Rachel Goldman

BIO-INSPIRED CRYSTAL GROWTH AS A ROUTE TOWARDS TUNING ELECTROMAGNETIC PROPERTIES

Abby Rachel Goldman, Ph. D.

Cornell University 2019

Organisms routinely produce minerals, called biominerals, with altered materials properties compared to geologic or traditional lab-grown crystals that are suited to the organism's needs. By manipulating the mineral growth, the organisms can alter the crystal structure, shape, orientation, and composition, which collectively determine the material's properties. For example, the mollusk grows its calcium carbonate shell in a gel-like organic template, helping transform the fragile mineral into a stronger material that is hard to break. In another example, a certain class of bacteria uses nanoscale confinement to grow a specific size and shape of iron oxide nanoparticles, which the bacteria can use as a compass to navigate along the Earth's magnetic field. By translating these biomineral growth strategies to the laboratory, we can achieve a high degree of control over crystalline architectures in a wider range of materials systems than organisms can produce. Because many magnetic and electronic properties depend strongly on nano- and microstructure, the ability to grow complex crystalline architectures made of magnetic or electronic materials enables new properties.

My Ph.D. research was inspired by the ability of biominerals to form two types of structures: hierarchical structures that are ordered across many length scales and single crystal composites. For the first half of my Ph.D., I developed a model that predicts how control of hierarchical structure, in particular the crystalline texture, can help us engineer harder magnetic materials. I validated this magnetic model for mosaic

crystals of hematite and developed growth pathways for another hierarchically-structured magnetic material, bismuth ferrite. For the second half of my Ph.D., I formed a theoretical framework for how nano- and micro-particles incorporate into single crystals during solution crystal growth. Finally, I developed a generalizable physical confinement-based approach to semiconductor/plasmonic nanoparticle composites for photocatalytic applications.

BIOGRAPHICAL SKETCH

Abby Rachel Goldman was born in Silver Spring, Maryland to her parents, Jay Goldman and Rebecca Salon. With the encouragement of her parents and teachers, Abby's love of science began early. One highlight was winning first place in the fourth-grade science fair. For her project, she studied rust growth on nails, so it's fitting that she basically spent the first half of her Ph.D. also studying rust. In high school, she enjoyed her chemistry and math classes, which led her to her first research experience as a Howard Hughes Medical Institute intern at the National Institutes of Health during her senior year. Though her understanding of the cancer biology and molecular pharmacology research was (and remains) limited, she was captivated by the process of performing real-world research.

Abby arrived at Mount Holyoke College in South Hadley, MA thinking she would pursue chemistry, but upon taking a required physics class for the chemistry major, she immediately switched course. During an introductory physics course, she became fascinated by magnetism and soon after, she joined the lab of Prof. Kathy Aidala simulating the magnetization reversal behavior of nanomagnets.

Upon graduating, Abby traveled to Haifa, Israel on a Fulbright Fellowship for her first major foray into materials science research, fabricating and testing hybrid organic-inorganic solar cells. After leaving Israel, Abby began a Ph.D. program at University of California Santa Barbara in materials science, but after completing one year, decided to leave the program. Abby later decided to return to graduate school, this time at Cornell University in Ithaca, NY in the department of materials science and engineering. At Cornell, she joined Prof. Lara Estroff's research group, where Abby brought her physics perspective both to the understanding the growth of bio-inspired crystals and to measuring their electronic and magnetic properties.

When she wasn't in the lab, which to be honest was a fair amount, Abby was

actively engaging in science outreach, teaching, mentoring and career exploration. Highlights include: starting up and growing participation Destination Imagination, a STEAM-based creativity program for K-12 students, in Central NY, serving as the Chair for the Gordon Research Seminar on Crystal Growth and Assembly, a two-day seminar for graduate students and post-docs prior to the Gordon Research Conference meant to allow for networking and community building, and teaching senior undergraduate Materials Science and Engineering students how to write about their research in Senior Lab and Senior Thesis.

It was through these extracurricular activities that Abby realized that her passions and skills lay in fields at the intersection of science and communication to non-scientist audiences. Therefore, following graduation, Abby will join the Science Technology Policy Institute in Washington, D.C., where she can apply her interdisciplinary materials science background to progressing our nation's science and technology interests.

For my family, Eliad and Shoshana

ACKNOWLEDGMENTS

Thank you to my parents who were great role models for doing work that you are passionate about. To my mom, whose example of how to balance work and parenting (and finishing ones Ph.D.) never made me question that the same would be possible for me. To my dad, who saw my passion for science as a kid and signed me up for *every* weekend workshop, camp, hands-on science day that he could find.

I am also grateful for all of the mentors that I've had along the way, To Mr. Levin, my high school chemistry teacher: you convinced me to take the HHMI NIH internship, despite my concerns that I wouldn't get to hang out with my friends after school. That first internship led me to the second, which led to the third and fourth and ultimately to the Fulbright and to graduate school. To my undergraduate advisor, Kathy Aidala: you embodied being a confident woman in physics and you empowered all your students to feel the same way. To my Fulbright advisor, Gitti Frey: you not only mentored me as I transitioned to a new research field into a more independent researcher, but you, too, were a role model of being a successful scientist and a parent. To my UCSB Ph.D. advisor, Ram Seshadri: you introduced me to a whole new way of thinking about inorganic chemistry and materials science, though what I am most appreciative of is the way you supported me through my decision to leave graduate school. To my committee members, Bruce van Dover and Greg Fuchs: thank you for your willingness to share your time and input, particularly when it came to wildly brainstorming about nanostructured magnets. It was exactly what I'd hoped for in committee members.

To Lara Estroff, my Ph.D. advisor: thank you for being supportive even when I strayed into the land of magnetism or spent too much time pursuing extracurricular activities and for never questioning my “alternative” post-PhD career path. I can honestly say that I left each of our meetings feeling better about my research direction, which to me is one of the ultimate signs of a great advisor.

There are so many other members of the Cornell community who were influential in my time here. The Estroff research group have been the best labmates imaginable, providing camaraderie and support through professional and personal life. Specifically, I must immensely thank Emily Asenath-Smith, who not only performed much of the foundational work upon which my dissertation work expanded, but you also taught me pretty much all of the wet chemistry that I know. If only you knew how often I explain a procedure as “this is the way Emily taught me.” The Cornell MSE administrative staff, in particular Michele Conrad, Kyle Page, and Marissa Porter, and many others have been integral parts of my time here. A big thank you to the amazing CCMR facility managers enabled me to do all of this work.

Thank you also to my original coffee crew, Jennie, Angela and Teresa. I think I learned more by talking about research with you three than from some of our grad classes. To Heather and Ben, my first friends, who made studying for the Q not only bearable, but also sometimes enjoyable.

A huge thank you to my husband, Eliad, for saying that you’d move to Ithaca, NY from sunny Israel, not knowing at all what kind of crazy journey you were agreeing to. You have supported me unconditionally every step of the way with all the

hugs and Wegmans cake that I needed. A final thank you to Shoshana for bringing me such joy during the challenging and stressful undertaking of finishing my Ph.D.

This work was supported by several grants, NSF (DMR-1210304) and DOE (DE-SC0010560). Additionally, this work made use of the Cornell Center for Materials Research Shared Facilities which are supported through the NSF MRSEC program (DMR-1120296). I would also like to acknowledge all of the fellowships that supported me during my Ph.D.: NSF Graduate Research Fellowship Program (GRF, DGE-1144153), the Cornell Provost's Diversity Fellowship and the Cornell MSE Morel Dissertation Fellowship.

TABLE OF CONTENTS

Biographical Sketch.....	iii
Dedication.....	v
Acknowledgements.....	vi
Table of Contents.....	ix
List of Figures.....	xii
List of Tables.....	xiv
Chapter 1	
1.1 Research Background	1
1.2 Dissertation Introduction	2
1.3 Dissertation Overview	3
References	7
Chapter 2	
2.1 Motivation	9
2.2 Biological inspiration for single crystal composites	10
2.3 Theoretical framework for particle incorporation during solution growth ...	16
2.3.1 Crystallization pressure	18
2.4 Using normal forces to oppose crystallization pressure	18
2.4.1 Particles forming a colloidal crystal-like template	19
2.4.2 Particles in a gel matrix	20
2.4.3 Summary and remaining questions: normal forces	24
2.5 Tuning intermolecular forces to create net attractive forces	25
2.5.1 Crystal surfaces in solution	26
2.5.2 Particle surfaces in solution	30
2.5.3 Summary and remaining questions: intermolecular forces	35

2.6 Conclusions	37
References	39
Chapter 3	
3.1 Introduction.....	55
3.2 Experimental Methods.....	60
3.2.1 Materials.....	60
3.2.2 Growth of Cu ₂ O/Au NP composites in track-etched membranes.....	61
3.2.3 Growth of ZnO/Au NP composites in track-etched membranes.....	62
3.2.4 Powder x-ray diffraction.....	62
3.2.5 Scanning electron microscopy.....	62
3.2.6 Transmission electron microscopy.....	63
3.2.7 UV/Vis spectroscopy.....	63
3.3 Results.....	63
3.4 Discussion.....	76
3.5 Conclusion.....	84
References.....	85
Chapter 4	
4.1 Abstract.....	97
4.2 Manuscript.....	97
4.3 Acknowledgements	114
4.4 Supplementary Methods	114
4.4.1 Materials	114
4.4.2 Synthesis	114
4.4.3 Magnetic Characterization	115
4.4.4 Structural and Phase Characterization	116

4.5 Supporting Information	117
References.....	123
Chapter 5	
5.1 Abstract	133
5.2 Introduction	133
5.3 Experimental Methods	134
5.3.1 Materials	134
5.3.2 Methods	135
5.3.3 Characterization	136
5.4 Results	136
5.5 Discussion.....	145
5.6 Conclusions.....	148
5.7 Acknowledgements	149
5.8 Supporting Information.....	150
References.....	153
Chapter 6	
Conclusions	157
References.....	166
Appendix 1	
A.1 Introduction.....	167
A.2 Refining the MA model – The effect of varying mosaicity.....	167
A.2.1 Gel grown mosaic crystals (quasispheres).....	169
A.2.2 Acid-etched, gel grown grown mosaic crystals	172
References	176

LIST OF FIGURES

Figure 2.1 Electron microscopy and tomography of organic inclusions in the calcitic prisms from a mollusk shell.....	12
Figure 2.2 Electron microscopy, PEEM and XANES of inorganic inclusions in a brittle star lens.....	13
Figure 2.3 Schematic illustration of the three main forces that dictate the repulsion or incorporation of particles into a crystal.....	17
Figure 2.4 Examples from the literature of particle occlusion into crystals using normal forces provided by packing particles together	21
Figure 2.5 Examples from the literature of particle occlusion into crystals using normal forces provided by a strong gel	23
Figure 2.6 Schematic illustration of the key features that dictate the nature of the intermolecular forces between crystal surfaces and particle surfaces in solution.....	31
Figure 3.1. X-ray diffraction of an as-grown membrane following Cu ₂ O growth.....	64
Figure 3.2 Electron microscopy evidence for the growth mechanism of Cu ₂ O nanorods within membrane pores.....	65
Figure 3.3 Proposed mechanism for membrane templated nanorod growth shown schematically.....	67
Figure 3.4. SEM of Cu ₂ O nanorods formed in different pore size membranes.....	69
Figure 3.5. Electron microscopy showing the mechanism for ZnO nanorod growth and evidence that we do form ZnO/Au NP composites.....	71
Figure 3.6 Secondary and backscattered electron imaging of Au NP-loaded membranes.....	73
Figure 3.7 TEM of Cu ₂ O/Au NP composite rods grown where the nanoparticles are located within “plugs” or where nanoparticles are dispersed along the length of the rod.....	75
Figure 3.8. TEM imaging of Cu ₂ O/Au NP composite nanorods at four different α tilt angles.....	77
Figure 3.9. UV/Vis absorption of Au NPs	82
Figure 4.1 Schematic of the alignment of magnetic moments (a) in a polycrystalline material as described by the random anisotropy (RA) model and (b) in a mosaic crystal.....	101
Figure 4.2. Electron microscopy of our series of hematite samples, mosaic crystals, polycrystals and nanoparticles.....	104
Figure 4.3. Field-dependent magnetization is measured at two temperatures for all three samples... ..	106
Figure 4.4. Temperature-dependent, zero-field cooled/field cooled (ZFC/FC), magnetization measurements for all three samples	112
Figure 4.S1. Original SEM image of Fig. 4.2b.....	117
Figure 4.S2. Method for calculating and subtracting the antiferromagnetic (AFM) susceptibility (χ_{AFM}) from the 300 K field-dependent magnetization data in order to extract the remnant to saturation magnetization ratio and coercive field.....	118
Figure 4.S3. Method based on Ref. 71 for calculating the Morin transition temperature	

(T_m), the sharpness of the Morin transition (ΔT_m), and the percent decrease in magnetization from 300 K to 15 K ($\Delta M/M_{300K}$) from the zero field-cooled temperature-dependent magnetization data.....120

Figure 4.S4. Powder x-ray diffraction (XRD) for all three samples.....121

Figure 5.1. Powder x-ray diffraction patterns of the final products of bismuth iron oxide hydrothermal synthesis experiments.140

Figure 5.2. SEM images of phase-pure BiFeO_3 and phase-pure BiFeO_3 141

Figure 5.3. Powder x-ray diffraction patterns of the intermediate products formed prior to furnace treatment.144

Figure 5.4. Schematic representation of the proposed reaction pathways that lead to phase-pure $\text{Bi}_2\text{Fe}_4\text{O}_9$ and BiFeO_3146

Figure 5.S1. Scanning electron micrograph of phase-pure $\text{Bi}_2\text{Fe}_4\text{O}_9$ formed by the 10mM/0hr reaction conditions.....150

Figure 5.S2. Powder x-ray diffraction patterns of other reaction conditions for control experiments.....151

Figure 5.S3. XRD of “normal” phase-pure BiFeO_3 and phase-pure BiFeO_3 grown with the soluble ions in the intermediate products removed.....152

Figure A.1 SEM, TEM and magnetic properties of gel-grown mosaic crystals (quasispheres).....170

Figure A.2 SEM, TEM and magnetic properties of acid-etched, gel-grown mosaic crystals173

LIST OF TABLES

Table 3.1. Summary of Cu ₂ O/Au NP composite rod incorporation statistics.....	78
Table 4.1. Magnetic data for the four hematite samples.....	108
Table 4.S1. Calculated antiferromagnetic (AFM) susceptibility (χ_{AFM}) values for the four hematite samples.....	119
Table 4.S2. Crystallite sizes analysis (Scherrer) from Powder x-ray diffraction data.....	122
Table 5.1. Summary of hydrothermal growth conditions and intermediate and final phases present as identified by powder x-ray diffraction.....	138
Table A.1. Summary of magnetic properties of other mosaic crystals of hematite...	175

CHAPTER 1

PRELIMINARY DISCUSSION

1.1 Research Background

My whole career as a scientist has led me to undertake this interdisciplinary research project. From my earliest research experiences in molecular biology as a senior high school to my subsequent summer internships, I have worked on a wide array of research topics. These varied research experiences and my undergraduate degree in physics strongly influenced the perspective that I bring with me when approaching scientific questions.

As such, when I joined the Estroff group at Cornell, I was particularly interested in the ways that bio-inspired crystal growth can enable new electronic and magnetic properties. I would not have been able to undertake such a project had I not felt prepared to work at the interface between biology, chemistry, physics, geology and more.

In my Ph.D. work, I combined an eagerness to delve into the underlying physical principles of my research projects and an ability to translate those complex topics to audiences from diverse backgrounds. This combination helped me add a new research direction to the Estroff group, and also allowed me to begin to fill the critical gap of missing structure-property relations in the field of bio-inspired crystal growth.

1.2 Dissertation Introduction

Biom mineralization, the process by which organisms grow crystals, produces materials with complex architectures that impart improved functionality compared to their non-biogenic counterparts. In many examples, these biominerals have modified mechanical properties compared to their geologic counterparts, as seen in the increased hardness in the calcite prisms of the mollusk [1] or in the enhanced toughness of the amorphous silica surrounding diatoms[2]. In other examples, biominerals enable the organisms to perform magnetic or optical sensing, as seen in the cases of the magnetotactic bacteria, which synthesize a chain of iron oxide nanocrystals that act as a compass for the bacteria[3], or the brittlestar, which forms an array of calcite lenses that focus light onto photoreceptors.[4] In all these cases, the organisms precisely control the size, shape, location, polymorph, crystallographic orientation, and inclusion of additives into the crystal at low temperature in water. By learning from and translating the strategies that biology uses to grow crystals into the laboratory, we can then grow a wider range of materials with the same control over crystal morphologies.

Much research has focused on translating biomineral growth strategies into the laboratory to produce crystalline materials with similar structural characteristics. However, most of those studies end with sweeping claims about how their material might have new and exciting properties. **The goal of my thesis was to make the critical connection between the bio-inspired nanostructures and the electromagnetic properties of the materials.** Many electronic and magnetic

properties are highly sensitive to nanoscale features. Therefore, new structure-property relationships must be developed for these complex bio-inspired nanostructures. In my thesis work, we focus on two unique structures that are achieved in biomineral systems: single crystal composites and hierarchical structures, both of which are challenging to achieve using traditional growth methods.

1.3 Dissertation Overview

The scope of this thesis is to translate themes from biomineral growth into the laboratory to enable new electromagnetic properties.

In Chapter 2, we discuss the perplexing topic of single crystal composites. Crystallization is often used as a method for purification as it is thought to repel impurities from the perfect, periodic arrangement of atoms in the lattice. However, biomineralization routinely creates composite crystals, where second phases are incorporated within single crystalline domains. These second phases can range in size from atomic and small molecule impurities to proteins and biomacromolecular fibers.

We review what is known about the identities and strategies for incorporation of additives in biogenic crystals. With this knowledge, many examples have demonstrated the use of bio-inspired growth strategies to create single crystal composites in the lab. However, incorporation of nano- and micro-particles into crystals during aqueous solution growth remains poorly understood. Previously, most researchers in the field of bio-inspired crystal growth trying to trap particles within crystals relied on theory from how particles are captured in melt crystallization. However, these melt growth models do not consider the critical ways that solution

crystal growth mechanisms (spiral, layer-by-layer) or solution chemistry will affect incorporation. Here, we provide a theoretical framework to describe the forces responsible for particle occlusion with supporting empirical evidence. In short, a repulsive crystallization pressure always acts to repel impurities from a growing crystal. Either confinement or intermolecular forces can be utilized to oppose the crystallization pressure and allow for particle incorporation.

This review paper is in preparation to be submitted in February 2019 as an invited Focus article for *Materials Horizons*. The figures and schematics for this paper were prepared by Dr. Damian Palin.

In Chapter 3, armed with strategies for creation of single crystal composites, we use confinement to grow composite nanorods of plasmonic nanoparticles entrapped within semiconducting oxides. Plasmonic nanoparticle/semiconductor composites hold promise for optoelectronic applications ranging from solar cells to photocatalysts. Up until this point, there are only two typical morphologies for such heterostructures, core-shell nanoparticles and pre-formed semiconductor nanostructures that are decorated with nanoparticles, but both have significant limitations on the degree to which the absorption and charge transfer can be enhanced. A composite architecture in which multiple nanoparticles can be incorporated into a crystalline rod without the insulating barriers associated with ligands could allow us to further enhance optoelectronic performance.

Previous work from our group showed that track-etched membranes could be used as a template for the formation of composite Cu₂O/Au nanoparticle rods,[5]

where a large number of Au nanoparticles are encapsulated within crystalline cuprite nanorods. In the current work, we show the generalizability of this physical confinement-based approach to create other semiconductor/nanoparticle composites, such as Cu₂O/Ag and ZnO/Au. First, we load the track etched membrane with nanoparticles of an appropriate diameter with respect to the diameter of the pores such that the nanoparticles jam within the pores of the membrane. Then, using low-temperature, aqueous growth methods, we grow metal oxide semiconductors, which grow into the membrane pores and encapsulate the nanoparticles. By incorporating collections of nanoparticles into crystalline rods, we access a relatively unexplored morphology of plasmonic nanoparticle/semiconductor heterostructure that we predict may have enhanced light collection and charge separation compared to the current typical morphologies.

The work for this project was performed with the help of undergraduate student, Jeffrey Zheng, who performed much of the ZnO growth, and Masters student, Jennifer Tasneem, who will continue exploring the generalizability of this method. This project is a work in progress and will be submitted for publication at a later date.

In Chapter 4, we present a predictive model for the magnetic interactions in one type of mesostructured crystal, the mosaic crystal. Due to the composite nature of many biominerals, they are frequently found to be mesostructured, meaning their crystalline order is in between the perfect order of a single crystal and the random order of a polycrystal. Many examples of magnetic mesostructured crystals had been reported, but prior to my work, there was no framework to understand their magnetic

interactions.

I proposed a new model for interpreting the magnetic interactions in crystals with mosaic texture called the mosaic anisotropy (MA) model. These crystals with mosaic texture are defined by a low degree of misorientation between the adjacent (coherent) crystalline domains, meaning grains are separated by small angle ($< 15^\circ$) grain boundaries. Using mosaic crystals of hematite ($\alpha\text{-Fe}_2\text{O}_3$) as a model system, we validate our prediction that small angle grain boundaries in mosaic crystals allow for enhanced remanence and coercivity compared to single or polycrystals. This structure-property relationship demonstrated by this framework for the magnetic properties of mesostructured crystals reveal new routes to engineering harder magnetic materials.

A version of this chapter appeared as a manuscript that was published in *Applied Physics Letters*, **5**, 104901 (2017); doi: 10.1063/1.5007794.

In Chapter 5, we grow hierarchically-structured bismuth ferrite crystals and explore elements of their growth pathway. Having developed a predictive model for the magnetic interactions in mesostructured crystals, we sought to grow other interesting magnetic materials with complex crystalline architectures. We chose BiFeO_3 , which is the only known, room temperature magnetoelectric material, meaning its ferroelectric and ferromagnetic polarizations are coupled. BiFeO_3 has a similar type of magnetic order to hematite, which we explored in our previous study. However, this particular type of magnetic order actually complicates things. It means that bulk BiFeO_3 has no net magnetization, while nanoparticulate BiFeO_3 contains a magnetic polarization, but no electric polarization. These trends suggest that a BiFeO_3 morphology that is hierarchical, such that it is composed of small sub-units that are

arranged into a larger structure, may actually enable simultaneous ferromagnetic and ferroelectric polarizations.

We first needed to improve our understanding of how hydrothermal synthesis can be used to control the phase-purity and morphology of BiFeO₃. We identified a critical step, a prolonged pre-furnace, room-temperature reaction, necessary for phase purity in the hydrothermal synthesis of BiFeO₃. By considering the growth as a two-step process and considering the intermediate products separately from the final products, we identified that formation of Bi₂₅FeO₄₀ in the intermediate products seems to favor BiFeO₃ as the final product. The BiFeO₃ crystals formed by our method appear to be collections of faceted sub-units and it appears that we can alter the size and qualitative orientation of these sub-units by removing some of the spectator ions during the furnace treatment. By studying the reaction pathways for the hydrothermal synthesis of BiFeO₃, we lay the foundation for future work to explore the magnetoelectric properties of bismuth ferrite with hierarchical structures.

A version of this chapter appeared as a manuscript that was published in *Journal of Crystal Growth*, 468 (2017) 104–109; doi: 10.1016/j.jcrysgro.2016.09.054.

REFERENCES

- (1) Kunitake, M. E.; Mangano, L. M.; Peloquin, J. M.; Baker, S. P.; Estroff, L. A. Evaluation of Strengthening Mechanisms in Calcite Single Crystals from Mollusk Shells. *Acta Biomater.* **2013**, 9 (2), 5353–5359.
- (2) Hamm, C. E.; Merkel, R.; Springer, O.; Jurkojc, P.; Maiert, C.; Prechtelt, K.; Smetacek, V. Architecture and Material Properties of Diatom Shells Provide

Effective Mechanical Protection. *Nature* **2003**, *421* (6925), 841–843.

- (3) Frankel, R. B.; Bazylinski, D. A. Biologically Induced Mineralization by Bacteria. *Rev. Mineral. Geochemistry* **2003**, *54* (1), 95–114.
- (4) Aizenberg, J.; Tkachenko, A.; Weiner, S.; Addadi, L.; Hendler, G. Calcitic Microlenses as Part of the Photoreceptor System in Brittlestars. *Nature* **2001**, *412* (6849), 819–822.

CHAPTER 2

SINGLE CRYSTAL COMPOSITES:

TO INCLUDE OR NOT INCLUDE, THAT IS THE QUESTION*

2.1 Motivation

Single crystals, with their perfectly periodic arrangement of atoms, are typically thought to be free of impurities. Crystallization is even used as a purification technique, as foreign matter is rejected from the growing crystal.¹ However, single crystals of both geologic and biological origin have been found to incorporate impurities.

Understanding the processes that allow secondary phases to incorporate into single crystals not only addresses a curious issue, but it can also shed light on critical scientific questions that span disciplines. Studying gas or liquid inclusions in geologic minerals provides a snapshot of the geologic history of Earth, clueing scientists in to the atmospheric chemistry or volcanic activity billions of years ago.^{2,3} The remarkable mechanical properties of biologically-formed crystals, called biominerals, can be partially attributed to the incorporation of atomic and protein impurities.⁴

Advancements in modern mechanical, magnetic and optoelectronic applications take advantage of composites, which can integrate dissimilar materials and outperform single materials. However, the successful integration of dissimilar components is a major synthetic challenge and we are currently limited in the types of composite

* Co-contributors to this chapter include Dr. Damian Palin, who created all the figures and schematics.

structures we can fabricate. In this focus article, we learn from the well-studied field of biomineralization to understand how single crystals incorporate secondary phases. Here, we propose a new theoretical framework for the incorporation mechanisms of particles into crystals, which we believe can be applied to the creation of future advanced composite materials.

2.2 Biological inspiration for single crystal composites

The earliest evidence for the existence of a biomineral single crystal composite relied on relatively unsophisticated characterization methods. Calcitic sea urchin spicules were known to “blink” uniformly when viewed by cross polarized microscopy, indicating they are single crystalline in nature. These same spicules, however, do not fracture along well-defined crystallographic planes as expected for a single crystal. Instead, their cracks are deflected, hinting at the presence of other species within the crystal.⁵ This contraindicating evidence has puzzled scientists for decades, but with advancements in materials characterization methods, we can now learn the distributions and identities of inclusions in biominerals.

High resolution synchrotron x-ray diffraction of biominerals has been used to reveal the distribution of the additives within the crystalline lattice.⁶ Several studies have observed anisotropic deformations of the crystal lattice that are uncharacteristically large for ceramic materials.⁷⁻¹⁰ In these studies of calcite and aragonite biominerals from multiple mollusk species, their unit cell is systematically larger along the c axis than in their geologic counterparts, indicating that the additives seem to preferentially occlude on the (001) planes of the crystal structure. To visualize the spatial distribution of the nanoscale inclusions within biominerals, electron

microscopy has been used. By producing thin electron transparent sections of biominerals and imaging them using transmission electron microscopy (TEM), we can simultaneously observe a heterogeneous morphology with many obvious inclusions and a single crystal-like electron diffraction pattern (or single crystal-like fast Fourier transform).¹¹⁻¹³ (Fig. 2.1A, B, Fig. 2.2B) To determine the 3D distribution of inclusions, tomographic reconstructions can reveal the preferential confirmation and orientation of proteins within the calcite or aragonite lattice.^{11,13,14} (Fig. 2.1C) While these methods provide information about the distributions of additives in the crystal, they can only provide limited information about the identity of the additives lies in the relative contrast of the crystal and additive. For example, annular dark field mode of TEM imaging and intensity profile measurements allow us only to determine that these are organic inclusions, but we learn nothing of their chemical composition.^{11,14} (Fig. 2.1D,E)

To chemically and spatially resolve the identities of the additives in biominerals, two main techniques are used: x-ray spectroscopy and atom probe tomography. X-ray absorption near-edge structure (XANES) and extended x-ray absorption fine structure (EXAFS) spectroscopy both probe local atomic structure. When these spectroscopic techniques are combined with photoelectron emission spectromicroscopy (PEEM), the combined method (X-PEEM) produces spatial maps with chemical information about the inclusions.¹⁵⁻¹⁷ For example, in the brittle star lens (Fig. 2.2B), this method was able to resolve slight changes in local atomic structure to prove the nanodomains are inorganic Mg-rich calcite nanoparticles within a single crystal calcite matrix.¹² (Fig. 2.2C, D) Atom probe tomography (APT) is the only method that can detect and study

true atomic-scale inclusions.¹⁸ By milling the biomineral sample into a fine needle shape, and then ionizing clusters of atoms from the tip of the sample and tracking the trajectory of the ions to learn their charge-to-mass ratios, we can create a chemical map of the components in the sample.¹⁹ APT is one of the only techniques that can identify

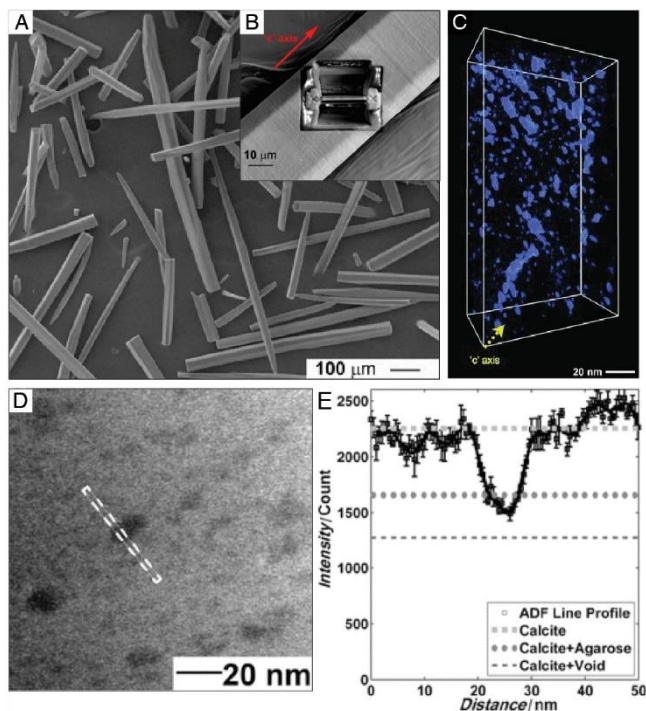


Figure 2.1 (A) SEM image of single crystal prisms isolated from the calcitic layer of a mollusk shell (B) Higher magnification SEM image of a prism, with (inset) showing the FIB-thinned section of known orientation from within prism (C) A tomographic reconstruction shows the 3D distribution and preferential orientation of biomacromolecules incorporated within the thin crystalline section shown in (B). (D) HAADF-STEM image showing dark inclusions within a light crystalline matrix, indicating the inclusions have a lower Z than the crystal. (E) The intensity profile along the white dashed line from (D) compared with calculated intensities confirms that the dark regions are organic inclusions and not voids. Reprinted (adapted) with permission from H. Li, H.L. Xin, M.E. Kunitake, E.C. Keene, D.A. Muller, L.A. Estroff, Calcite prisms from mollusk shells (*Atrina rigida*): Swiss-cheese-like organic-inorganic single-crystal composites, *Adv. Funct. Mater* **2011**, 21, 2028–2034. Copyright 2011 John Wiley and Sons

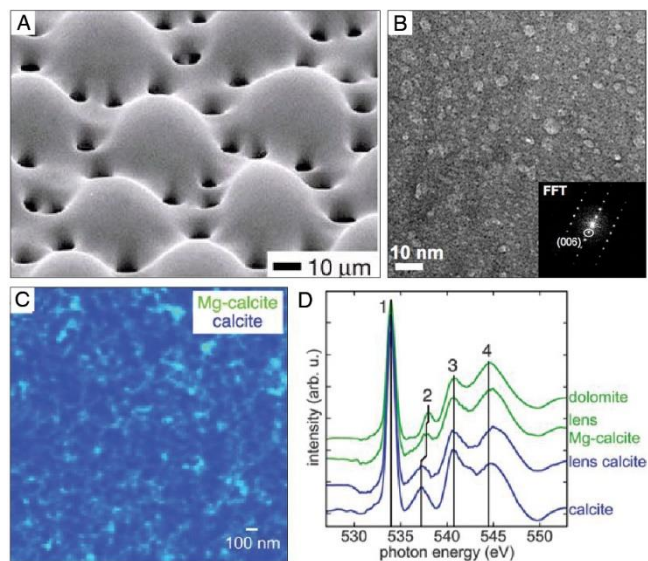


Figure 2.2 (A) SEM of the calcitic brittle star lens. Reprinted by permission from Springer Nature : Aizenberg, J. Tkachenko, A., Weiner, S., Addadi, L., Hendler, G. Calcitic microlenses as part of the photoreceptor system in brittlestars, *Nature*. **2001** 412, 819–822. doi:10.1038/35090573. Copyright 2001 (B) High resolution TEM of a thin section from a brittle star lens shown in (A) shows a heterogeneous nanostructure with bright nanodomains simultaneous with an FFT pattern (inset) that is single crystal-like. (C) A PEEM map of the lens reveals the spatial distribution of low magnesium calcite (blue) and high magnesium calcite (green). Magnesium-rich calcite nanoparticles appear as cyan. (D) Oxygen XANES spectra of the lens and relevant control samples indicate that the crystalline structure of the lens calcite is similar to geological calcite, as shown by aligned peaks 1 to 4 (vertical lines), while the lens Mg-calcite is intermediate between calcite and dolomite (MgCO_3), as shown by the position of peak 2. From Polishchuk, I.; Bracha, A. A.; Bloch, L.; Levy, D.; Kozachkevich, S.; Etinger-Geller, Y.; Kauffmann, Y.; Burghammer, M.; Giacobbe, C.; Villanova, J.; et al. Coherently Aligned Nanoparticles within a Biogenic Single Crystal: A Biological Prestressing Strategy. *Science*. **2017**, 358 (6368), 1294–1298. Reprinted with permission from AAAS

small quantities of organic additives dispersed in a crystal.^{20,21}

The question of how these secondary phases are incorporated into the growing crystal remains. To do mechanistic studies of incorporation, we need to use model systems. Calcite is the main model biomineral, and synthetic studies have examined the incorporation of additives across a range of length scales.²²⁻²⁴ *Ex situ* growth of calcite in the presence of extracted biomineral proteins has helped reveal how these proteins can modify bulk morphology and inhibit crystal growth along specific crystallographic directions.^{25,26} Fluorescent-labeling of these soluble biomineral proteins and imaging using sub-diffraction limit techniques have allowed for visualization of the internal structure of these crystalline composites.²⁷⁻²⁹

To investigate the mechanisms by which these soluble proteins interact with growing crystals, “synthetic proteins,” like designer double-hydrophilic block copolymers (DHBCs) have been used.³⁰⁻³² These designer polymers allow for systematic studies of how polymer charge, functional group, hydrophobicity, etc. modify crystal growth, which provides insight on the necessary characteristics of proteins to incorporate into biominerals. When the DHBCs include highly charged acidic groups, a common feature of biomineral proteins, they too interact strongly with the growing crystal, drastically modifying its typical single crystal morphology. In many cases, the DHBCs induce the formation of mosaic or mesostructured crystals, where the polymer occupies space at the grain boundaries between the neighboring crystalline sub-units, rather than incorporating within the crystallites themselves.³³ The synthesis and mechanisms for forming these mosaic-type mesostructures is an active area of study³⁴,

but in this article, our focus is understanding additives occlusion *within* a single crystal matrix.

We further restrict the scope of this article to discuss occlusion of nano- and micro-particles into single crystals. As we saw earlier, in the biogenic systems, macromolecules often appear in isolated nanodomains within the crystalline matrix, suggesting that they may incorporate not in an extended conformation, but in collapsed protein aggregates.¹¹ (Fig. 2.1C) Therefore, studying the incorporation of particles in crystals may serve as a more representative model system for understanding incorporation mechanisms of soluble biomineral additives. Furthermore, for crystals to occlude particles whose size is much larger than that of the crystal lattice presents a perplexing challenge. Many models have described how particles can get captured by crystals during melt or freezing transitions.^{35–38} In melt crystal growth, new growth units, and therefore additives too, are relatively agnostic to their crystallographic addition site. Solution crystal growth, especially at low supersaturations, new growth units preferentially add to kink and edge sites, during spiral and layer-by-layer growth, respectively. Other reviews have described how a wide size range of impurities, from small molecules to gel fibers, can incorporate into single crystals during solution growth.^{4,24,39,40} However, to date, there is no firm understanding of how particle incorporation occurs during solution crystal growth.

Here, we present a theoretical framework for the forces that govern particle occlusion/repulsion during solution growth. While many particle occlusion studies use calcite as the “host” crystal, several studies have also considered more functional solution-grown crystals, such as semiconducting zinc oxide. Through this framework

for particle incorporation, we hope to provide the foundation that can be applied to grow functional single crystal composites with optoelectronic applications. For example, when quantum dots are occluded within polycrystalline salt crystals, their stability is improved due to their isolation from the environment.⁴¹⁻⁴³ But eliminating the grain boundaries in the host crystal or incorporating quantum dots into functional host crystals has the potential to further enhance their properties.^{44,45} Another promising opportunity for single crystal composites is for plasmonic nanoparticle/semiconductor heterostructures for photocatalytic or photovoltaic applications.⁴⁶⁻⁴⁸ Current state-of-the-art heterostructures include geometries like plasmonic nanoparticle core/semiconductor shell particles or plasmonic nanoparticle-decorated semiconductors, but a structure that can incorporate multiple plasmonic nanoparticles within a semiconducting crystal could further improve absorption and energy transfer.

2.3 Theoretical framework for particle incorporation during solution growth

In this section, we discuss the possible particle/crystal interactions in an aqueous salt solution. We take stock of the repulsive and attractive forces between the particles and crystal, and highlight the experimental variables that control the magnitude of each force. The central idea to our framework is that when the forces that repel particles are overcome by attractive or external forces, the crystal entraps the particles. (Fig. 2.3)

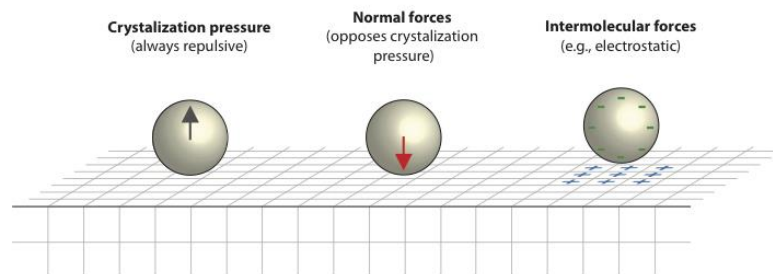


Figure 2.3 Schematic illustration of the three main forces that dictate the repulsion or incorporation of particles into a crystal. A repulsive crystallization pressure acts to push particles out of the growing crystal. Crystals can occlude particles if the crystallization pressure is opposed by external forces, like normal forces provided by a template or attractive intermolecular forces generated between the particle and crystal.

2.3.1 Crystallization pressure

The crystallization pressure is one of the primary repulsive forces acting on the particles in solution. Crystallization pressure was defined by Khaimov-Mal'kov as the external force applied to a crystal required to stop the crystal from growing further.⁴⁹ While crystallization pressure does increase with supersaturation, it is relatively independent of the properties of the crystal and solution. At even mild supersaturations ($\sigma = 1.1$), the crystallization pressure is large at $\sim 8 \text{ kg/cm}^2$, meaning a crystal with a 1 cm^2 facet exerts enough force on its surroundings to lift an 8 kg mass.⁴⁹ Therefore, considering crystallization pressure alone, we would predict that all impurities would be expelled from the growing crystal and we would never form single crystal composites.

In the following two sections, we present the two primary forces that have been explored to overcome this repulsive crystallization pressure. The first approach uses normal forces to counterbalance the crystallization pressure and the second approach relies on tuning intermolecular forces to achieve a net attractive interaction between a particle and crystal.

2.4 Using normal forces to oppose crystallization pressure

The concept of the normal force was introduced by Sir Isaac Newton in his first law of motion.⁵⁰ When a force is applied to an object, the object will begin to move. For the object is to remain static, an equal and opposite force must be applied. In crystal growth, when a growing crystal exerts a repulsive force due to the crystallization pressure on a particle, the particle will get pushed ahead of the crystal growth front, resulting in no incorporation. If a force equal and opposite to the crystallization pressure

exists, then the particle can remain “static” and can become incorporated into the growing crystal. There are two predominant synthetic strategies for engineering these normal forces, immobilizing particles either in a colloidal crystal-like template or in a strong gel matrix.

2.4.1 Particles forming a colloidal crystal-like template

Several rigid 3D nanostructured materials have proved immovable by a growing crystal front, allowing for the crystals to occlude the nanostructured template. A large number of single crystalline materials, like calcite, SrSO₄, PbSO₄, PbCO₃, NaCl and CuSO₄*5H₂O, have been found to occlude rigid templates, such as 3D, nanostructured block co-polymer gyroids or replicas of sea urchin skeletal plates.⁵¹⁻⁵³ Calcite crystals can also incorporate rigid templates formed by ordered particle packings, called colloidal crystals.⁵⁴

The approach of using colloidal crystal packings of particles has been successfully demonstrated for crystalline materials other than calcite. Polystyrene particles were assembled into a uniform 3D template for the subsequent growth of Cu₂O and ZnO single crystals.⁵⁵ Though incorporation of polymer particles into semiconducting oxides may not directly impact the electronic properties of the crystals, other work showed that incorporating amino acids into ZnO single crystals creates anisotropic distortions to the lattice that lead to changes in the semiconducting band gap.^{56,57} In many cases, the functional use for these colloidal crystal-derived single crystal composites only emerges once the polystyrene particles are burned off, and then the 3D macroporous, single crystal templates are used for a variety of photo- or electro-chemical applications.⁵⁸

As seen above, the forces provided by the colloidal template are sufficient to oppose the crystallization pressure, allowing crystals to occlude particles. In these studies, the ability of the single crystal to occlude the particles does not depend on the degree of order in the colloidal packing. It seems that the counter force that the rigid template and growth in a confined environment provide on the growing crystal are more critical. These principles guide our understanding of how to entrap functional nanoparticles, which are less likely than micron-sized polymer colloids to form into well-ordered colloidal crystals.

In recent work from our group, confinement was used to generate Cu_2O single crystals with incorporated Au nanoparticles.^{59,60} In one study, Au nanoparticles are immobilized within the cylindrical pores of a track-etched membrane.⁵⁹ (Fig. 2.4A) The nanoparticles in the membrane pores do not form ordered crystalline packings as with the colloidal crystals above, but instead form disordered arrays. When Cu_2O grows within the membrane pores, it entraps the arrays of Au nanoparticles within cylindrical, high aspect ratio, crystalline Cu_2O rods. (Fig. 2.4B, D) Extraordinarily, the encapsulation of many nanoparticles does not disrupt the crystalline lattice of the Cu_2O as seen by the continuous lattice fringes. (Fig. 2.4C) Thus, it appears that normal forces provided by the immobilization of the nanoparticles in the membrane pores prevent the nanoparticles from being pushed ahead of the Cu_2O growth front.

2.4.2 Particles in a gel matrix

In the previous section, we showed how normal forces from packings of particles can counter the repulsive crystallization pressure. Here, we consider how particles loaded into a gel matrix can also form single crystal composites.

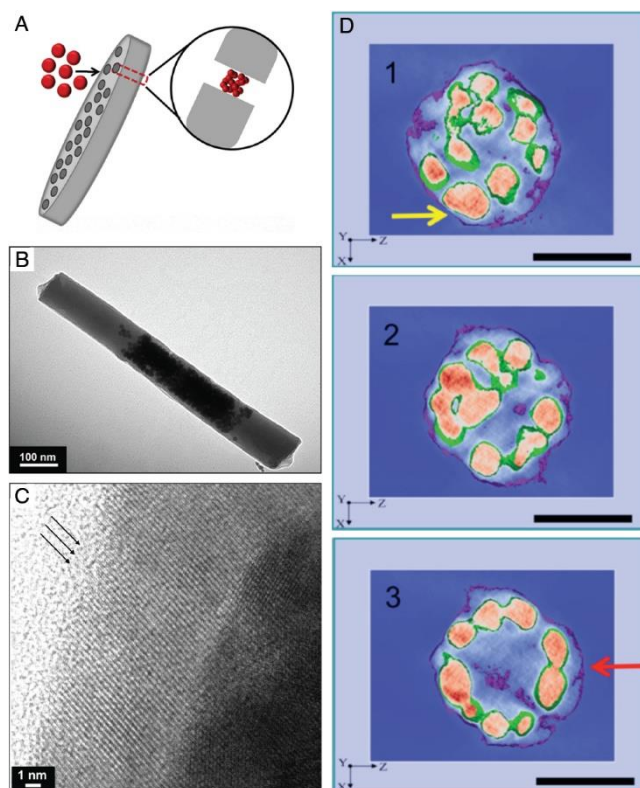


Figure 2.4 (A) Schematic representation of the formation of Au nanoparticle arrays within the pores of track-etched membranes. (B) TEM image of a Cu₂O nanorod with many entrapped Au nanoparticles (darker region in middle portion of the rod) formed by growing Cu₂O within the nanoparticle-loaded membrane pores. (C) High-resolution STEM of the Cu₂O-Au interface illustrating the continuous lattice fringes (highlighted with arrows) of the crystalline Cu₂O that surrounds the Au nanoparticle array. (D) Three slices from a tomographic STEM reconstruction of the 3D structure of a Cu₂O-Au nanorod showing that many Au nanoparticles are encapsulated throughout the Cu₂O rod. (Au= green isosurface; Cu₂O = purple isosurface). The scale bar = 50 nm Reprinted (adapted) with permission from Asenath-Smith, E.; Noble, J. M.; Hovden, R.; Uhl, A. M.; DiCorato, A.; Kim, Y.-Y.; Kulak, A. N.; Meldrum, F. C.; Kourkoutis, L. F.; Estroff, L. A. Physical Confinement Promoting Formation of Cu₂O–Au Heterostructures with Au Nanoparticles Entrapped within Crystalline Cu₂O Nanorods. *Chem. Mater.* 2017, 29 (2), 555–563. Copyright 2017 American Chemical Society

It is well known that crystals grown in a gel matrix can incorporate gel fibers within the crystal⁶¹, and the mechanisms for gel incorporation in calcite are fairly well agreed upon.^{24,62} The relationship between crystallization pressure and gel strength, defined as the force that must be applied for the gel to fracture, determines whether a gel becomes incorporated or not. When the crystallization pressure exceeds the gel strength, the growing crystal will fracture any gel fibers it encounters, thus expelling them from the crystal. However, a strong enough gel will provide sufficient resistance to oppose the crystallization pressure and gel fibers will be incorporated into the growing crystal.

By loading a strong gel with nanoparticles, several groups have used strong gels to generate composite single crystals of calcite with nanoparticles occluded in addition to the gel.^{63–65} (Fig. 2.5) When the nanoparticles alone were added to the calcite growth solution, the nanoparticles were excluded from the crystal. Incorporation of nanoparticles into the gel has even been found to increase the gel stiffness, thus promoting an even greater degree of particle and gel incorporation.⁶³

Loading gels with nanoparticles seems to be a versatile approach to generating single crystal composites as it is relatively independent of particle material, size and shape. The same gel can be used to incorporate different nanoparticles into calcite crystals. For example, an agarose matrix was used to incorporate Au, Fe₃O₄, CdTe quantum dots, and polymer dots^{64,66} and a xyloglucan gel matrix was used to incorporate Fe₃O₄ and ZnO nanoparticles.⁶³ In all of these studies, calcite is crystalline matrix into which the gel and nanoparticles incorporate. There are many other crystals

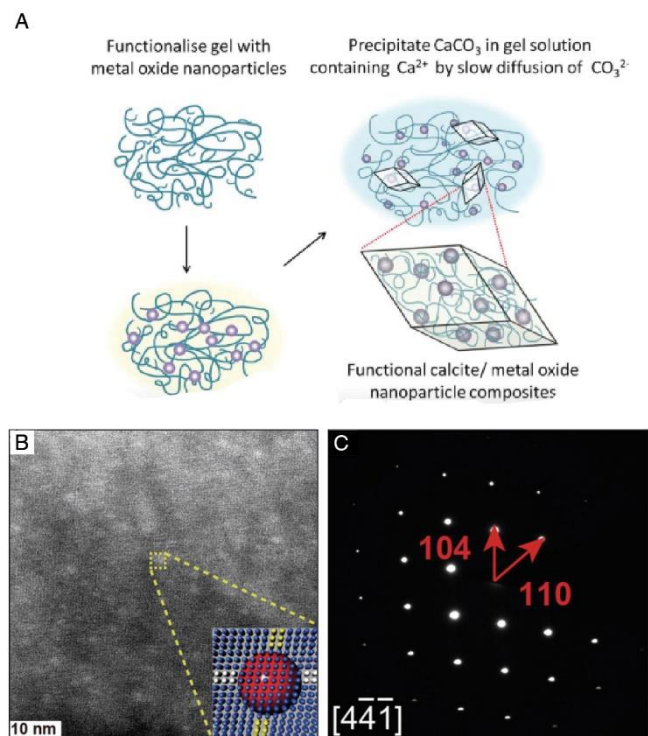


Figure 2.5 (A) Schematic methodology for using nanoparticle-loaded gels to form single crystal calcite with occluded metal oxide nanoparticles. Reproduced from Kim, Y.-Y.; Schenk, A. S.; Walsh, D.; Kulak, A. N.; Cespedes, O.; Meldrum, F. C. Bio-Inspired Formation of Functional Calcite/Metal Oxide Nanoparticle Composites. *Nanoscale* **2014**, 6 (2), 852–859. with permission from The Royal Society of Chemistry (B) A HAADF-STEM image of a thin section from a calcite crystal grown in a quantum dot-loaded gel reveals a uniform distribution of the quantum dots (bright spots), shown schematically in the inset. (C) Electron diffraction pattern of the crystal in (B) shows a single crystal-like diffraction pattern despite the occlusion of gel fibers and quantum dots. Reprinted (adapted) with permission from Liu, Y., Zang, H., Wang, L., Fu, W., Yuan, W., Wu, J., Jin, X., Han, J., Wu, C., Wang, Y., Xin, H.L., Chen, H., Li, H. Nanoparticles Incorporated inside Single-Crystals: Enhanced Fluorescent Properties, *Chem. Mater.* **2016**, 28, 20, 7537–7543. doi:10.1021/acs.chemmater.6b03589. Copyright 2016 American Chemical Society.

known to incorporate gel fibers⁶⁷⁻⁶⁹. With further study, this approach of trapping particles in gels that become incorporated can be applied to other crystal systems.

2.4.3 Summary and remaining questions: normal forces

In summary, normal forces can be used to overcome the repulsive crystallization pressure and allow for the formation of single crystal composites in the lab. There are two primary approaches for generating normal forces to oppose the crystallization pressure: assembling particles into colloidal crystal-like packings and trapping particles within a gel matrix. Further study is required to understand how exactly a gel matrix, even one stiffened by incorporation of particles, is able to provide sufficient force to counter a crystallization pressure of $\sim 8 \text{ kg/cm}^2$. With this framework in mind, we can now begin to explore other types of forces that might play a similar role to traditional normal forces in opposing the crystallization pressure. For example, can entropic hard sphere repulsion generate sufficient forces to preventing particles from getting pushed ahead of a crystal growth front?

Using normal forces to oppose the crystallization pressure has shown the potential for developing functional composite materials. Incorporation of quantum dot or polymer dot nanoparticles into a gel and then into calcite keeps the nanoparticles isolated from the environment and improves their photostability.⁶⁵ The role of the gel in modifying the optoelectronic properties of these composites is not known. In other systems, gel incorporation into crystals can be designed to have a functional purpose^{69,70}, so future research should work towards designing crystal/gel/particle pairings where each component has a functional role. Though we might not expect the incorporation of insulating polymer particles into semiconducting single crystals to

affect their optoelectronic properties, other studies have shown incorporation of additives to influence the bandgap of the semiconductor.^{56,57} In recent work from our group, functional plasmonic nanoparticles were incorporated into crystalline semiconductors, which is expected to improve both the absorption and the charge transfer of the composites.⁷¹

2.5 Tuning intermolecular forces to create net attractive forces

In this section, we consider how crystals can occlude mobile particles. In this thought experiment, we consider a “one-pot” synthesis, where particles and a supersaturated growth solution are mixed together in a single beaker and we wait to see whether particles incorporate or are pushed out of the growing crystals. Earliest attempts to incorporate polymer microparticles in crystals relied on “guess-and-check” approach as they varied the particle surface functional groups and checked whether particles incorporated or not.^{72–75} Recently, there have been a number of systematic studies that provide beautiful examples of particle occlusion within crystals.^{76–86} Here, we combine this empirical experimental evidence with concepts from the theory of intermolecular surface forces to provide a theoretical framework for why some particles/crystals incorporate and others do not.

Chernov and others pioneered the early work on particle incorporation, focusing on the “disjoining pressure,” which despite its name can describe both repulsive and attractive interactions.^{87,88} Disjoining pressure describes the van der Waals, electrostatic, and solvation forces that determine the equilibrium thickness of a liquid film between two surfaces.^{36,87,89} For our purposes, we are mostly interested in whether this equilibrium thickness is zero (meaning the particle is attracted and in direct contact

with the crystal surface) or non-zero (meaning the particle remains outside the crystal). Based upon the concept of the disjoining pressure, several models defined the criteria for particle incorporation during melt crystal growth or freezing transitions.^{35–38,87,90} In the decades since these models were proposed, our computational modeling and experimental measurement capabilities of the intermolecular surface forces at play during solution crystal growth have drastically increased, but have not yet been applied to understanding particle incorporation. In particular, no models for particle incorporation consider two critical elements of solution crystal growth: 1) the ways in which these intermolecular forces behave in aqueous electrolyte solutions, and 2) the ways in which the common solution crystal growth mechanisms of layer-by-layer or spiral growth affect particle incorporation. Due to the complexity of the problem, we separately consider the characteristics of the particle surface and the crystal surface necessary for incorporation.

2.5.1 Crystal surfaces in solution

In this section, we describe four of the key elements of crystal surfaces in solution: hydration layers, electric double layers, step/kink sites and attachment/detachment kinetics. (Fig. 2.6) Within the past decade, our understanding of water structuring and binding dynamics at crystal surfaces has drastically improved due to new experimental and computational methods. For example, in calcite, it has been shown computationally that during growth, new calcium and carbonate growth units interact with structured water layers above the physical crystal surface and they each have distinct sites along the step edges to which they bind.⁹¹ The complexity of the growth mechanism in the pure calcite system highlights how challenging it will be to

also consider impurities. Calcite solution growth is one of the most heavily studied systems in this field, and though many studies refer to calcite, we try to highlight concepts that apply to other ionic crystals.

An ionic crystal in an aqueous solution will interact strongly with the water in solution, leading to “bound” water molecules organized on the crystal surface. For a particle to bind to this hydrated crystal surface, first the bound water in the hydration layers must be removed from the surface. Recently, surface force measurements were able to resolve the forces required to “squeeze out” individual hydration layers on a calcite surface.⁹² The force required to remove hydration layers from the surface presents an additional barrier to particle incorporation. The magnitude of the hydration binding depends both on properties of the crystal surface and the solution chemistry. Frequency-modulated atomic force microscopy can be used to image structured water layers at crystal surfaces.^{93,94} Applying this method to calcite, Söngen et al. found there are five distinct layers of bound water on a calcite (104) surface and that individual point defects in the calcite will modify structure of these hydration layers.⁹³ Therefore, for a particle to incorporate into calcite, there are actually five barriers associated with disruption hydration layers to overcome. Can careful choice of solution chemistry reduce the strength of water binding? Surface force measurements show how decreasing ionic strength of the solution can change the nature of these hydration forces from largely repulsive to oscillatory.⁹⁵ More recent surface force measurements were able to detect the subtle ways that specific ions in solution can change the magnitudes of the binding forces, depending on the polarizability, size and hydration of the ions.⁹⁶ Specific ion effects have been considered in relation to Mg^{2+} incorporation into calcium

carbonate, where magnesium's ability to disrupt hydration layers has been thought to contribute to its role in calcium carbonate polymorph selectivity.⁹⁷ In future work, specific ion effects should also be considered to help disrupt hydration layers and allow for easier incorporation of particles into crystals.

Electrostatics are useful for generating attractive forces between the crystal surface and a particle in solution, as a negatively charged particle will be attracted to a positively charged crystal surface.⁹⁸ The distance over which the particle and crystal can experience an attractive force is determined by the thickness of the electric double layer (EDL). The EDL describes the way in which layers of ions in solution assemble at the charged crystal surface. For example, when a positively charged surface is immersed in an electrolyte solution, negatively charged ions in solution will be attracted to and bind the surface, and then positively charged ions in solution will be attracted to and loosely bind to those negative charges. The thickness of the EDL is dictated by the ionic strength of the solution and not by properties of the crystal. In a higher ionic strength solution, ions bind more strongly to the crystal surface, leading to a shorter EDL. For a pure water solution, the EDL thickness is nearly 1 μm , while for a 1 mM NaCl solution it is drastically reduced to only 9.6 nm.⁹⁸ If a particle is farther than the length of the EDL away from the crystal surface, the charges on the crystal surface have been "screened" and the particle and crystal experience no electrostatic interactions. Therefore, a thicker EDL is desirable because the electrostatic attraction between the particle and crystal can occur at larger distances from the crystal surface. The thickness of the EDL depends only on the properties of the solution, and not on the properties of the crystal. For crystal growth to occur, the solution must be supersaturated, but based

on electrostatic considerations, working at the lowest possible supersaturation is more likely to promote attractive particle/crystal interactions.

Solution crystal growth, particularly at low supersaturations, typically proceeds by either layer-by-layer or spiral growth, where addition of growth units occurs at step or kink sites.⁹⁹ (Fig. 2.6) Recent reports also indicate that particles in solution appear to bind with calcite step edges prior to incorporation.^{78,100} Therefore, the chemistry and electrostatic properties of the step or kink sites may be more important to consider than the overall crystal surface properties. However, only careful computational studies that account for the complexity of the solvent can give us insight into the properties of the steps or kinks. For example, as mentioned above, in calcite, molecular dynamics calculations predict there are two distinct edge sites during growth, which each have drastically different binding affinities for the calcium and carbonate growth units in solution.⁹¹ Experimentally, we can watch crystal growth and particle incorporation in solution in real time using *in situ* atomic force microscopy (AFM). By imaging under the equilibrium solution conditions, when the crystal is neither growing nor dissolving, we can watch particle attachment in the absence of growth. In a recent *in situ* AFM study, particles showed a slight preference for one of the two calcite edge sites over the other, though it is not understood why. Due to the difficulty of performing both these experiments and calculations, further research is needed to draw more general conclusions about the binding site preferences of particles on other crystalline materials.

During solution crystal growth, new growth units (ions) are constantly attaching and detaching from the crystal surface, and when the rate of attachment (k_{on}) is greater than the rate of detachment (k_{off}), the crystal will grow. For particles to incorporate into

a growing crystal, their rate of attachment must be not too much larger or too much smaller than that of the new growth units. When impurity binds too strongly ($k_{\text{on}} \gg k_{\text{off}}$), even at large supersaturations, growth of the crystals halts entirely.^{101,102} However, recent kinetic Monte Carlo simulations revealed a new mechanism that allows for incorporation of strongly impurities. Even when these strongly bound impurities impede normal step flow, macrosteps can still advance and occlude a large number of impurities when they do.¹⁰³ In most real-world cases, the attachment of the additives is weaker than that of new growth units. If the impurity attaches too weakly ($k_{\text{off}} \gg k_{\text{on}}$), then by the time the crystal growth front reaches the site with a bound impurity, the impurity will have detached back into solution. A recent study from our group used *in situ* AFM to track the incorporation/detachment behavior of particles interacting with a growing calcite crystal.⁷⁸ We found that there is a third possible behavior, a hovering of the particles over the advancing crystal growth front. This hovering phenomenon has only been reported for protein crystals and is not well understood.¹⁰⁴ Slight differences in particle surface, which we discuss in the following section, determine the likelihood of the particle to hover or detach from the crystal surface, hinting at potential new strategies when designing particle/crystal interactions.

2.5.2 Particle surfaces in solution

A wide variety of particles, ranging from large polymer microparticles to inorganic nanoparticles to organic block co-polymer micelles, have all been incorporated into single crystals in the lab.⁷⁶⁻⁸⁶ It may seem challenging to draw overarching conclusions about how all these different particles interact with a growing crystal. However, all the particles that have been successfully incorporated contained a

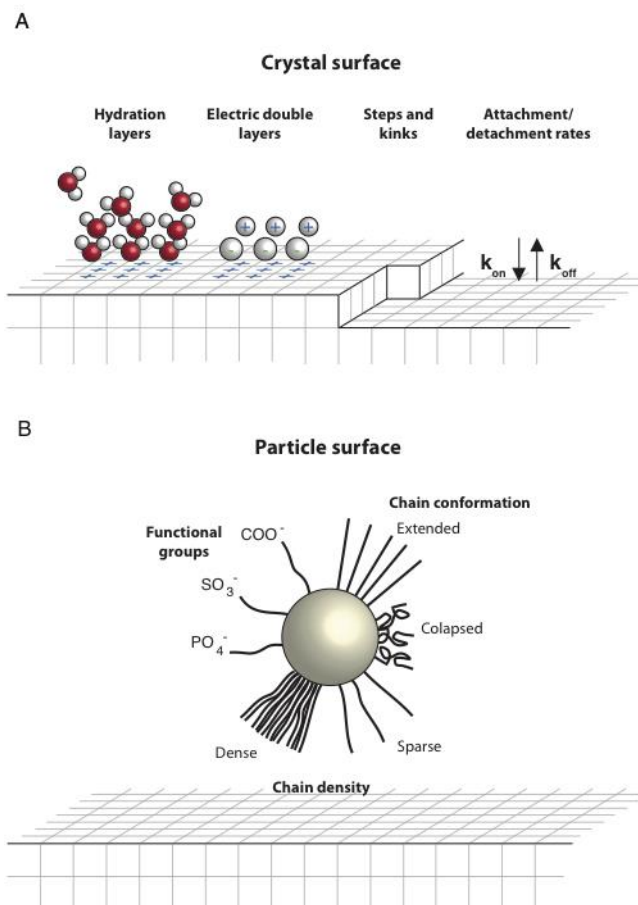


Figure 2.6 Schematic illustration of the key features that dictate the nature of the intermolecular forces between (A) crystal surfaces and (B) particle surfaces in solution. The solution chemistry (pH, ionic strength, ratio of monovalent to multivalent ions) impacts nearly all of these characteristics.

stabilizing corona of polymer chains. (Only in very rare cases were bare, un-functionalized nanoparticles found to incorporate into crystals.^{105,106}) Thus, we can broadly understand incorporation mechanisms across various particle types by considering the behavior of the stabilizer chains, as they are what must contact the crystal for incorporation to occur. In particular, we discuss key features like chain functional group, chain density and polyelectrolyte chain conformation (Fig. 2.6).

Most of the proteins occluded by calcite biominerals contain highly acidic, negatively charged functional groups.^{107,108} Therefore, it might not be surprising that adding anionic stabilizer chains to the surface of particles allows them to incorporate into calcite. We might hypothesize that a negatively charged corona of stabilizer chains interacting with a positively charged crystal surface provides attractive electrostatic forces that promote incorporation. Across numerous studies, incorporation always occurred for particles whose stabilizer chains had purely anionic character, independent of the specific, charged functional group (carboxylate, sulfate and phosphate). In one case, cationic stabilizer chains were used to successfully incorporate Au nanoparticles into calcite.⁷⁶ Zwitterionic stabilizer chains, which contain both anionic and cationic functional groups, were found not as effective as purely anionic groups at generating attractive interactions between a particle and crystal.⁸² Non-ionic functional groups have been shown to not incorporate,^{78,84} though a recent study showed that a mix of anionic and non-ionic stabilizer chains was effective at promoting incorporation.⁸⁶ Even with anionic functional groups, the solution chemistry, specifically pH and ionic strength, must be appropriately chosen to generate sufficient attractive forces. For example, if the growth solution pH is too low to fully deprotonate the functional groups,

then the particle will have an overall lower anionic character and will not incorporate as well.^{73,80} The ionic strength also affects the electric double layer thickness around the particles. At higher salt concentrations, the charges of the stabilizer chains are effectively screened by the charges in solution, meaning the particles must be very close to the crystal surface before they experience attractive forces.¹⁰⁹

Polyelectrolyte stabilizer chains appear to be one of the most effective corona features for particle occlusion. Strongly acidic polyelectrolyte chains were used to occlude Au, Fe₃O₄ and polymer nanoparticles in calcite and/or ZnO.^{76,79,81,85,110}

Polyelectrolyte stabilizer chains have the potential for multivalent interactions with the crystal surface because each chain contains many charged groups that could bind with multiple sites along the crystal surface. To achieve this optimal binding conformation, we must carefully choose the solution chemistry and the design of the polyelectrolyte chains.

To understand how polyelectrolyte chains rearrange to achieve optimal binding, we need to consider the behavior of tethered polyelectrolyte chains in the ionic growth solution. When polyelectrolyte chains are anchored to a particle, their behavior is best described by polyelectrolyte brush theory.¹¹¹ In a high pH solution, the functional groups become fully deprotonated making the chains highly charged. Under these conditions, the polyelectrolyte brush is in its “swollen” state, where due to osmotic pressure from the ions in solution, chains extend straight outward. However, in a strong electrolyte solution, the ions in solution begin to screen the charges of one chain from its neighbors and the chains become free to rearrange or “collapse”.¹¹² Multivalent ions in solution, even at low concentrations, are more likely than monovalent ions to lead to

polyelectrolyte brush collapse.^{113–115} Once collapsed, the stabilizer chains now have additional conformational degrees of freedom.

Design of stabilizer chains with more degrees of conformational freedom can also aid incorporation of particles into growing crystals. Longer polyelectrolyte chains incorporate more effectively than short ones due to the greater extent to which they can rearrange themselves.⁸⁶ The choice of polymer backbone also plays a large role in the conformational freedom of the chains, though until now it has received little attention. For example, the degree to which the charged functional groups “dangle” off of the stabilizer chain backbone will impact their ability to access the appropriate areas of the crystal surface. Additionally, the nature of the bonding along the backbone will influence the chain rearrangement. When we compare within the subset the polymers with carboxylic acid functional groups used in these incorporation studies, some polymers have ester bonds connecting the backbone to the carboxylic acid group, while others contain amide or other types of bonds in addition to the ester bonds. This slight difference in backbone chemistry will affect the rotational freedom of the chain as well as the ways that neighboring chains can hydrogen bond to one another.

Recent work from our group and the Meldrum group has begun to consider how non-polyelectrolyte chains may still allow for particle occlusion into calcite crystals. Non-polyelectrolyte chains do not collapse in the presence of salt solutions. Our group compared the incorporation behavior of two particle chemistries, one with carboxylic acid polyelectrolyte chains and the other a non-polyelectrolyte backbone with terminal carboxylic acid functional groups at the tips of the chains. A detailed look at the interactions of these two types of particles using *in situ* AFM reveals that they both

incorporate with similar efficiencies.⁷⁸ The main difference in the behavior of the two particles is that the particles with polyelectrolyte chains were more likely to “hover” over a growing step edge, while the non-polyelectrolyte chains are more likely to attach and then detach from the crystal surface. As mentioned previously, hovering is not well understood, but we can hypothesize that the ability of the polyelectrolyte stabilizer chains to collapse and rearrange in the vicinity of the crystal surface helps those particles hover instead of detach. In the Meldrum group study, which performed *ex situ* growth of calcite, the presence of non-polyelectrolyte chains was thought to increase the residency time of particles on the growing crystal surface.⁸⁶ Particles with a mix of polyelectrolyte and non-polyelectrolyte chains incorporated into calcite to a greater extent than particles with only polyelectrolyte chains.⁸⁶ They posit that the hydroxyl (OH⁻) functional groups on their non-polyelectrolyte chains may help increase the residency times of their particles on the calcite surface or disrupt the hydration layers at the crystal surface.

2.5.3 Summary and remaining questions: intermolecular forces

In summary, careful consideration of solution chemistry (pH, ionic strength, monovalent vs. multivalent ions) can generate attractive intermolecular forces between the crystal and particle surfaces and form single crystal composites. Based on the requirements on crystal and particle surfaces described above, we can propose a set of conditions under which particles decorated with organic stabilizer chains are more likely to incorporate. We must take a balanced approach when choosing solution ionic strength. A low ionic strength solution is ideal for a thicker EDL at crystal surface, while a high ionic strength can help promote polyelectrolyte chain collapse, though

multivalent ions at low concentrations can also cause chain collapse. The specific ions in solution may be able to disrupt or at least modify hydration layers at the crystal surface.^{96,116,117} By disrupting the hydration layers, which presented an additional barrier to particle binding, we may promote longer retention times and stronger binding ($k_{\text{on}} > k_{\text{off}}$) of particles at the surface. Non-ionic stabilizer chains might also help disrupt hydration layers and yield stronger binding.

Polyelectrolyte stabilizer chains are a good choice given both their highly charged nature and their ability to collapse and rearrange to accommodate the crystal surface. Until now, studies have not considered the size and shape complementarity of the polymer chains and the steps on the crystal surface. However, in other studies, molecular additives were found to incorporate at distinct growth sites depending on their size, shape and orientation match.^{118–120} Focusing on complementarity of the stabilizer chains is complicated by our still limited understanding of their interactions, in solution and with the crystal surface. For example, we do not have a firm understanding of the optimal chain density at the particle surface. Initial studies suggest that incorporation is lower when the chain density is too high, as neighboring stabilizer chains may cross-link have less conformational degrees of freedom to bind properly to the crystal surface.⁸⁵ Therefore, a better understanding of the types of multivalent interactions between polyelectrolyte brushes and crystal surfaces is necessary.

Thus far, we have focused on the interactions that dictate why the particles incorporate into crystals, but an equally perplexing question is how crystals are able to incorporate particles. Many studies report internal strains generated in single crystals due to the incorporation of additives.^{6,23,57} The ability of these crystals to accommodate

large internal strains challenges our ideas of what was possible in ionic crystal systems. Fewer studies report the effects of incorporation on the particles. Both *in situ* AFM and *ex situ* growth studies have shown that when these polymer particles incorporate into calcite, the particles deform, changing shape from spherical to ellipsoidal particles.^{83,100} The ability of the particle to deform will depend not only on the conformational degrees of freedom of the stabilizer chain, but also on the “core” of the particle, which we have not considered of importance until now. For example, *in situ* AFM studies that used polymer particles with similar stabilizer chains and a stiffer core did not observe any deformation of the particles upon incorporation. We do not yet understand the role that the particle deformation plays in aiding or hindering incorporation into crystals. While all the studies presented here considered relatively soft particles incorporating into relatively hard crystals, a recent study explored the inclusion of hard particles into soft (molecular) crystals.¹²¹ By watching incorporation in real time using *in situ* AFM, they observed that particle inclusion was able to generate screw dislocations, suggesting that in some cases particle incorporation can additionally modify microscopic crystal growth mechanisms.

Most of the studies described in the previous section incorporate the particles into calcite crystals. However, several studies also incorporate stabilizer chain-coated polymer or Fe₃O₄ nanoparticles into ZnO or functionalized Au nanoparticles into Cu₂O.^{60,80,81} Future work should create single crystal composites with other functional crystalline materials by considering the requirements for crystal surfaces outlined above.

2.6 Conclusions

We presented a framework for understanding how particles can become incorporated into single crystals during solution growth. We describe different types of forces that can be used to oppose the large repulsive crystallization pressure that favors additive-free crystal growth. When particles are packed into a template, particle-particle or particle-template normal forces can counter the crystallization pressure by preventing particles from getting pushed ahead of the crystal growth front. For mobile particles in solution, attractive intermolecular forces between the particles and crystal can overcome the crystallization pressure and lead to uniform particle occlusion within single crystals. The particle surface, crystal surface and the solution chemistry each play key roles in generating sufficient attractive intermolecular forces. With the framework presented here we hope we can now move beyond growing single crystal calcite with additives, and instead grow functional composite single crystals.

REFERENCES

- (1) Mullin, J. W. Chapter 7 Recrystallization. In *Crystallization*; Elsevier Science & Technology, 2001.
- (2) Roedder, E. Origin and Significance of Magmatic Inclusions. *Bull. Minéralogique* **1979**, *102*, 487–510.
- (3) Stuart, F. M.; Burnard, P. G.; Taylor, R. P.; Turner, G. Resolving Mantle and Crustal Contributions to Ancient Hydrothermal Fluids: HeAr Isotopes in Fluid Inclusions from Dae Hwa W-Mo Mineralisation, South Korea. *Geochim. Cosmochim. Acta* **1995**, *59* (22), 4663–4673.
- (4) Weber, E.; Pokroy, B. Intracrystalline Inclusions within Single Crystalline Hosts: From Biomineralization to Bio-Inspired Crystal Growth. *CrystEngComm* **2015**, *17* (31), 5873–5883.
- (5) Towe, K. M. Echinoderm Calcite: Single Crystal. *Science*. **1967**, *157*, 8–11.
- (6) Seknazi, E.; Pokroy, B. Residual Strain and Stress in Biocrystals. *Adv. Mater.* **2018**, *1707263*, 1–6.
- (7) Pokroy, B.; Quintana, J. P.; Caspi, E. N.; Berner, A.; Zolotoyabko, E. Anisotropic Lattice Distortions in Biogenic Aragonite. *Nat. Mater.* **2004**, *3*.
- (8) Pokroy, B.; Fitch, A. N.; Marin, F.; Kapon, M.; Adir, N.; Zolotoyabko, E. Anisotropic Lattice Distortions in Biogenic Calcite Induced by Intra-Crystalline Organic Molecules. *J. Struct. Biol.* **2006**, *155* (1), 96–103.
- (9) Pokroy, B.; Fitch, A. N.; Zolotoyabko, E. The Microstructure of Biogenic Calcite: A View by High-Resolution Synchrotron Powder Diffraction. *Adv. Mater.* **2006**, *18* (18), 2363–2368.

- (10) Zolotoyabko, E. Anisotropic Lattice Distortions in Biogenic Minerals Originated from Strong Atomic Interactions at Organic / Inorganic Interfaces. *Adv. Mater. Interfaces* **2017**, *4*, 1600189.
- (11) Li, H.; Xin, H. L.; Kunitake, M. E.; Keene, E. C.; Muller, D. A.; Estroff, L. A. Calcite Prisms from Mollusk Shells (*Atrina Rigida*): Swiss-Cheese-like Organic-Inorganic Single-Crystal Composites. *Adv. Funct. Mater.* **2011**, *21* (11), 2028–2034.
- (12) Polishchuk, I.; Bracha, A. A.; Bloch, L.; Levy, D.; Kozachkevich, S.; Etinger-Geller, Y.; Kauffmann, Y.; Burghammer, M.; Giacobbe, C.; Villanova, J.; et al. Coherently Aligned Nanoparticles within a Biogenic Single Crystal: A Biological Prestressing Strategy. *Science*. **2017**, *358* (6368), 1294–1298.
- (13) Younis, S.; Kauffmann, Y.; Bloch, L.; Zolotoyabko, E. Inhomogeneity of Nacre Lamellae on the Nanometer Length Scale. *Cryst. Growth Des.* **2012**, *12* (9), 4574–4579.
- (14) Gries, K.; Kröger, R.; Kübel, C.; Fritz, M.; Rosenauer, A. Investigations of Voids in the Aragonite Platelets of Nacre. *Acta Biomater.* **2009**, *5* (8), 3038–3044.
- (15) Ma, Y.; Aichmayer, B.; Paris, O.; Fratzl, P.; Meibom, A.; Metzler, R. A.; Politi, Y.; Addadi, L.; Gilbert, P. U. P. A.; Weiner, S. The Grinding Tip of the Sea Urchin Tooth Exhibits Exquisite Control over Calcite Crystal Orientation and Mg Distribution. *Proc. Natl. Acad. Sci.* **2009**, *106* (15), 6048–6053.
- (16) Killian, C. E.; Metzler, R. A.; Gong, Y.; Churchill, T. H.; Olson, I. C.; Trubetskoy, V.; Christensen, M. B.; Fournelle, J. H.; De Carlo, F.; Cohen, S.; et al. Self-Sharpening Mechanism of the Sea Urchin Tooth. *Adv. Funct. Mater.*

- 2011**, *21* (4), 682–690.
- (17) Metzler, R. A.; Tribello, G. A.; Parrinello, M.; Gilbert, P. U. P. A. Asprich
Peptides Are Occluded in Calcite and Permanently Disorder Biomineral Crystals.
J. Am. Chem. Soc. **2010**, *132* (33), 11585–11591.
- (18) Marquis, E. A.; Bachhav, M.; Chen, Y.; Dong, Y.; Gordon, L. M.; McFarland, A.
On the Current Role of Atom Probe Tomography in Materials Characterization
and Materials Science. *Curr. Opin. Solid State Mater. Sci.* **2013**, *17* (5), 217–223.
- (19) Seidman, D. N. Three-Dimensional Atom-Probe Tomography: Advances and
Applications. *Annu. Rev. Mater. Res.* **2007**, *37* (1), 127–158.
- (20) Gordon, L. M.; Joester, D. Nanoscale Chemical Tomography of Buried
Organic-Inorganic Interfaces in the Chiton Tooth. *Nature* **2011**, *469* (7329),
194–198.
- (21) Alberto, P. Preliminary Data on the Nanoscale Chemical Characterization of the
Inter-Crystalline Organic Matrix of a Calcium Carbonate Biomineral. *Minerals*
2018, *8* (223).
- (22) Meldrum, F. C.; Hyde, S. T. Morphological Influence of Magnesium and
Organic Additives on the Precipitation of Calcite. *J. Cryst. Growth* **2001**, *231* (4),
544–558.
- (23) Borukhin, S.; Bloch, L.; Radlauer, T.; Hill, A. H.; Fitch, A. N.; Pokroy, B.
Screening the Incorporation of Amino Acids into an Inorganic Crystalline Host:
The Case of Calcite. *Adv. Funct. Mater.* **2012**, *22* (20), 4216–4224.
- (24) Asenath-Smith, E.; Li, H.; Keene, E. C.; Seh, Z. W.; Estroff, L. a. Crystal
Growth of Calcium Carbonate in Hydrogels as a Model of Biomineralization.

- Adv. Funct. Mater.* **2012**, 22 (14), 2891–2914.
- (25) Berman, A.; Addadi, L.; Weiner, S. Interactions of Sea-Urchin Skeleton Macromolecules With Growing Calcite Crystals - a Study of Intracrystalline Proteins. *Nature* **1988**, 331 (6156), 546–548.
- (26) Albeck, S.; Aizenberg, J.; Addadi, L.; Weiner, S. Interactions of Various Skeletal Intracrystalline Components with Calcite Crystals. *J. Am. Chem. Soc.* **1993**, 115 (25), 11691–11697.
- (27) Liu, C.; Du, J.; Xie, L.; Zhang, R. Direct Observation of Nacre Proteins in the Whole Calcite by Super-Resolution Microscopy Reveals Diverse Occlusion Patterns. *Cryst. Growth Des.* **2017**, 17 (4), 1966–1976.
- (28) Weber, E.; Bloch, L.; Guth, C.; Fitch, A. N.; Weiss, I. M.; Pokroy, B. Incorporation of a Recombinant Biomineralization Fusion Protein into the Crystalline Lattice of Calcite. *Chem. Mater.* **2014**, 26 (17), 4925–4932.
- (29) Green, D. C.; Ihli, J.; Thornton, P. D.; Holden, M. A.; Marzec, B.; Kim, Y. Y.; Kulak, A. N.; Levenstein, M. A.; Tang, C.; Lynch, C.; et al. 3D Visualization of Additive Occlusion and Tunable Full-Spectrum Fluorescence in Calcite. *Nat. Commun.* **2016**, 7, 1–13.
- (30) Sedlák, M.; Antonietti, M.; Cölfen, H. Synthesis of a New Class of Double-Hydrophilic Block Copolymers with Calcium Binding Capacity as Builders and for Biomimetic Structure Control of Minerals. *Macromol. Chem. Phys.* **1998**, 199 (2), 247–254.
- (31) Cölfen, H.; Antonietti, M. Crystal Design of Calcium Carbonate Microparticles Using Double-Hydrophilic Block Copolymers. *Langmuir* **1998**, 14 (3), 582–589.

- (32) Cölfen, H.; Qi, L. A Systematic Examination of the Morphogenesis of Calcium Carbonate in the Presence of a Double-Hydrophilic Block Copolymer. *Chem. - A Eur. J.* **2001**, *7* (1), 106–116.
- (33) Yu, S.-H.; Cölfen, H. Bio-Inspired Crystal Morphogenesis by Hydrophilic Polymers. *J. Mater. Chem.* **2004**, *14* (14), 2124.
- (34) Cölfen, H.; Antonietti, M. Mesocrystals: Inorganic Superstructures Made by Highly Parallel Crystallization and Controlled Alignment. *Angew. Chemie - Int. Ed.* **2005**, *44* (35), 5576–5591.
- (35) Asthana, R.; Tewari, S. N. The Engulfment of Foreign Particles by a Freezing Interface. *J. Mater. Sci.* **1993**, *28* (20), 5414–5425.
- (36) Chernov, A. A.; Temkin, D. E. Capture of Inclusions in Crystal Growth. In *1976 Crystal Growth and Materials*; 1977; pp 4–77.
- (37) Rempel, A. W.; Worster, M. G. Interaction between a Particle and an Advancing Solidification Front. *J. Cryst. Growth* **1999**, *205* (3), 427–440.
- (38) Azouni, M. A.; Casses, P. Thermophysical Properties Effects on Segregation during Solidification. *Adv. Colloid Interface Sci.* **1998**, *75* (2), 83–106.
- (39) Kahr, B.; Shtukenberg, A. G. Dyeing Crystals since 2000. *CrystEngComm* **2016**, *18*, 8988–8998.
- (40) Kahr, B.; Gurney, R. W. Dyeing Crystals. *Chem. Rev.* **2001**, *101*, 893–951.
- (41) Adam, M.; Tietze, R.; Gaponik, N.; Eychmüller, A. QD-Salt Mixed Crystals: The Influence of Salt-Type, Free-Stabilizer, and PH. *Zeitschrift für Phys. Chemie* **2015**, *229* (1–2), 109–118.
- (42) Otto, T.; Müller, M.; Mundra, P.; Lesnyak, V.; Demir, H. V.; Gaponik, N.;

- Eychmüller, A. Colloidal Nanocrystals Embedded in Macrocrystals: Robustness, Photostability, and Color Purity. *Nano Lett.* **2012**, *12* (10), 5348–5354.
- (43) Brovelli, S.; Bae, W. K.; Galland, C.; Giovanella, U.; Meinardi, F.; Klimov, V. I. Dual-Color Electroluminescence from Dot-in-Bulk Nanocrystals. *Nano Lett.* **2014**, *14* (2), 486–494.
- (44) Yang, Z.; Voznyy, O.; Walters, G.; Fan, J. Z.; Liu, M.; Kinge, S.; Hoogland, S.; Sargent, E. H. Quantum Dots in Two-Dimensional Perovskite Matrices for Efficient Near-Infrared Light Emission. *ACS Photonics* **2017**, *4* (4), 830–836.
- (45) Ning, Z.; Gong, X.; Comin, R.; Walters, G.; Fan, F.; Voznyy, O.; Yassitepe, E.; Buin, A.; Hoogland, S.; Sargent, E. H. Quantum-Dot-in-Perovskite Solids. *Nature* **2015**, *523* (7560), 324–328.
- (46) Atwater, H. A.; Polman, A. Plasmonics for Improved Photovoltaic Devices. *Nat. Mater.* **2010**, *9* (3), 205–213.
- (47) Jiang, R.; Li, B.; Fang, C.; Wang, J. Metal/Semiconductor Hybrid Nanostructures for Plasmon-Enhanced Applications. *Adv. Mater.* **2014**, *26* (31), 5274–5309.
- (48) Cushing, S. K.; Wu, N. Progress and Perspectives of Plasmon-Enhanced Solar Energy Conversion. *J. Phys. Chem. Lett.* **2016**, *7* (4), 666–675.
- (49) Khaimov-Mal'kov, V. Y. Growth of Crystals, Vol. 2. In *Growth of Crystals*, vol. 2; Shubnikov, A. V., Sheftal, N. N., Eds.; 1959.
- (50) Newton, I. *Philosophiae Naturalis Principia Mathematica*; 1687.
- (51) Finnemore, A. S.; Scherer, M. R. J.; Langford, R.; Mahajan, S.; Ludwigs, S.; Meldrum, F. C.; Steiner, U. Nanostructured Calcite Single Crystals with Gyroid Morphologies. *Adv. Mater.* **2009**, *21* (38–39), 3928–3932.

- (52) Park, R. J.; Meldrum, F. C. Shape-Constraint as a Route to Calcite Single Crystals with Complex Morphologies. *J. Mater. Chem.* **2004**, *14* (14), 2291–2296.
- (53) Yue, W.; Park, R. J.; Kulak, A. N.; Meldrum, F. C. Macroporous Inorganic Solids from a Biomineral Template. *J. Cryst. Growth* **2006**, *294* (1), 69–77.
- (54) Hetherington, N. B. J.; Kulak, A. N.; Kim, Y. Y.; Noel, E. H.; Snoswell, D.; Butler, M.; Meldrum, F. C. Porous Single Crystals of Calcite from Colloidal Crystal Templates: ACC Is Not Required for Nanoscale Templating. *Adv. Funct. Mater.* **2011**, *21* (5), 948–954.
- (55) Li, X.; Jiang, Y.; Shi, Z.; Xu, Z. Two Growth Modes of Metal Oxide in the Colloidal Crystal Template Leading to the Formation of Two Different Macroporous Materials. *Chem. Mater.* **2007**, *19* (22), 5424–5430.
- (56) Brif, A.; Ankonina, G.; Drathen, C.; Pokroy, B. Bio-Inspired Band Gap Engineering of Zinc Oxide by Intracrystalline Incorporation of Amino Acids. *Adv. Mater.* **2014**, *26* (3), 477–481.
- (57) Brif, A.; Bloch, L.; Pokroy, B. Bio-Inspired Engineering of a Zinc Oxide/Amino Acid Composite: Synchrotron Microstructure Study. *CrystEngComm* **2014**, *16*, 3268–3273.
- (58) Li, X.; Tao, F.; Jiang, Y.; Xu, Z. 3-D Ordered Macroporous Cuprous Oxide: Fabrication, Optical, and Photoelectrochemical Properties. *J. Colloid Interface Sci.* **2007**, *308* (2), 460–465.
- (59) Smith, A. E. A.; Noble, J. M.; Hovden, R.; Uhl, A. M.; Dicorato, A.; Kim, Y.-Y.; Kulak, A. N.; Meldrum, F. C.; Lena, F. Physical Confinement Promoting

- Formation of Cu₂O–Au Heterostructures with Au Nanoparticles Entrapped within Crystalline Cu₂O Nanorods. *Chem. Mater.* **2016**, *29*, 555–563.
- (60) DiCorato, A. E.; Asenath-Smith, E.; Kulak, A. N.; Meldrum, F. C.; Estroff, L. A. Cooperative Effects of Confinement and Surface Functionalization Enable the Formation of Au/Cu₂O Metal–Semiconductor Heterostructures. *Cryst. Growth Des.* **2016**, acs.cgd.6b00913.
- (61) Henisch, H. K. *Crystal Growth in Gels*; Dover Publications, 1996.
- (62) Li, H.; Xin, H. L.; Muller, D. a; Estroff, L. a. Visualizing the 3D Internal Structure of Calcite Single Crystals Grown in Agarose Hydrogels. *Science* **2009**, *326* (5957), 1244–1247.
- (63) Kim, Y.-Y.; Schenk, A. S.; Walsh, D.; Kulak, A. N.; Cespedes, O.; Meldrum, F. C. Bio-Inspired Formation of Functional Calcite/Metal Oxide Nanoparticle Composites. *Nanoscale* **2014**, *6* (2), 852–859.
- (64) Liu, Y.; Yuan, W.; Shi, Y.; Chen, X.; Wang, Y.; Chen, H.; Li, H. Functionalizing Single Crystals : Incorporation of Nanoparticles Inside Gel-Grown Calcite Crystals. *Angew. Chemie - Int. Ed.* **2014**, 4127–4131.
- (65) Liu, Y.; Zang, H.; Wang, L.; Fu, W.; Yuan, W.; Wu, J.; Jin, X.; Han, J.; Wu, C.; Wang, Y.; et al. Nanoparticles Incorporated inside Single-Crystals: Enhanced Fluorescent Properties. *Chem. Mater.* **2016**, *28* (20), 7537–7543.
- (66) Liu, Y.; Zang, H.; Wang, L.; Fu, W.; Yuan, W.; Wu, J.; Jin, X.; Han, J.; Wu, C.; Wang, Y.; et al. Nanoparticles Incorporated inside Single-Crystals: Enhanced Fluorescent Properties. *Chem. Mater.* **2016**, *28*.
- (67) Li, H.; Fujiki, Y.; Sada, K.; Estroff, L. A. Gel Incorporation inside of Organic

- Single Crystals Grown in Agarose Hydrogels. *CrystEngComm* **2011**, *13* (4), 1060–1062.
- (68) Chen, L.; Ye, T.; Jin, X.; Ren, J.; Huang, B.; Xu, Z. K.; Chen, H.; Li, H. Gel Network Incorporation into Single Crystals Grown by Decomplexation Method. *CrystEngComm* **2015**, *17* (42), 8113–8118.
- (69) Hu, C.; Ye, T.; Liu, Y.; Ren, J.; Jin, X.; Chen, H.; Li, H. Pbl₂ Band Gap Engineering by Gel Incorporation. *Mater. Chem. Front.* **2018**, 362–368.
- (70) Ren, J.; Huang, B.; Chen, L.; Liu, Y.; Ye, T.; Liu, W.; Jin, X.; Xu, Z. K.; Chen, H.; Li, H. Constructing Bulk-Contact inside Single Crystals of Organic Semiconductors through Gel Incorporation. *CrystEngComm* **2016**, *18* (5), 800–806.
- (71) Asenath-Smith, E.; Noble, J. M.; Hovden, R.; Uhl, A. M.; DiCorato, A.; Kim, Y.-Y.; Kulak, A. N.; Meldrum, F. C.; Kourkoutis, L. F.; Estroff, L. A. Physical Confinement Promoting Formation of Cu₂O–Au Heterostructures with Au Nanoparticles Entrapped within Crystalline Cu₂O Nanorods. *Chem. Mater.* **2017**, *29* (2), 555–563.
- (72) Lu, C.; Qi, L.; Cong, H.; Wang, X.; Yang, J.; Yang, L.; Zhang, D.; Ma, J.; Cao, W. Synthesis of Calcite Single Crystals with Porous Surface by Templating of Polymer Latex Particles. *Chem. Mater.* **2005**, *17* (20), 5218–5224.
- (73) Muñoz-Espí, R.; Qi, Y.; Lieberwirth, I.; Gómez, C. M.; Wegner, G. Surface-Functionalized Latex Particles as Controlling Agents for the Mineralization of Zinc Oxide in Aqueous Medium. *Chem. - A Eur. J.* **2006**, *12* (1), 118–129.
- (74) Muñoz-Espí, R.; Jeschke, G.; Lieberwirth, I.; Gomez, C. M.; Wegner, G. ZnO-

- Latex Hybrids Obtained by Polymer-Controlled Crystallization: A Spectroscopic Investigation. *J. Phys. Chem. B* **2007**, *111* (4), 697–707.
- (75) Wegner, G.; Baum, P.; Müller, M.; Norwig, J.; Landfester, K. Polymers Designed to Control Nucleation and Growth of Inorganic Crystals from Aqueous Media. *Macromol. Symp.* **2001**, *175*, 349–355.
- (76) Kulak, A. N.; Yang, P.; Kim, Y.-Y. Y.; Armes, S. P.; Meldrum, F. C. Colouring Crystals with Inorganic Nanoparticles. *Chem. Commun.* **2014**, *50*, 67–69.
- (77) Kulak, A. N.; Semsarilar, M.; Kim, Y.; Ihli, J.; Fielding, L. A.; Cespedes, O.; Armes, S. P.; Meldrum, F. C. One-Pot Synthesis of an Inorganic Heterostructure: Uniform Occlusion of Magnetite Nanoparticles within Calcite Single Crystals. *Chem. Sci.* **2014**, 738–743.
- (78) Hendley IV, C. T.; Fielding, L. A.; Jones, E. R.; Ryan, A. J.; Armes, S. P.; Estroff, L. A. Mechanistic Insights into Diblock Copolymer Nanoparticle – Crystal Interactions Revealed via in Situ Atomic Force Microscopy. *J. Am. Chem. Soc.* **2018**, *140*, 7936–7945.
- (79) Kim, Y.-Y.; Ganesan, K.; Yang, P.; Kulak, A.; Borukhin, S.; Pechook, S.; Ribeiro, L.; Kroger, R.; Eichhorn, S. An Artificial Biomineral Formed by Incorporation of Copolymer Micelles in Calcite Crystals. *Nat. Mater.* **2011**, *10* (11), 890–896.
- (80) Ning, Y.; Fielding, L. A.; Andrews, T. S.; Growney, D. J.; Armes, S. P. Sulfate-Based Anionic Diblock Copolymer Nanoparticles for Efficient Occlusion within Zinc Oxide. *Nanoscale* **2015**, *7* (15), 6691–6702.
- (81) Kulak, A. N.; Grimes, R.; Kim, Y. Y.; Semsarilar, M.; Anduix-Canto, C.;

- Cespedes, O.; Armes, S. P.; Meldrum, F. C. Polymer-Directed Assembly of Single Crystal Zinc Oxide/Magnetite Nanocomposites under Atmospheric and Hydrothermal Conditions. *Chem. Mater.* **2016**, *28* (20), 7528–7536.
- (82) Ning, Y.; Fielding, L. A.; Doncom, K. E. B.; Penfold, N. J. W.; Kulak, A. N.; Matsuoka, H.; Armes, S. P. Incorporating Diblock Copolymer Nanoparticles into Calcite Crystals: Do Anionic Carboxylate Groups Alone Ensure Efficient Occlusion? *ACS Macro Lett.* **2016**, *5* (3), 311–315.
- (83) Kim, Y. Y.; Semsarilar, M.; Carloni, J. D.; Cho, K. R.; Kulak, A. N.; Polishchuk, I.; Hendley, C. T.; Smeets, P. J. M.; Fielding, L. A.; Pokroy, B.; et al. Structure and Properties of Nanocomposites Formed by the Occlusion of Block Copolymer Worms and Vesicles Within Calcite Crystals. *Adv. Funct. Mater.* **2016**, *26* (9), 1382–1392.
- (84) Hanisch, A.; Yang, P.; Kulak, A. N.; Fielding, L. A.; Meldrum, F. C.; Armes, S. P. Phosphonic Acid-Functionalized Diblock Copolymer Nano-Objects via Polymerization-Induced Self-Assembly: Synthesis, Characterization, and Occlusion into Calcite Crystals. *Macromolecules* **2016**, *49* (1), 192–204.
- (85) Ning, Y.; Fielding, L. A.; Ratcliffe, L. P. D.; Wang, Y. W.; Meldrum, F. C.; Armes, S. P. Occlusion of Sulfate-Based Diblock Copolymer Nanoparticles within Calcite: Effect of Varying the Surface Density of Anionic Stabilizer Chains. *J. Am. Chem. Soc.* **2016**, *138* (36), 11734–11742.
- (86) Kim, Y.-Y.; Fielding, L. A.; Kulak, A. N.; Nahi, O.; Mercer, W.; Jones, E. R.; Armes, S. P.; Meldrum, F. C. Influence of the Structure of Block Copolymer Nanoparticles on the Growth of Calcium Carbonate. *Chem. Mater.* **2018**, *30* (20),

7091–7099.

- (87) Chernov, A. A. *Modern Crystallography III: Crystal Growth*; Springer-Verlag, 1984.
- (88) Starov, V. M. *Encyclopedia of Microfluidics and Nanofluidics*. **2013**, 1–9.
- (89) Derjaguin, B. V.; Churaev, N. V. On the Question of Determining the Concept of Disjoining Pressure and Its Role in the Equilibrium and Flow of Thin Films. *J. Colloid Interface Sci.* **1978**, *66* (3), 389–398.
- (90) Raitchenko, A. I.; Mukai, K. Theory of Interaction between a Solid Inclusion in a Liquid with Nonuniform Viscosity with an Advancing Solidification Front
Theory of Interaction between a Solid Inclusion in a Liquid with Nonuniform Viscosity with an Advancing Solidification Front. **1999**, 2291.
- (91) De La Pierre, M.; Raiteri, P.; Stack, A. G.; Gale, J. D. Uncovering the Atomistic Mechanism for Calcite Step Growth. *Angew. Chemie - Int. Ed.* **2017**, *56* (29), 8464–8467.
- (92) Diao, Y.; Espinosa-Marzal, R. M. Molecular Insight into the Nanoconfined Calcite–solution Interface. *Proc. Natl. Acad. Sci.* **2016**, *113* (43), 12047–12052.
- (93) Söngen, H.; Reischl, B.; Miyata, K.; Bechstein, R.; Raiteri, P.; Rohl, A. L.; Gale, J. D.; Fukuma, T.; Kühnle, A. Resolving Point Defects in the Hydration Structure of Calcite (10.4) with Three-Dimensional Atomic Force Microscopy. *Phys. Rev. Lett.* **2018**, *120* (11), 116101.
- (94) Kobayashi, K.; Oyabu, N.; Kimura, K.; Ido, S.; Suzuki, K.; Imai, T.; Tagami, K.; Tsukada, M.; Yamada, H. Visualization of Hydration Layers on Muscovite Mica in Aqueous Solution by Frequency-Modulation Atomic Force Microscopy. *J.*

- Chem. Phys.* **2013**, *138* (18).
- (95) Pashley, R. M.; Israelachvili, J. N. Molecular Layering of Water in Thin Films between Mica Surfaces and Its Relation to Hydration Forces. *J. Colloid Interface Sci.* **1984**, *101* (2), 511–523.
- (96) Zachariah, Z.; Espinosa-Marzal, R. M.; Heuberger, M. P. Ion Specific Hydration in Nano-Confined Electrical Double Layers. *J. Colloid Interface Sci.* **2017**, *506*, 263–270.
- (97) Dorvee, J. R.; Veis, A. Water in the Formation of Biogenic Minerals: Peeling Away the Hydration Layers. *J. Struct. Biol.* **2013**, *183* (2), 278–303.
- (98) Israelachvili, J. N. Electrostatic Forces between Surfaces in Liquids; 2011; pp 291–340.
- (99) Vekilov, P. G. Incorporation at Kinks: Kink Density and Activation Barriers. *AIP Conf. Proc.* **2007**, *916*, 235–267.
- (100) Cho, K. R.; Kim, Y.; Yang, P.; Cai, W.; Pan, H.; Kulak, A. N.; Lau, J. L.; Kulshreshtha, P.; Armes, S. P.; Meldrum, F. C.; et al. Direct Observation of Mineral-Organic Composite Formation Reveals Occlusion Mechanism. *Nat. Commun.* **2016**, *7*, 1–7.
- (101) DeYoreo, J. J.; Vekilov, P. G. Principles of Crystal Nucleation and Growth. *Rev. Mineral. Geochemistry* **2003**, *54* (1), 57–93.
- (102) Van Enkevort, W. J. P.; Los, J. H. “Tailor-Made” Inhibitors in Crystal Growth: A Monte Carlo Simulation Study. *J. Phys. Chem. C* **2008**, *112* (16), 6380–6389.
- (103) Sleutel, M.; Lutsko, J.; Van Driessche, A. E. S. Mineral Growth beyond the Limits of Impurity Poisoning. *Cryst. Growth Des.* **2018**, *18* (1), 171–178.

- (104) Qiu, S. R.; Wierzbicki, A.; Orme, C. A.; Cody, A. M.; Hoyer, J. R.; Nancollas, G. H.; Zepeda, S.; De Yoreo, J. J. Molecular Modulation of Calcium Oxalate Crystallization by Osteopontin and Citrate. *Proc. Natl. Acad. Sci.* **2004**, *101* (7), 1811–1815.
- (105) Lu, G.; Li, S.; Guo, Z.; Farha, O. K.; Hauser, B. G.; Qi, X.; Wang, Y.; Wang, X.; Han, S.; Liu, X.; et al. Imparting Functionality to a Metal-Organic Framework Material by Controlled Nanoparticle Encapsulation. *Nat. Chem.* **2012**, *4* (4), 310–316.
- (106) Sindoro, M.; Feng, Y.; Xing, S.; Li, H.; Xu, J.; Hu, H.; Liu, C.; Wang, Y.; Zhang, H.; Shen, Z.; et al. Triple-Layer (Au@Perylene)@polyaniline Nanocomposite: Unconventional Growth of Faceted Organic Nanocrystals on Polycrystalline Au. *Angew. Chemie - Int. Ed.* **2011**, *50* (42), 9898–9902.
- (107) Addadi, L.; Weiner, S. Interactions between Acidic Proteins and Crystals: Stereochemical Requirements in Biomineralization. *Proc. Natl. Acad. Sci. U. S. A.* **1985**, *82* (12), 4110–4114.
- (108) Addadi, L.; Joester, D.; Nudelman, F.; Weiner, S. Mollusk Shell Formation: A Source of New Concepts for Understanding Biomineralization Processes. *Chemistry* **2006**, *12* (4), 980–987.
- (109) Israelachvili, J. N. Unifying Concepts in Intermolecular and Interparticle Forces. In *Intermolecular and Surface Forces*; 2011.
- (110) Ning, Y.; Fielding, L. a; Andrews, T. S.; Growney, D.; Armes, S. P. Sulfate-Based Anionic Diblock Copolymer Nanoparticles for Efficient Occlusion within Zinc Oxide. *Nanoscale* **2015**.

- (111) Ballauff, M.; Borisov, O. Polyelectrolyte Brushes. *Curr. Opin. Colloid Interface Sci.* **2006**, *11* (6), 316–323.
- (112) Parnell, A. J.; Martin, S. J.; Dang, C. C.; Geoghegan, M.; Jones, R. A. L.; Crook, C. J.; Howse, J. R.; Ryan, A. J. Synthesis, Characterization and Swelling Behaviour of Poly(Methacrylic Acid) Brushes Synthesized Using Atom Transfer Radical Polymerization. *Polymer (Guildf)*. **2009**, *50* (4), 1005–1014.
- (113) Zhulina, E. B.; Borisov, O. V.; Birshtein, T. M. Polyelectrolyte Brush Interaction with Multivalent Ions. *Macromolecules* **1999**, *32* (24), 8189–8196.
- (114) Yu, J.; Jackson, N. E.; Xu, X.; Morgenstern, Y.; Kaufman, Y.; Ruths, M.; de Pablo, J. J.; Tirrell, M. Multivalent Counterions Diminish the Lubricity of Polyelectrolyte Brushes. *Science*. **2018**, *360* (6396), 1434–1438.
- (115) Brettmann, B. K.; Laugel, N.; Hoffmann, N.; Pincus, P.; Tirrell, M. Bridging Contributions to Polyelectrolyte Brush Collapse in Multivalent Salt Solutions. *J. Polym. Sci. Part A Polym. Chem.* **2016**, *54* (2), 284–291.
- (116) Espinosa-Marzal, R. M.; Drobek, T.; Balmer, T.; Heuberger, M. P. Hydrated-Ion Ordering in Electrical Double Layers. *Phys. Chem. Chem. Phys.* **2012**, *14* (17), 6085–6093.
- (117) Kilpatrick, J. I.; Loh, S. H.; Jarvis, S. P. Directly Probing the Effects of Ions on Hydration Forces at Interfaces. *J. Am. Chem. Soc.* **2013**, *135* (7), 2628–2634.
- (118) Elhadj, S.; Salter, E. A.; Wierzbicki, A.; De Yoreo, J. J.; Han, N.; Dove, P. M. Peptide Controls on Calcite Mineralization: Polyaspartate Chain Length Affects Growth Kinetics and Acts as a Stereochemical Switch on Morphology. *Cryst. Growth Des.* **2006**, *6* (1), 197–201.

- (119) De Yoreo, J. J.; Chung, S.; Friddle, R. W. IN Situ Atomic Force Microscopy as a Tool for Investigating Interactions and Assembly Dynamics in Biomolecular and Biomineral Systems. *Adv. Funct. Mater.* **2013**, *23* (20), 2525–2538.
- (120) Orme, C. A.; Noy, A.; Wierzbicki, A.; McBride, M. T.; Grantham, M.; Teng, H. H.; Dove, P. M.; DeYoreo, J. J. Formation of Chiral Morphologies through Selective Binding of Amino Acids to Calcite Surface Steps. *Nature* **2001**, *411* (6839), 775–779.
- (121) Zhong, X.; Shtukenberg, A. G.; Hueckel, T.; Kahr, B.; Ward, M. D. Screw Dislocation Generation by Inclusions in Molecular Crystals. *Cryst. Growth Des.* **2018**, *18* (1), 318–323.

CHAPTER 3

TOWARDS A GENERALIZABLE, CONFINEMENT-BASED APPROACH TO SEMICONDUCTOR/PLASMONIC NANOPARTICLE COMPOSITES*

3.1 Introduction

Semiconductors are the workhorses of many modern optoelectronic applications, like photocatalysis and photovoltaics, based on their ability to absorb light and convert it to electricity. For many semiconductors, however, the absorption of visible light is low, leading to less efficient energy conversion. To increase absorption, plasmonic nanoparticles, typically Au, Ag or Cu, can be introduced into the semiconducting structures. Plasmonic nanoparticles have a unique property called the localized surface plasmon resonance (LSPR), which causes the particles to strongly absorb light at that resonant wavelength and to have locally enhanced electric fields in their vicinity. Therefore, when plasmonic nanoparticles and semiconductors are combined, they have the potential to increase both the overall absorption as well as energy conversion compared to a pure semiconductor.¹⁻⁵

The degree to which the optoelectronic properties of the semiconductor/plasmonic nanoparticle composite are enhanced is directly tied to the physical integration of the plasmonic nanoparticles and the semiconductor.^{6,7} There are two typical semiconductor/plasmonic nanoparticle morphologies, nanoparticle-

* Co-contributors to this chapter include Jeffrey Zheng, who performed most of the ZnO growths.

decorated structures and core-shell nanoparticles, but both have significant limitations on the degree to which the absorption and energy transfer can be enhanced.

To form nanoparticle-decorated structures, plasmonic nanoparticles are attached using ligands to the surface of pre-formed semiconductor nanostructures.⁸⁻¹⁰ This approach is versatile and simple as the nanoparticles and semiconductors can be synthesized separately and there are a limitless number of combinations one can create. A generalizable method like this approach is useful because the choice of specific semiconductor and plasmonic nanoparticle will determine the types of photocatalysis or photosynthesis applications where they can be applied. The ligands used to attach the two materials, however, present an insulating barrier that could prevent effective energy transfer of light absorbed by the plasmonic nanoparticle into the semiconductor. Additionally, in some studies where particle loading on the semiconductor surface was too high, light absorption by the semiconductor actually decreases compared to a semiconductor with fewer plasmonic nanoparticles.⁹

For core-shell nanoparticles, typically a single plasmonic nanoparticle is encapsulated within a thin semiconducting shell. A large body of work has explored the synthesis of such structures, including variations like eccentric core-shell nanoparticles or Janus nanoparticles.¹¹⁻²² However, new chemistries must be developed to grow core-shell particles using different combinations of materials, making it a less generalizable method than decorating semiconductors with nanoparticles. The geometry of the core-shell particle does allow for the synergistic optoelectronic properties of the plasmonic nanoparticle and the semiconducting shell to shine, as the two are in intimate contact and can reap the benefits of the enhanced

electric fields and potential for energy transfer.^{23,24} But with only one plasmonic nanoparticle and only a small volume of semiconductor per core-shell particle, the maximum increase in absorbed light is limited. Numerous recent studies have brought light to the collective resonant behavior that emerges when multiple plasmonic nanoparticles are assembled into arrays (either ordered or disordered).^{5,25-32} Therefore, a composite architecture in which multiple nanoparticles can be incorporated into a crystalline host without the insulating barriers associated with ligands could allow us to further enhance optoelectronic performance.

Biomaterials provide numerous examples of composite crystals, where second phases are incorporated within single crystalline domains, thereby imparting improved functionality to the composite compared to pure single crystal.³³⁻³⁷ There are a few examples in biology where nanoparticle-like additives are present within the single crystal matrix.^{33,37} If we could learn how biology is able to grow these single crystal composites, then perhaps we could grow semiconductor/plasmonic nanoparticle composites with this type of morphology. It is still not well understood, however, how particle-sized additives, which are orders of magnitude larger than the unit cell dimensions, can incorporate into crystals without disrupting their single crystallinity. (This topic is covered at length in chapter 2). In short, a growing crystal exerts a repulsive crystallization pressure on its environment, which favors expulsion of all additives or particles from the growing crystal.³⁸ If other forces can be introduced to counter the crystallization pressure, however, then additives or particles should be incorporated into the growing crystal. There are two main strategies for countering the crystallization pressure, tuning intermolecular forces to generate large attractive forces

between crystal and particle or using normal forces to immobilize particles and thereby counterbalance the crystallization pressure.

One strategy to create single crystal composites is to use attractive intermolecular forces between particles and crystal that dominate the repulsive crystallization pressure. The earliest work on the subject was largely trial-and-error in its screening of which charged ligands adsorbed on polymer microparticles could enable incorporation into both calcite and zinc oxide.³⁹⁻⁴³ In the last decade, systematic studies varying the polyelectrolyte stabilizer chains that surrounding either a polymer or inorganic particle have advanced our understanding of the design rules for incorporation.⁴⁴⁻⁵⁵ For example, anionic polyelectrolyte stabilizer chains are effective at promoting incorporation into calcite, though recent work suggests that non-ionic stabilizer chains play a key role in dictating particle-crystal interactions too.^{50,51} Largely, these studies have focused on incorporating polymer particles into calcite. Only a few studies, however, explored composites with potentially “functional” electronic properties, though in most cases either the particle or the crystal is “functional” and therefore the electronic properties remain largely unaltered.^{44,46,53,55} Although attractive intermolecular forces can be used successfully to generate single crystal composites, there is still an element of trial-and-error associated with determining the unique stabilizer chain chemistry required to promote incorporation of a specific particle type into a specific crystal. For an application of semiconductor/plasmonic nanoparticle composites, the presence of stabilizer chains at the interface between the particle and crystal presents an insulating barrier that could prevent energy transfer between the two. (Without stabilizer chains on the particles,

they are prone to aggregation in the growth solution.)

An alternate strategy to create single crystal composites uses normal forces to immobilize particles and thereby counterbalance the crystallization pressure. As described previously, the crystallization pressure prefers to continually push mobile particles ahead of the advancing crystallization front.³⁸ If the particles are loaded into a strong hydrogel, however, then the normal forces provided by the semi-rigid template can prevent the particles from getting pushed away from the crystal and instead result in incorporation.⁵⁶⁻⁵⁸ The same hydrogel could be used to incorporate particles of varying composition, size and shape into calcite crystals, indicating that this approach is more easily generalizable to different pairings of particle/crystal than the approach of using intermolecular forces. Thus far, hydrogels have only been used to occlude particles into calcite crystals, though when particles were immobilized by assembly into colloidal crystal packings, they were successfully incorporated into calcite or cuprite (Cu_2O) crystals.^{59,60} Therefore, it seems that inter-particle normal forces can also be used to counter the repulsive crystallization pressure. The composites generated using normal forces once again tend to be composed of either an electronically “functional” crystal or nanoparticles, but never both. This approach has the potential to generate composites where the particles and crystal are in intimate contact, possibly allowing for better energy transfer and more enhanced optical absorption compared to composites where polymer chains exist at the interface.

Recent work from our group showed that physical confinement could be used to grow cuprite (Cu_2O) nanorods with entrapped gold nanoparticles (Au NPs).⁶¹ Briefly, Au NPs are loaded into a polycarbonate track-etched membrane via vacuum-

filtration, which is then placed into the Cu₂O growth solution. During growth, the Cu₂O crystals encapsulate the immobilized Au NP arrays forming composite Cu₂O/Au NP nanorods, which can be isolated by dissolving the membrane. We found that the Au nanoparticles became incorporated without disrupting the crystalline lattice of the Cu₂O demonstrating the promise of this approach for a new semiconductor/plasmonic nanoparticle heterostructure geometry where multiple plasmonic nanoparticles are encapsulated within a semiconducting crystal.

In this work, we demonstrate the generalizability of this physical confinement-based approach to form other composite pairs. To extend this strategy to grow other semiconducting nanorod materials, we first investigated the growth mechanism for Cu₂O nanorod formation and then translated that knowledge to grow ZnO nanorods within the membrane pores. To entrap other plasmonic nanoparticle materials, we studied the mechanism for Au nanoparticle trapping within the membrane pores. We explored the forces that immobilize particles and aid in their incorporation into the crystalline nanorods. This work presents the first steps towards a fully generalizable physical confinement-based approach that can grow many additional pairings of nanoparticles and crystals.

3.2 Experimental Methods

3.2.1 Materials

All materials are used without further purification. Copper (II) sulfate pentahydrate (98%, Sigma-Aldrich), Sodium citrate tribasic dihydrate (>98%, Sigma-Aldrich), Sodium hydroxide pellets (99.2%, Fisher), Hydrazine hydrate (78-82%, Sigma-

Aldrich), Zinc nitrate hexahydrate (98%, Sigma-Aldrich), Ammonium hydroxide solution (28-30%, VWR), Dichloromethane (DCM, 99.8%, Sigma-Aldrich), Ethanol (100%, Pharmco-Aaper), Gold (III) chloride trihydrate (99.99%, Aldrich), Polycarbonate track-etched membranes (Whatman Nuclepore™, 25 mm membrane diameter, 0.05 μm pore size).

3.2.2 Growth of Cu₂O/Au NP composites in track-etched membranes

Crystallization of Cu₂O/Au NP composites was performed using previously developed and published methods from our group.⁶¹ Briefly, Au nanoparticles are loaded into track-etched membranes by vacuum filtration. The nanoparticle-loaded membranes are degassed under vacuum prior to growth of Cu₂O by vapor diffusion of hydrazine hydrate into a modified Fehlings solution. Here, we highlight the only two differences between the methods used here and the previously published methods. The first difference relates to optimizing the time and temperature of the growth chamber for consistent, phase-pure Cu₂O growth. In this work, we used a slightly larger amount of hydrazine (3.5 mL of 80.2% hydrazine hydrate with 16.5 mL water) and a reactor internal temperature of 64 °C, a growth time of 9 hours, and at which point the membrane is red colored and the growth solution clear. The second difference relates to the amount of time that the nanoparticle loaded membranes were degassed prior to growth and in what solution composition. In the previous work, first the copper sulfate, sodium citrate and sodium hydroxide were mixed, triggering the start of growth. Immediately following mixing, the nanoparticle loaded membrane is added to the growth solution and degassed under vacuum for one hour. At the end of the hour, the solution is visibly cloudy. Here, in some cases, we degas the nanoparticle-loaded

membrane under vacuum in a solution that only contains copper sulfate solution overnight (12-15 hours). We use a stir bar as a weight to keep the membrane from floating to the solution/air interface during this extended degas time. Following degassing, in a new vial, we mix the copper sulfate, sodium citrate and sodium hydroxide, immediately add the membrane and begin the growth.

3.2.3 Growth of ZnO/Au NP composites in track-etched membranes

For the growth of ZnO, we first degas the membrane in a zinc nitrate solution. Then using a similar vapor diffusion set up as for our Cu₂O growth, we vapor diffuse a 1.44 wt% ammonium hydroxide solution into a 50 mM zinc nitrate solution at 60 °C for 24 hours.

3.2.4 Powder x-ray diffraction (XRD)

Phase analysis was performed via powder x-ray diffraction using a Bruker D8 Advance ECO powder diffractometer with Cu K α radiation, operating at 40 kV and 25 mA with a scan rate of 0.25°/minute.

3.2.5 Scanning electron microscopy (SEM)

Scanning electron microscopy was performed using a Mira3 LM field emission scanning electron microscopy (SEM) at 10 keV. All samples are carbon coated prior to imaging to prevent charging. The polycarbonate membrane surface is especially prone to charging, so silver paint is also applied to the edges of a small cut portion of the membrane prior to SEM imaging.

For SEM analysis, we often compare the as-grown membrane surface, where bulk crystals are often still attached to the membrane, to a scraped membrane surface, where the bulk crystals have already been removed. Additionally, we frequently

compare the secondary electron (SE) and backscattered electron (BSE) images in order to gain information about both topography and atomic number, Z , of our samples.

3.2.6 Transmission electron microscopy (TEM)

Bright-field transmission electron microscopy is performed using a FEI T12 Spirit TEM at 120 kV. α -tilt was used to view nanorods from multiple angles.

3.2.7 UV/Vis spectroscopy

Optical absorption of the Au NP solution was measured from 300-700 nm using a Cary 5000 UV-Vis-NIR Spectrophotometer.

3.3 Results

Before tackling the growth of other pairings of semiconducting crystals and plasmonic nanoparticles in a composite nanorods, we first consider the growth of bare Cu_2O semiconducting rods within the membrane pores. When an empty track-etched membrane containing no Au NPs is placed in the cuprite growth solution, Cu_2O forms, as demonstrated by powder x-ray diffraction (pXRD) of the membrane and by the distinctive red color of the Cu_2O phase. (Fig. 3.1) When the nanorods are isolated from the polymer membrane, we find Cu_2O nanorods that are 108 ± 15 nm in diameter and 859 ± 491 nm long ($N=114$). (Fig. 3.2a)

To understand the mechanism of nanorod formation within the membrane pores, we took a closer look at the membrane surface. Scanning electron microscopy of the as-grown, un-scraped, membrane surface shows many faceted, bulk cuprite crystals on the surface of the membrane (Fig. 3.2b). It is hard to find any membrane pores on the un-scraped membrane surface that appear to contain rods. Upon scraping

the membrane surface using weigh paper, the bulk crystals are removed from the membrane. Imaging the scraped membrane surface using backscattered electrons

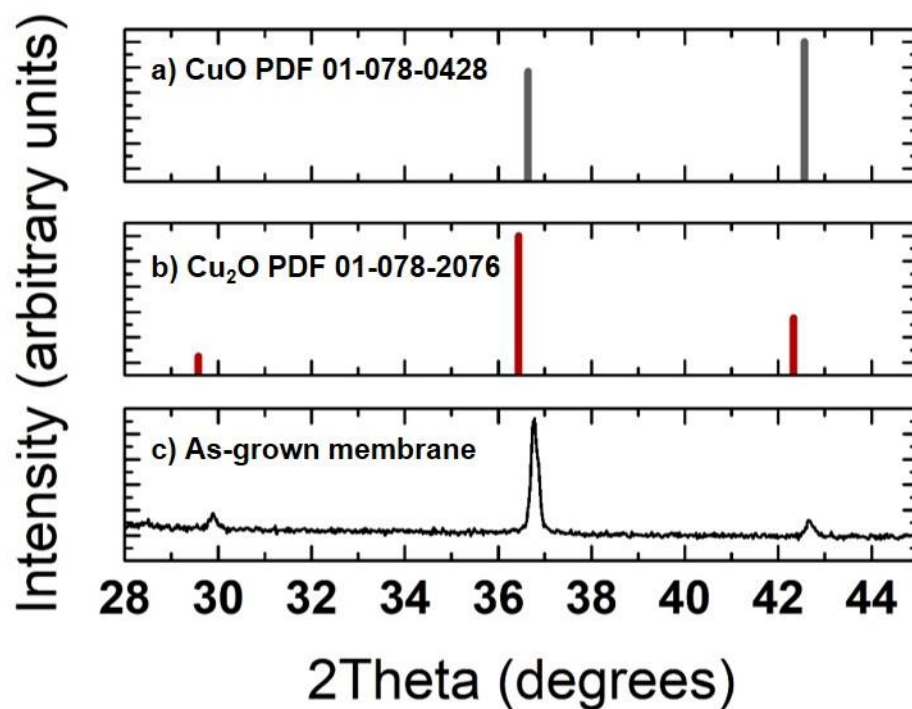


Figure 3.1. Phase analysis via powder x-ray diffraction of crystals grown in track-etched membranes. Standard PDFs for two copper oxide phases (a) CuO and (b) Cu₂O are nearly identical except for the presence of a small peak at 29.6° for Cu₂O that is absent in CuO. (c) XRD of the as-grown membrane surface shows a good match to the PDF pattern

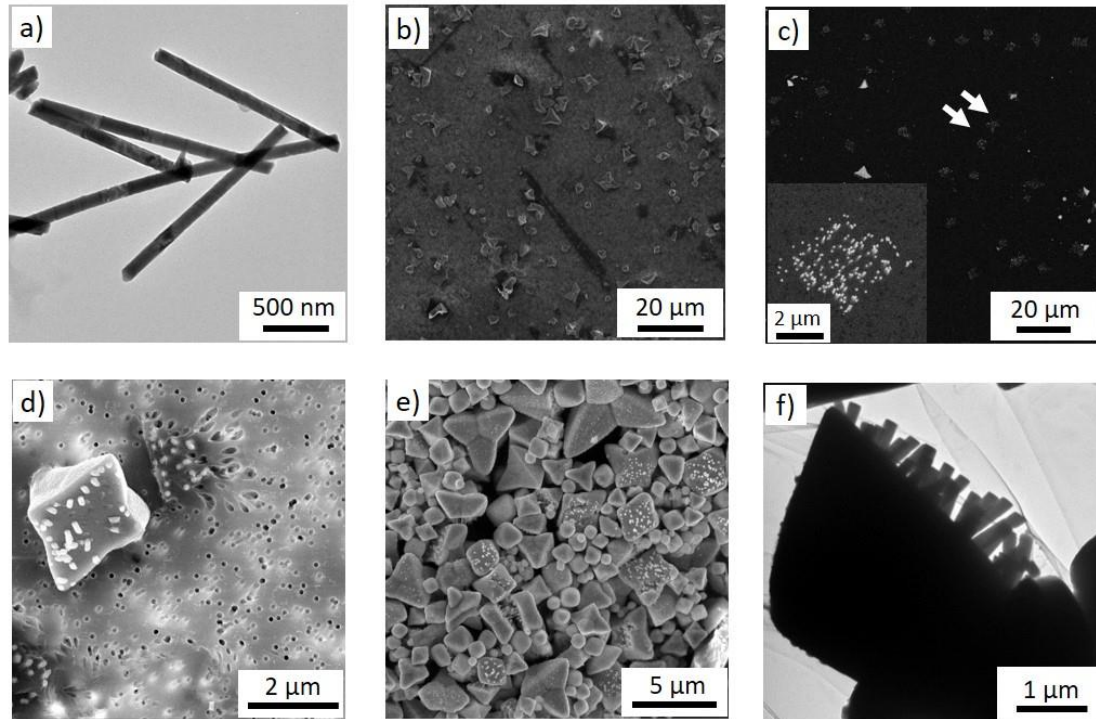


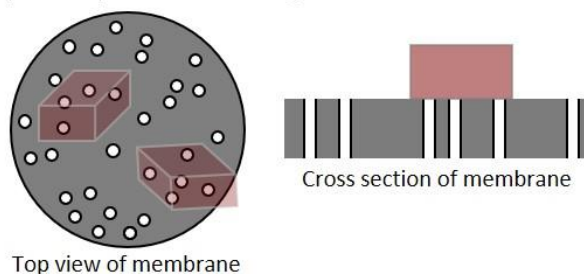
Figure 3.2. (a) TEM of bare Cu_2O nanorods dissolved from the track-etched membrane in which they were grown. (b) SEM imaging shows many faceted, bulk Cu_2O crystals on the un-scraped membrane surface following the growth of Cu_2O oxide, but no nanorods are visible. (c) Backscattered electron imaging of the scraped membrane surface reveals discrete, faceted, light-colored patches (arrows). A zoom in on one patch (inset) reveals that it is composed of white spots, each of which is a single Cu_2O nanorod filling a membrane pore. (d) SEM of a bulk Cu_2O crystal that has flipped over and is sitting next to the region of the membrane where it likely grew. Many nanorods are still attached to the bulk Cu_2O crystal, though some nanorods have broken off of the bulk crystal and are still located within the membrane pores. A region of membrane pores, which likely contained the nanorods that are still attached to the bulk crystal, appear distorted. (e) SEM of the bulk crystals collected after dissolving away an un-scraped membrane. By not scraping the membrane, we can see many nanorods that are attached to flat facets of the bulk crystals. (f) TEM of a single bulk Cu_2O crystal with many nanorods attached.

(BSE) shows many fewer bulk crystals sitting on the membrane surface, and reveals patches of brighter dots, indicating higher Z materials than the carbon membrane (Fig. 3.2c). In the BSE image, each dot corresponds to a membrane pore filled with a cuprite rod (Fig. 3.2c). Further, the patches of rods appear somewhat faceted in their shape.

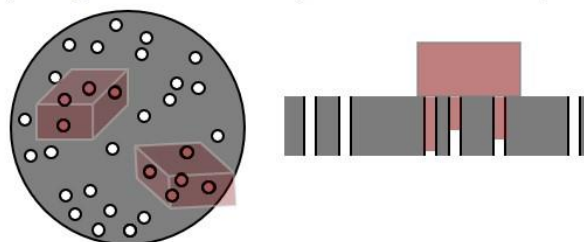
A closer look at a region of the scraped membrane surface provides insight into the mechanism for rod growth. A bulk cuprite crystal was dislodged during scraping, but rather than being fully removed, it flipped over and remained on the membrane surface providing a unique snapshot into the growth mechanism. The bulk crystal contains a number of rods extending from its flat facet. The region of the membrane to the right of the crystal contains filled pores, as indicated by their light color (Fig. 3.2d). When the as-grown, un-scraped membrane is dissolved, and the crystals imaged with SEM or TEM, we see many bulk crystals that contain nanorods extending off of flat facets (Fig. 3.2e,f).

We hypothesize that the rods form by an overgrowth off of crystals formed in the bulk. Due to the high pore density of these membranes, each micron-sized, faceted, bulk crystal covers dozens of membrane pores when it falls to the membrane surface (Fig. 3.3). As growth continues, overgrowth off the bulk crystals occurs into the cylindrical membrane pores, thus templating nanorod growth. This overgrowth mechanism explains why in the backscattered electron images, we observe only patches of rods because rods only form off of the faceted cuprite bulk crystals. If the rods did not form by overgrowth off of bulk crystals, but instead by heterogeneous nucleation within the membrane pores, we would expect to see some isolated pores

a) Bulk crystals fall onto or grow on membrane surface



b) Overgrowth off of bulk crystals into membrane pores



c) Nanorods remain after removal of bulk crystals

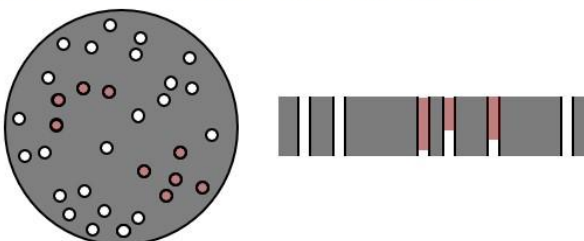


Figure 3.3. Proposed mechanism for membrane templated nanorod growth shown schematically via top view and cross section of the track-etched membrane. (a) Bulk crystals grow on the membrane surface or grow in solution and fall onto the membrane surface, where they cover a number of pores. (b) When growth continues off of the bulk crystals and into the membrane pores, nanorods that are templated by the high aspect ratio, cylindrical pores are formed. (c) After we scrape away the bulk crystals on the membrane surface, we are left only with nanorods in the membrane pores, which we can collect by dissolving the membrane.

containing rods, but we see none. When track-etched membranes with larger or smaller pore diameters were used, we still find that nanorods appear to form via an overgrowth mechanism off of bulk crystals (Fig. 3.4).

When expanding our approach to grow nanorods of other crystalline materials, we hypothesize that any material that grows large, faceted crystals will overgrow nanorods within the membrane pores. Additionally, we require mild synthesis conditions as polycarbonate membranes pores distort above 130 °C (not shown), and the membranes dissolve entirely in high pH solutions and in many organic solvents.⁶² Therefore, we chose zinc oxide (ZnO) as a second target rod material as it can form micron-sized faceted crystals in water at 50-70 °C. After optimizing the solution conditions, we grew hexagonal ZnO prisms, where the hexagonal facets were > 0.5 μm in diameter. When a membrane is introduced into the growth solution and the un-scraped membrane is imaged in the SEM, interestingly we largely see the hexagonal ends of the bulk ZnO crystals on the membrane surface (Fig. 3.5a). After scraping the membrane surface and imaging using BSE, we once again see a patchy distribution of rods (white spots) within the membrane pores (Fig. 3.5b). While the patches of the Cu₂O rods were more discrete, the patches of the ZnO rods appear more irregular, likely because of the way the bulk ZnO crystals sometimes form in clusters (Fig. 3.5a). Similar to the Cu₂O growth, when the as-grown, un-scraped membrane is dissolved, and the crystals are imaged using TEM, we see bulk crystals that contain ZnO nanorods extending off of them (Fig. 3.5c). When the scraped membrane was dissolved, we could isolate collections of bare ZnO nanorods (Fig. 3.5d).

After successfully growing ZnO nanorods within the membrane pores, we next

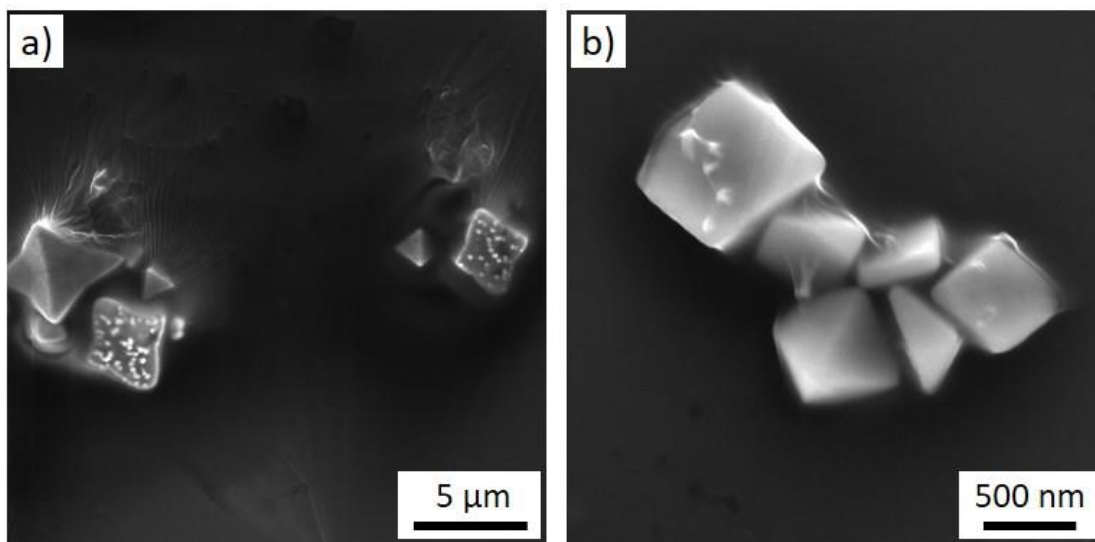


Figure 3.4. SEM of Cu_2O crystals from dissolved, un-scraped, track-etched, polycarbonate membranes with (a) “200 nm” pore size and (b) 30 nm pore size. In both cases, we see nanorods (lighter spots) extending off of the flat facets of bulk crystals. In these images, the membrane was poorly dissolved so we see a large amount of dissolved membrane residue coating the crystals.

wanted to know whether these ZnO rods could also entrap Au NP arrays like the Cu₂O nanorods. After loading the membrane pores with Au NPs and placing the loaded membrane in the ZnO growth solution, we found we were able to grow ZnO/Au NP composite nanorods (Fig. 3.5e).

Thus far, we have successfully incorporated Au NP arrays into both Cu₂O and ZnO nanorods. To put other types of nanoparticles into our Cu₂O or ZnO nanorods, we first needed to better understand the mechanism by which our Au NPs are getting trapped within the membrane pores. It is extremely challenging, however, to characterize the loading of nanoparticles into membrane pores due to the small size scale of the nanoparticles.

SEM images of the loaded membrane surface provide us with snapshot of how efficiently our membrane pores are filled (Fig. 3.6). During a typical experiment, we vacuum filter our Au NP solution through one side of the track-etched membrane and then flip the membrane over and vacuum filter Au NP solution through the membrane once again. To better understand particle loading, we first considered a membrane that had been loaded with Au NPs from only one side, which we will call the top of the membrane. We call the opposite side of the membrane the bottom of the membrane. Comparing the secondary (SE) and backscattered (BSE) SEM images of the top and bottom of the Au NP loaded membrane allows us to learn about how the nanoparticles get stuck within the membrane pores.

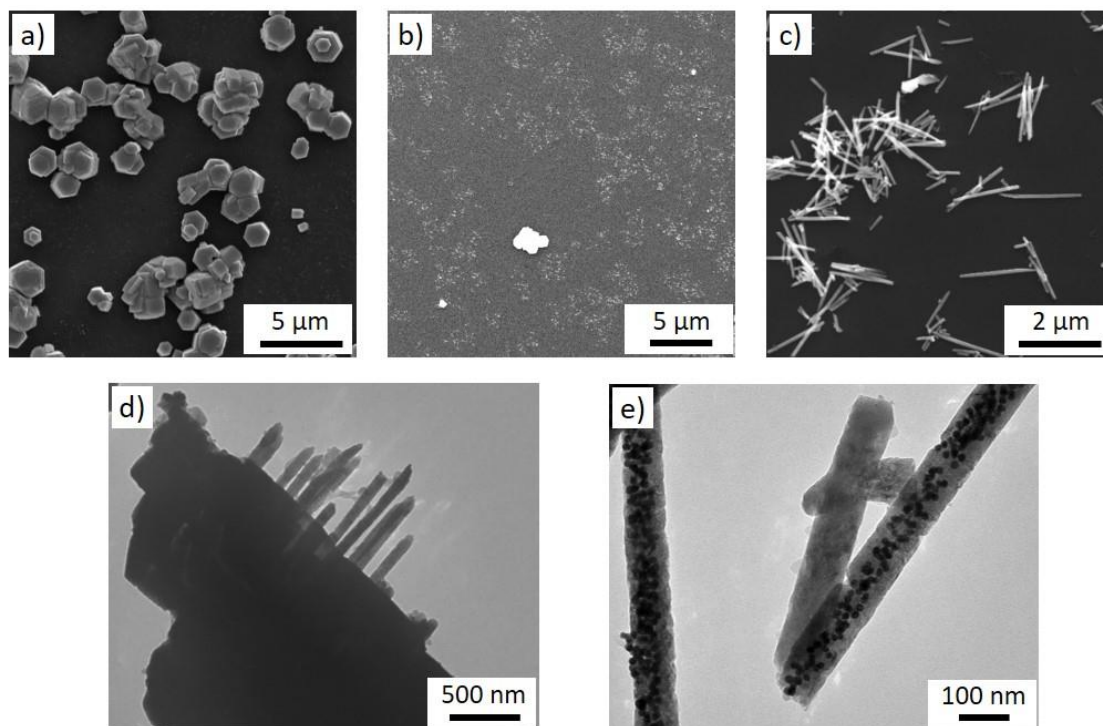


Figure 3.5. (a) SEM of an un-scraped membrane surface following ZnO growth shows hexagonally-faceted bulk ZnO crystals sitting on the membrane. (b) Backscattered electron imaging of the scraped membrane surface reveals patchy regions of light colored spots, similar to that of the scraped membrane post-Cu₂O growth. (c) SEM imaging of ZnO nanorods obtained after dissolving the scraped membrane. (d) TEM imaging of bulk ZnO crystals dissolved from an un-scraped membrane shows many nanorods extending from the bulk crystal. (e) TEM of two ZnO nanorods with entrapped Au nanoparticles. We also find one nanorod that does not contain nanoparticles and a broken piece of a rod.

SE imaging of the top of the loaded membrane show several unfilled membrane pores easily visible by the dark circular areas (Fig. 3.6a). There are also Au NPs covering nearly all of the membrane surface, which makes it challenging to identify membrane pores that are filled with nanoparticles. While secondary electron contrast arises due to changes in topography of the sample, backscattered electron contrast is sensitive to the atomic number, Z , of the sample. Additionally, the penetration depth of BSE is larger than that of SE, so we can probe Au nanoparticles embedded several μm deep within the membrane pores with BSE imaging.⁶³ Therefore, when we perform BSE imaging of the same region, the Au NP-filled membrane pores are easily identifiable by the dense white circular areas (Fig. 3.6b). SE imaging of the bottom of the loaded membrane shows no nanoparticles on the surface (Fig. 3.6c). However, with BSE imaging of this same region, it is possible to see some white circular spots indicating that we can still distinguish some of the filled membrane pores (Fig. 3,6d).

To gain further information about the loading of nanoparticles in the membrane pores, we can measure their distribution within nanorods following Cu_2O growth. After dissolving the membrane and imaging the $\text{Cu}_2\text{O}/\text{Au}$ NP nanorods in TEM, we can count the number of nanorods that contain or do not contain nanoparticles as a first approximation of our pore loading efficiency. We find that of 116 nanorods counted (from over 5 experiments), ~50% were found to contain nanoparticles (Table 3.1). This percentage, however, does not account for the fact that some of our nanorods probably fractured following growth during dissolution of the membrane. It is possible that some of the rods that we have counted as “empty”

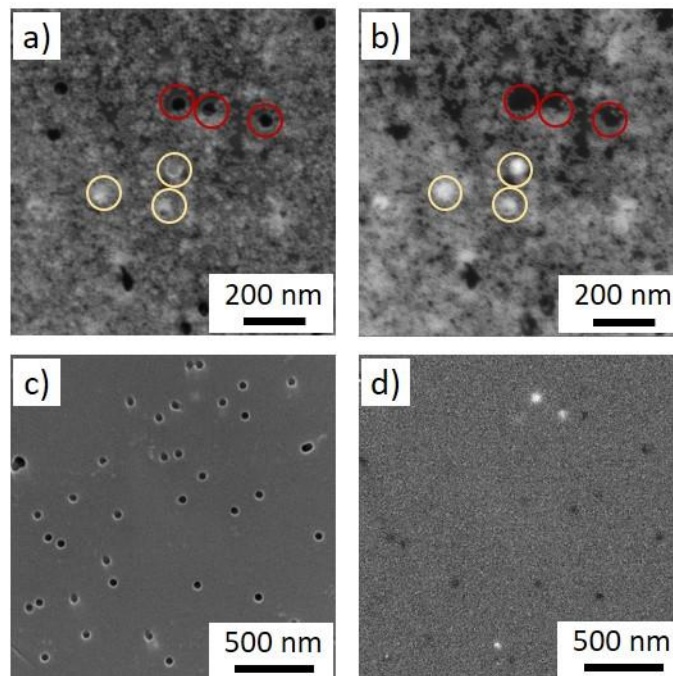


Figure 3.6. (a) Secondary electron (SE) imaging and (b) backscattered electron (BSE) imaging of the top side of a Au nanoparticle-loaded track-etched membrane. Though we see many Au nanoparticles covering the whole membrane surface, the SE image can help us identify unfilled pores (red circles) and the BSE image can help us identify filled membrane pores (yellow circles) by their extremely bright circular contrast. (c) SE imaging and (d) BSE imaging of the bottom side of the same Au nanoparticle-loaded membrane. While we see no surface coverage, we also only identify a few pores that we can detect as filled by their bright contrast in the BSE image.

perhaps were once part of a longer rod that did contain nanoparticles in a different section of the rod.

When counting nanorods that contain and do not contain particles, we also observe that sometimes particles appear to be isolated within one region of the nanorod while in other experiments the particles appear more dispersed throughout the nanorod (Fig. 3.7). The only difference in the experimental methods in these two scenarios is the length of time that the Au NP membrane is allowed to degas in the Cu₂O growth solution. A prolonged degas time (> 12 hours) seems to favor nanoparticles that are dispersed throughout a longer portion of the nanorod (Fig. 3.7b), while a short degas time (one hour) seems to favor “plugs” of nanoparticles within the membrane pores (Fig. 3.7a).

To quantify the differences between these two populations of nanorods, we measured the distances over which nanoparticles are spread along the length of the nanorod. Given that TEM images are a 2D projection of a 3D nanorod, we performed tilt series to develop a set of criteria to identify whether nanoparticles we were counting were in fact encapsulated within the nanorod and not attached to the nanorod surface (Fig. 3.8). In the experiments where nanoparticle-loaded membranes degassed for only one hour, of the 35 rods which contained particles, on average the particles were spread over 42 ± 21 % of the rod length. In the experiments where nanoparticle-loaded membranes degassed for more than 12 hours, of the 24 rods which contained particles, 83% of the rods contained nanoparticles spread over the whole length of the rod (Table 3.1). We might think that the difference in the length over which the nanoparticles spread along the length of the rod is explained by a difference in total

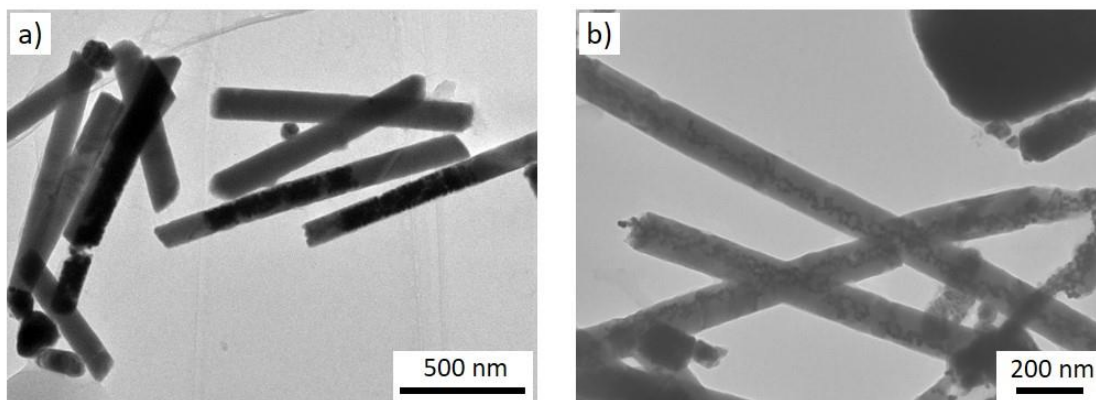


Figure 3.7. (a) TEM of $\text{Cu}_2\text{O}/\text{Au}$ NP composite rods grown where the nanoparticles are located within “plugs” that span only part of the total length of the rod. (b) TEM of $\text{Cu}_2\text{O}/\text{Au}$ NP composite rods where the nanoparticles are dispersed along the majority of the length of the rod.

rod length. The rods with more dispersed nanoparticles were shorter on average (759 ± 400 nm) than the rods that contained plugs of nanoparticles (1226 ± 575 nm). (This difference in average rod length can likely be attributed to differences in the washing away the membranes that caused more breakage and fragmenting of the nanorods with dispersed nanoparticles.) However, when we compare the length over which the nanoparticles are spread (not normalized to rod length), we see that when the loaded membrane degassed for more than 12 hours, the particles spread over 710 ± 420 nm compared to 471 ± 230 nm for loaded membranes that degassed for only one hour. These statistics allow us to conclude that degassing of the nanoparticle loaded membranes does lead to measurable change in the distribution of nanoparticles within the semiconducting rods.

3.3 Discussion

We first aimed to generalize our synthesis of semiconductor/plasmonic nanoparticle composite nanorods to other semiconductor materials by understanding the mechanism of nanorod formation in the track-etched membranes. In our experiments growing Cu_2O in membrane pores, we found bulk Cu_2O crystals with many attached nanorods (Fig. 3.2E,F). Using a similar method to grow ZnO in the membranes, we saw similar results (Fig. 3.5D). From these results, we hypothesized a growth mechanism where nanorods form by overgrowth off of bulk crystals and posit that any material that forms large, faceted crystals in solution could form nanorods by overgrowing into the membrane pores too. There is another possible growth mechanism where bulk crystals overgrow from the nanorods, which would also yield a final product of bulk crystals with nanorods attached. The central question is whether

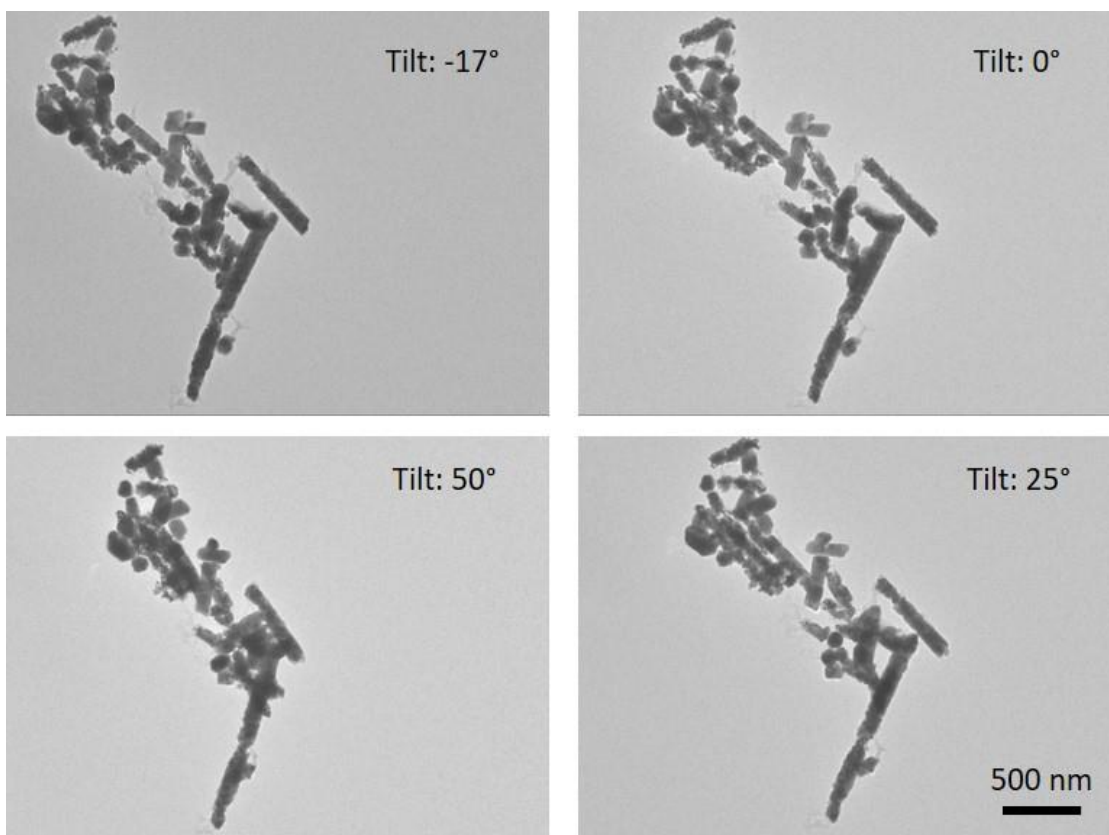


Figure 3.8. TEM imaging of Cu₂O/Au NP composite nanorods at four different α tilt angles. Because TEM imaging provides a 2D projection of a 3D object, this tilt series over nearly 70 ° shows that nanoparticles are largely fully encapsulated within the nanorods, and not simply attached to the outer surface of the nanorod.

Table 3.1. Summary of Cu₂O/Au NP composite rod incorporation statistics.

	Number of rods without NPs	Length of rods without NPs (nm)	Width of rods without NPs (nm)	Number of rods with NPs	Length of rods with NPs (nm)	Width of rods with NPs (nm)	Distance (along rod length) over which NPs are spread	Fraction of rod length over which NPs are spread	Percentage of rods with NPs spread along the whole length
Short degas	54	666 ± 309	116 ± 12	35	1226 ± 575	107 ± 14	471 ± 230	0.42 ± 0.21	5.7%
Long degas	3	418 ± 129	92 ± 12	24	759 ± 400	94 ± 10	710 ± 410	0.93 ± 0.19	83.3%

or not the crystals first nucleate within the membrane pores and grow out or whether the crystals first nucleate outside of the membrane pores and grow in. Put differently, there are two competing phenomena, the preferred nucleation at nanoscale pits/scratches on the surface and the challenge for crystallization precursors to effectively infiltrate and nucleate with the porous media.

Nucleation at grooves or scratches on a surface is well agreed to be faster than nucleation on an atomically smooth surface.⁶⁴⁻⁶⁶ Simulations of protein growth in a nanopore show that for the right size nanopore, nucleation can be seven orders of magnitude faster than nucleation on a flat surface.⁶⁷ For proteins, it seems that porosity can help promote nucleation and therefore nanorods may be more likely to nucleate independently within individual membrane pores.⁶⁸ Upon reaching the surface of the membrane, the nanorods are no longer restricted to grow in the cylindrical template of the membrane and begin to adopt a faceted equilibrium morphology. When the overgrowing bulk crystals originating from neighboring pores coalesce, they can form large single crystals even though they originated from different membrane pores. The result is bulk crystals with many attached nanorods, similar to what we saw in our experiments (Fig. 3.2E, F, Fig. 3.5D). This mechanism of bulk crystals overgrowing from nanorods was observed for lysozyme crystals grown in track-etched membrane pores.⁶⁹ In our experiments, however, the backscattered electron images of the scraped membrane surfaces can help us rule out the likelihood that bulk crystals form by overgrowth of nanorods. In that case, we would expect to see a random distribution of nanorods filling the membrane pores. However, we only see nanorods in patches or cluster with other nanorods, leading us to believe that they likely nucleated off a bulk

crystal that covered that region of the membrane surface. Time studies where we could observe earlier stages of crystal growth or even nucleation would further allow us to disprove this mechanism.

In the other possible nanorod growth mechanism, bulk crystals form first, either by forming in solution and falling to the membrane surface or by forming directly on the membrane surface (Fig. 3.3). Each of these bulk crystals covers an area of membrane pores and so when growth continues, the bulk crystal will continue to grow into those membrane pores and will form nanorods that are templated by the cylindrical membrane pores. It is plausible given what we know about the extra effort required to force other inorganic crystals to grow in nanoconfinement that bulk crystals are the first to form. For example, in many systems double-diffusion set ups or highly charged polymer additives were needed to encourage crystals to form within porous media.⁷⁰⁻⁷³ In our set-up, we have no additives and no restrictions on diffusion to promote nucleation in the pores of the track-etched membrane.

There is one other study of an additive-free, non-diffusion limited system, where potassium iodide crystals were grown in track-etched membrane pores. They too found that the KI rods formed by overgrowing off of bulk crystals.⁷⁴ In their experiment the KI rods were single crystalline and were much larger than our nanorods, so that there was obvious faceting of the rod growth front, which allowed them to identify which of the two primary bulk KI facets the rods nucleated from. We know from our previous studies of the Cu₂O composite nanorod formation that our nanorods often contain defects, which mean that each Cu₂O rod is often composed of a few crystallographic grains whose orientation are slightly rotated from one another.⁶¹

It is possible that by studying bulk crystals with Cu₂O or ZnO nanorods still attached we would be able to similarly identify if the nanorods have the same orientation as the bulk crystal facet from which they grow. By determining the crystallographic orientation of the multiple Cu₂O or ZnO nanorods in the region in proximity to the bulk crystal, we could say with greater certainty that the nanorods do in fact form by overgrowth off of bulk crystals.

With this understanding of the nanorod growth mechanism for Cu₂O and ZnO, we now hope to expand upon our method to grow other nanorod materials. To fully generalize our method, we also want to be able to entrap other types of nanoparticles within the nanorods. As we saw from studying nanoparticle loaded membranes, we filled only a fraction of the membrane pores with nanoparticles (Fig. 3.6A,B). To increase the fraction of membrane pores that get “clogged” with particles, which experimental parameters should we alter?

Studies of filtration explain that clogging of membranes often occurs by successive particle deposition as co-localized particles aggregate within a pore.^{75,76} When particular ratios of particle size to pore size are satisfied, regular packings of particles in the pores can be achieved.⁷⁷ Clogging or fouling of membrane pores occurs for a range of particle and pore ratios if flow rate and solution concentration are large enough then have a larger influence in whether or not particles clog the pores or not.⁷⁸ We know that our Au NP solution is dilute, with a concentration of 6.7 nM, (Fig. 3.9) and we have not yet explored how flow rate might help us improve the number of membranes pores that we can clog with Au NPs.

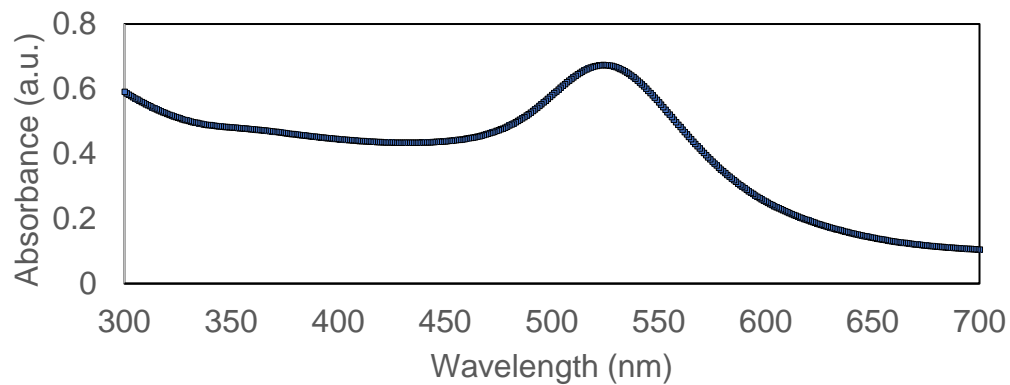


Figure 3.9. Absorption of Au NPs reveals its characteristic plasmonic resonance peak at 525nm. The broadness of the peak indicates some polydispersity. Using this absorption data, following the method for calculating Au NP concentration from UV/Vis measurement, we determine the concentration of Au NP in solution is ~6.7 nM.

In addition to flow rate and pressure, higher ionic strength solutions (100 mM) were able to modify the particle-particle and particle-pore wall intermolecular forces such that clogs were more likely to form.⁷⁹ Our Au NPs are citrate-stabilized and dialyzed into a slightly basic 0.1 mM NaOH solution to help prevent aggregation. We have not yet tried to increase the ionic strength of the Au NP solution prior to loading them into the membrane, but attractive interparticle interactions could help promote clogging.⁷⁶ Also notable, clogs that formed under high ionic strength solution conditions were more loosely packed, which could help explain to the dispersed nanoparticle formations we see after our nanoparticle loaded membranes are degassed for prolonged time periods in an electrolyte solution.⁷⁹

In addition, we would like to understand what controls the length over which particles are dispersed within our composite nanorods. One study found that the length of the microparticle clog was found to be of similar size to the pore width.⁸⁰ In our experiments, ultimately the gold nanoparticles form plugs that are many times longer than the pore width. (Table 3.1) In our case, we successively filter the Au nanoparticles through both sides of the membrane, and we know little about the initial clog formation, so we cannot rule out the possibility that the initial clogs that form are of similar length to the pore width.

We hypothesize that our Au NPs likely first clog in a “plug” structure (Fig. 7a) and then only reorganize and relax into a more dispersed configuration during the prolonged degas step (Fig. 8b). The degas step could mechanically disrupt the dense packing of the nanoparticles as solution is pulled through the membrane pores.⁸¹

Alternatively, the degas step takes place in a 0.068 M ionic strength solution, which will alter the particle-particle and particle-pore wall intermolecular forces and may stabilize a reorganized clog configuration. By varying both the ionic strength of the Au NP solution that we use while loading membranes as well as the ionic strength of the solution in which we degas the loaded membrane, we may gain a better understanding of how ionic strength affects the clog structure.

3.4 Conclusions

We present the first steps towards a generalizable method for the growth of nanorods with entrapped nanoparticle arrays. By studying the growth mechanism of Cu₂O nanorods in track-etched membrane pores, we learn that nanorods form within membrane pores by overgrowth off of bulk Cu₂O crystals. We showed that ZnO too can form nanorods within membrane pores and that we can also form ZnO/Au NP composite nanorods. To expand to other nanoparticle materials, we investigated the Au NP loading mechanism and found that we are able to tune the dispersion of nanoparticles within the nanorod by allowing the nanoparticle loaded membrane to degas in an electrolyte solution. Future work should determine how combining plasmonic nanoparticles and semiconductors in this heterostructure geometry can modify both the optical absorption as well as the energy transfer of the composites. In particular, the ability to create chains of dispersed plasmonic nanoparticles holds promise for further improvements to the optoelectronic properties due to increased broadband absorption.^{29,82}

REFERENCES

- (1) Atwater, H. A.; Polman, A. Plasmonics for Improved Photovoltaic Devices. *Nat. Mater.* **2010**, *9* (3), 205–213.
- (2) Cushing, S. K.; Wu, N. Plasmon-Enhanced Solar Energy Harvesting. *Electrochem. Soc. Interface* **2013**, *2* (c), 63–67.
- (3) Cushing, S. K.; Wu, N. Progress and Perspectives of Plasmon-Enhanced Solar Energy Conversion. *J. Phys. Chem. Lett.* **2016**, *7* (4), 666–675.
- (4) Kang, M.; Al-Heji, A. A.; Lee, J. E.; Saucer, T. W.; Jeon, S.; Wu, J. H.; Zhao, L.; Katzenstein, A. L.; Sofferan, D. L.; Sih, V.; et al. Ga Nanoparticle-Enhanced Photoluminescence of GaAs. *Appl. Phys. Lett.* **2013**, *103* (10).
- (5) Kang, M.; Jeon, S.; Jen, T.; Lee, J. E.; Sih, V.; Goldman, R. S. Formation of Embedded Plasmonic Ga Nanoparticle Arrays and Their Influence on GaAs Photoluminescence. *J. Appl. Phys.* **2017**, *122* (3).
- (6) Jiang, R.; Li, B.; Fang, C.; Wang, J. Metal/Semiconductor Hybrid Nanostructures for Plasmon-Enhanced Applications. *Adv. Mater.* **2014**, *26* (31), 5274–5309.
- (7) Kochuveedu, S. T.; Jang, Y. H.; Kim, D. H. A Study on the Mechanism for the Interaction of Light with Noble Metal-Metal Oxide Semiconductor Nanostructures for Various Photophysical Applications. *Chem. Soc. Rev.* **2013**, *42*, 8467–8493.
- (8) Wu, M.; Chen, W. J.; Shen, Y. H.; Huang, F. Z.; Li, C. H.; Li, S. K. In Situ Growth of Matchlike ZnO/Au Plasmonic Heterostructure for Enhanced Photoelectrochemical Water Splitting. *ACS Appl. Mater. Interfaces* **2014**, *6*

- (17), 15052–15060.
- (9) Pan, Y.; Deng, S.; Polavarapu, L.; Gao, N.; Yuan, P.; Sow, C. H.; Xu, Q.-H. Plasmon-Enhanced Photocatalytic Properties of Cu₂O Nanowire-Au Nanoparticle Assemblies. *Langmuir* **2012**, *28* (33), 12304–12310.
- (10) Wang, L.; Zhou, X.; Nguyen, N. T.; Schmuki, P. Plasmon-Enhanced Photoelectrochemical Water Splitting Using Au Nanoparticles Decorated on Hematite Nanoflake Arrays. *ChemSusChem* **2015**, *8* (4), 618–622.
- (11) Wang, H.; Chen, L.; Feng, Y.; Chen, H. Exploiting Core-Shell Synergy for Nanosynthesis and Mechanistic Investigation. *Acc. Chem. Res.* **2013**, *46* (7), 1636–1646.
- (12) Kuo, C.-H.; Hua, T.-E.; Huang, M. H. Au Nanocrystal-Directed Growth of Au-Cu₂O Core-Shell Heterostructures with Precise Morphological Control. *J. Am. Chem. Soc.* **2009**, *131* (49), 17871–17878.
- (13) Kuo, C. H.; Yang, Y. C.; Gwo, S.; Huang, M. H. Facet-Dependent and Au Nanocrystal-Enhanced Electrical and Photocatalytic Properties of Au-Cu₂O Core-Shell Heterostructures. *J. Am. Chem. Soc.* **2011**, *133* (4), 1052–1057.
- (14) Klug, M. T.; Dorval Courchesne, N. M.; Lee, Y. E.; Yun, D. S.; Qi, J.; Heldman, N. C.; Hammond, P. T.; Fang, N. X.; Belcher, A. M. Mediated Growth of Zinc Chalcogen Shells on Gold Nanoparticles by Free-Base Amino Acids. *Chem. Mater.* **2017**, *29* (16), 6993–7001.
- (15) Yang, K.-H.; Hsu, S.-C.; Huang, M. H. Facet-Dependent Optical and Photothermal Properties of Au@Ag-Cu₂O Core-Shell Nanocrystals. *Chem. Mater.* **2016**, *28* (14), 5140–5146.

- (16) Huang, L.; Zheng, J.; Huang, L.; Liu, J.; Ji, M.; Yao, Y.; Xu, M.; Liu, J.; Zhang, J.; Li, Y. Controlled Synthesis and Flexible Self-Assembly of Monodisperse Au@Semiconductor Core/Shell Hetero-Nanocrystals into Diverse Superstructures. *Chem. Mater.* **2017**, *29*, 2355–2363.
- (17) Zhang, L.; Blom, D. A.; Wang, H. Au-Cu₂O Core-Shell Nanoparticles: A Hybrid Metal-Semiconductor Heteronanostructure with Geometrically Tunable Optical Properties. *Chem. Mater.* **2011**, *23* (20), 4587–4598.
- (18) Li, J.; Cushing, S. K.; Bright, J.; Meng, F.; Senty, T. R.; Zheng, P.; Bristow, A. D.; Wu, N. Ag@Cu₂O Core-Shell Nanoparticles as Visible-Light Plasmonic Photocatalysts. *ACS Catal.* **2013**, *3* (1), 47–51.
- (19) Liu, D. Y.; Ding, S. Y.; Lin, H. X.; Liu, B. J.; Ye, Z. Z.; Fan, F. R.; Ren, B.; Tian, Z. Q. Distinctive Enhanced and Tunable Plasmon Resonant Absorption from Controllable Au@Cu₂O Nanoparticles: Experimental and Theoretical Modeling. *J. Phys. Chem. C* **2012**, *116* (7), 4477–4483.
- (20) Jing, H.; Large, N.; Zhang, Q.; Wang, H. Epitaxial Growth of Cu₂O on Ag Allows for Fine Control Over Particle Geometries and Optical Properties of Ag–Cu₂O Core–Shell Nanoparticles. *J. Phys. Chem. C* **2014**, *118* (34), 19948–19963.
- (21) Lu, B.; Liu, A.; Wu, H.; Shen, Q.; Zhao, T.; Wang, J. Hollow Au-Cu₂O Core-Shell Nanoparticles with Geometry-Dependent Optical Properties as Efficient Plasmonic Photocatalysts under Visible Light. *Langmuir* **2016**, *32* (12), 3085–3094.
- (22) Xiong, J.; Li, Z.; Chen, J.; Zhang, S.; Wang, L.; Dou, S. Facile Synthesis of

- Highly Efficient One-Dimensional Plasmonic Photocatalysts through Ag@Cu₂O Core-Shell Heteronanowires. *ACS Appl. Mater. Interfaces* **2014**, *6* (18), 15716–15725.
- (23) Jiang, D.; Zhou, W.; Zhong, X.; Zhang, Y.; Li, X. Distinguishing Localized Surface Plasmon Resonance and Schottky Junction of Au-Cu₂O Composites by Their Molecular Spacer Dependence. *ACS Appl. Mater. Interfaces* **2014**, *6* (14), 10958–10962.
- (24) Li, J.; Cushing, S. K.; Chu, D.; Zheng, P.; Bright, J.; Castle, C.; Manivannan, A.; Wu, N. Distinguishing Surface Effects of Gold Nanoparticles from Plasmonic Effect on Photoelectrochemical Water Splitting by Hematite. *J. Mater. Res.* **2016**, *31* (11), 1608–1615.
- (25) Lassiter, J. B.; Sobhani, H.; Fan, J. A.; Kundu, J.; Capasso, F.; Nordlander, P.; Halas, N. J. Fano Resonances in Plasmonic Nanoclusters: Geometrical and Chemical Tunability. *Nano Lett.* **2010**, *10* (8), 3184–3189.
- (26) Hentschel, M.; Dregely, D.; Vogelgesang, R.; Giessen, H.; Liu, N. Plasmonic Oligomers: The Role of Individual Particles in Collective Behavior. *ACS Nano* **2011**, *5* (3), 2042–2050.
- (27) Fan, J. A.; Wu, C.; Bao, K.; Bao, J.; Bardhan, R.; Halas, N. J.; Manoharan, V. N.; Nordlander, P.; Shvets, G.; Capasso, F. Self-Assembled Plasmonic Nanoparticle Clusters. *Science* **2010**, *328* (5982), 1135–1138.
- (28) Klinkova, A.; Choueiri, R. M.; Kumacheva, E. Self-Assembled Plasmonic Nanostructures. *Chem. Soc. Rev.* **2014**, *43*, 3976–3991.
- (29) Hanske, C.; Tebbe, M.; Kuttner, C.; Bieber, V.; Tsukruk, V. V.; Chanana, M.;

- König, T. A. F.; Fery, A. Strongly Coupled Plasmonic Modes on Macroscopic Areas via Template-Assisted Colloidal Self-Assembly. *Nano Lett.* **2014**, *14* (12), 6863–6871.
- (30) Luk'yanchuk, B.; Zheludev, N. I.; Maier, S. a; Halas, N. J.; Nordlander, P.; Giessen, H.; Chong, C. T. The Fano Resonance in Plasmonic Nanostructures and Metamaterials. *Nat. Mater.* **2010**, *9* (9), 707–715.
- (31) Hentschel, M.; Saliba, M.; Vogelgesang, R.; Giessen, H.; Alivisatos, A. P.; Liu, N. Transition from Isolated to Collective Modes in Plasmonic Oligomers. *Nano Lett.* **2010**, *10* (7), 2721–2726.
- (32) Kang, M.; Saucer, T. W.; Warren, M. V.; Wu, J. H.; Sun, H.; Sih, V.; Goldman, R. S. Surface Plasmon Resonances of Ga Nanoparticle Arrays. *Appl. Phys. Lett.* **2012**, *101* (8), 1–5.
- (33) Li, H.; Xin, H. L.; Kunitake, M. E.; Keene, E. C.; Muller, D. A.; Estroff, L. A. Calcite Prisms from Mollusk Shells (*Atrina Rigida*): Swiss-Cheese-like Organic-Inorganic Single-Crystal Composites. *Adv. Funct. Mater.* **2011**, *21* (11), 2028–2034.
- (34) Younis, S.; Kauffmann, Y.; Bloch, L.; Zolotoyabko, E. Inhomogeneity of Nacre Lamellae on the Nanometer Length Scale. *Cryst. Growth Des.* **2012**, *12* (9), 4574–4579.
- (35) Kunitake, M. E.; Mangano, L. M.; Peloquin, J. M.; Baker, S. P.; Estroff, L. A. Evaluation of Strengthening Mechanisms in Calcite Single Crystals from Mollusk Shells. *Acta Biomater.* **2013**, *9* (2), 5353–5359.
- (36) Weber, E.; Pokroy, B. Intracrystalline Inclusions within Single Crystalline

- Hosts: From Biomineralization to Bio-Inspired Crystal Growth. *CrystEngComm* **2015**, *17* (31), 5873–5883.
- (37) Polishchuk, I.; Bracha, A. A.; Bloch, L.; Levy, D.; Kozachkevich, S.; Etinger-Geller, Y.; Kauffmann, Y.; Burghammer, M.; Giacobbe, C.; Villanova, J.; et al. Coherently Aligned Nanoparticles within a Biogenic Single Crystal: A Biological Prestressing Strategy. *Science*. **2017**, *358* (6368), 1294–1298.
- (38) Khaimov-Mal'kov, V. Y. Growth of Crystals, Vol. 2. In *Growth of Crystals*, vol. 2; Shubnikov, A. V., Sheftal, N. N., Eds.; 1959.
- (39) Golovko, D. S.; Muñoz-Espí, R.; Wegner, G. Interaction between Poly (Styrene-Acrylic Acid) Latex Nanoparticles and Zinc Oxide Surfaces. *Langmuir* **2007**, *23* (7), 3566–3569.
- (40) Muñoz-Espí, R.; Jeschke, G.; Lieberwirth, I.; Gomez, C. M.; Wegner, G. ZnO-Latex Hybrids Obtained by Polymer-Controlled Crystallization: A Spectroscopic Investigation. *J. Phys. Chem. B* **2007**, *111* (4), 697–707.
- (41) Muñoz-Espí, R.; Qi, Y.; Lieberwirth, I.; Gómez, C. M.; Wegner, G. Surface-Functionalized Latex Particles as Controlling Agents for the Mineralization of Zinc Oxide in Aqueous Medium. *Chem. - A Eur. J.* **2006**, *12* (1), 118–129.
- (42) Lu, C.; Qi, L.; Cong, H.; Wang, X.; Yang, J.; Yang, L.; Zhang, D.; Ma, J.; Cao, W. Synthesis of Calcite Single Crystals with Porous Surface by Templating of Polymer Latex Particles. *Chem. Mater.* **2005**, *17* (20), 5218–5224.
- (43) Kim, Y. Y.; Ribeiro, L.; Maillot, F.; Ward, O.; Eichhorn, S. J.; Meldrum, F. C. Bio-Inspired Synthesis and Mechanical Properties of Calcite-Polymer Particle Composites. *Adv. Mater.* **2010**, *22* (18), 2082–2086.

- (44) Ning, Y.; Fielding, L. A.; Andrews, T. S.; Growney, D. J.; Armes, S. P. Sulfate-Based Anionic Diblock Copolymer Nanoparticles for Efficient Occlusion within Zinc Oxide. *Nanoscale* **2015**, *7* (15), 6691–6702.
- (45) Hanisch, A.; Yang, P.; Kulak, A. N.; Fielding, L. A.; Meldrum, F. C.; Armes, S. P. Phosphonic Acid-Functionalized Diblock Copolymer Nano-Objects via Polymerization-Induced Self-Assembly: Synthesis, Characterization, and Occlusion into Calcite Crystals. *Macromolecules* **2016**, *49* (1), 192–204.
- (46) Kulak, A. N.; Yang, P.; Kim, Y.-Y.; Armes, S. P.; Meldrum, F. C. Colouring Crystals with Inorganic Nanoparticles †. *Chem. Commun.* **2014**, *50*, 67–69.
- (47) Kim, Y.-Y.; Ganesan, K.; Yang, P.; Kulak, A.; Borukhin, S.; Pechook, S.; Ribeiro, L.; Kroger, R.; Eichhorn, S. An Artificial Biomineral Formed by Incorporation of Copolymer Micelles in Calcite Crystals. *Nat. Mater.* **2011**, *10* (11), 890–896.
- (48) Kim, Y. Y.; Semsarilar, M.; Carloni, J. D.; Cho, K. R.; Kulak, A. N.; Polishchuk, I.; Hendley, C. T.; Smeets, P. J. M.; Fielding, L. A.; Pokroy, B.; et al. Structure and Properties of Nanocomposites Formed by the Occlusion of Block Copolymer Worms and Vesicles Within Calcite Crystals. *Adv. Funct. Mater.* **2016**, *26* (9), 1382–1392.
- (49) Ning, Y.; Fielding, L. A.; Doncom, K. E. B.; Penfold, N. J. W.; Kulak, A. N.; Matsuoka, H.; Armes, S. P. Incorporating Diblock Copolymer Nanoparticles into Calcite Crystals: Do Anionic Carboxylate Groups Alone Ensure Efficient Occlusion? *ACS Macro Lett.* **2016**, *5* (3), 311–315.
- (50) Kim, Y.-Y.; Fielding, L. A.; Kulak, A. N.; Nahi, O.; Mercer, W.; Jones, E. R.;

- Armes, S. P.; Meldrum, F. C. Influence of the Structure of Block Copolymer Nanoparticles on the Growth of Calcium Carbonate. *Chem. Mater.* **2018**, *30* (20), 7091–7099.
- (51) Hendley IV, C. T.; Fielding, L. A.; Jones, E. R.; Ryan, A. J.; Armes, S. P.; Estroff, L. A. Mechanistic Insights into Diblock Copolymer Nanoparticle – Crystal Interactions Revealed via in Situ Atomic Force Microscopy. *J. Am. Chem. Soc.* **2018**, *140*, 7936–7945.
- (52) Ning, Y.; Fielding, L. A.; Ratcliffe, L. P. D.; Wang, Y. W.; Meldrum, F. C.; Armes, S. P. Occlusion of Sulfate-Based Diblock Copolymer Nanoparticles within Calcite: Effect of Varying the Surface Density of Anionic Stabilizer Chains. *J. Am. Chem. Soc.* **2016**, *138* (36), 11734–11742.
- (53) Kulak, A. N.; Grimes, R.; Kim, Y. Y.; Semsarilar, M.; Anduix-Canto, C.; Cespedes, O.; Armes, S. P.; Meldrum, F. C. Polymer-Directed Assembly of Single Crystal Zinc Oxide/Magnetite Nanocomposites under Atmospheric and Hydrothermal Conditions. *Chem. Mater.* **2016**, *28* (20), 7528–7536.
- (54) Cho, K. R.; Kim, Y.; Yang, P.; Cai, W.; Pan, H.; Kulak, A. N.; Lau, J. L.; Kulshreshtha, P.; Armes, S. P.; Meldrum, F. C.; et al. Direct Observation of Mineral-Organic Composite Formation Reveals Occlusion Mechanism. *Nat. Commun.* **2016**, *7*, 1–7.
- (55) Kulak, A. N.; Semsarilar, M.; Kim, Y.; Ihli, J.; Fielding, L. a; Cespedes, O.; Armes, S. P.; Meldrum, F. C. One-Pot Synthesis of an Inorganic Heterostructure: Uniform Occlusion of Magnetite Nanoparticles within Calcite Single Crystals. *Chem. Sci.* **2014**, 738–743.

- (56) Liu, Y.; Yuan, W.; Shi, Y.; Chen, X.; Wang, Y.; Chen, H.; Li, H. Functionalizing Single Crystals : Incorporation of Nanoparticles Inside Gel-Grown Calcite Crystals. *Angew. Chemie - Int. Ed.* **2014**, 4127–4131.
- (57) Kim, Y.-Y.; Schenk, A. S.; Walsh, D.; Kulak, A. N.; Cespedes, O.; Meldrum, F. C. Bio-Inspired Formation of Functional Calcite/Metal Oxide Nanoparticle Composites. *Nanoscale* **2014**, 6 (2), 852–859.
- (58) Liu, Y.; Zang, H.; Wang, L.; Fu, W.; Yuan, W.; Wu, J.; Jin, X.; Han, J.; Wu, C.; Wang, Y.; et al. Nanoparticles Incorporated inside Single-Crystals: Enhanced Fluorescent Properties. *Chem. Mater.* **2016**, 28.
- (59) Hetherington, N. B. J.; Kulak, A. N.; Kim, Y. Y.; Noel, E. H.; Snoswell, D.; Butler, M.; Meldrum, F. C. Porous Single Crystals of Calcite from Colloidal Crystal Templates: ACC Is Not Required for Nanoscale Templating. *Adv. Funct. Mater.* **2011**, 21 (5), 948–954.
- (60) Li, X.; Jiang, Y.; Shi, Z.; Xu, Z. Two Growth Modes of Metal Oxide in the Colloidal Crystal Template Leading to the Formation of Two Different Macroporous Materials. *Chem. Mater.* **2007**, 19 (22), 5424–5430.
- (61) Smith, A. E. A.-; Noble, J. M.; Hovden, R.; Uhl, A. M.; Dicorato, A.; Kim, Y.-Y.; Kulak, A. N.; Meldrum, F. C.; Lena, F. Physical Confinement Promoting Formation of Cu₂O–Au Heterostructures with Au Nanoparticles Entrapped within Crystalline Cu₂O Nanorods. *Chem. Mater.* **2016**, 29, 555–563.
- (62) Apel, P. Track Etching Technique in Membrane Technology. *Radiat. Meas.* **2001**, 34 (1–6), 559–566.
- (63) Demers, H.; Poirier-Demers, N.; Couture, A. R.; Joly, D.; Guilmain, M.; De

- Jonge, N.; Drouin, D. Three-Dimensional Electron Microscopy Simulation with the CASINO Monte Carlo Software. *Scanning* **2011**, *33* (3), 135–146.
- (64) Page, A. J.; Sear, R. P. Crystallization Controlled by the Geometry of a Surface. *J. Am. Chem. Soc.* **2009**, *131* (48), 17550–17551.
- (65) Campbell, J. M.; Meldrum, F. C.; Christenson, H. K. Observing the Formation of Ice and Organic Crystals in Active Sites. *Proc. Natl. Acad. Sci.* **2017**, *114* (5), 810–815.
- (66) Christenson, H. K. Two-Step Crystal Nucleation via Capillary Condensation. **2013**, 2030–2039.
- (67) Page, A. J.; Sear, R. P. Heterogeneous Nucleation in and out of Pores. *Phys. Rev. Lett.* **2006**, *97* (6), 1–4.
- (68) Nanev, C. N.; Saridakis, E.; Chayen, N. E. Protein Crystal Nucleation in Pores. *Sci. Rep.* **2017**, *7*, 35821.
- (69) Dobrev, D.; Baur, D.; Neumann, R. Crystallization of Lysozyme in Pores of Etched Heavy-Ion Tracks. *Appl. Phys. A Mater. Sci. Process.* **2005**, *80* (3), 451–456.
- (70) Cantaert, B.; Beniash, E.; Meldrum, F. C. The Role of Poly(Aspartic Acid) in the Precipitation of Calcium Phosphate in Confinement. *J. Mater. Chem. B* **2013**, *1* (48), 6586.
- (71) Schenk, A. S.; Albarracin, E. J.; Kim, Y.-Y.; Ihli, J.; Meldrum, F. C. Confinement Stabilises Single Crystal Vaterite Rods. *Chem. Commun.* **2014**, *50* (36), 4729–4732.
- (72) Zeng, M.; Kim, Y.-Y.; Anduix-Canto, C.; Frontera, C.; Laundry, D.; Kapur, N.;

- Christenson, H. K.; Meldrum, F. C. Confinement Generates Single-Crystal Aragonite Rods at Room Temperature. *Proc. Natl. Acad. Sci.* **2018**, 201718926.
- (73) Loste, E.; Park, R. J.; Warren, J.; Meldrum, F. C. Precipitation of Calcium Carbonate in Confinement. *Adv. Funct. Mater.* **2004**, *14* (12), 1211–1220.
- (74) Dobrev, D.; Vetter, J.; Neumann, R. Growth of Potassium Iodide Single-Crystals Using Ion Track Membranes as Templates. *Nucl. Instruments Methods Phys. Res. Sect. B Beam Interact. with Mater. Atoms* **1998**, *146* (1–4), 513–517.
- (75) Henry, C.; Minier, J. P.; Lefèvre, G. Towards a Description of Particulate Fouling: From Single Particle Deposition to Clogging. *Adv. Colloid Interface Sci.* **2012**, *185–186*, 34–76.
- (76) Dressaire, E.; Sauret, A. Clogging of Microfluidic Systems. *Soft Matter* **2017**, *13* (1), 37–48.
- (77) Xia, Y.; Yin, Y.; Lu, Y.; McLellan, J. Template-Assisted Self-Assembly of Spherical Colloids into Complex and Controllable Structures. *Adv. Funct. Mater.* **2003**, *13* (12), 907–918.
- (78) Wyss, H. M.; Blair, D. L.; Morris, J. F.; Stone, H. A.; Weitz, D. A. Mechanism for Clogging of Microchannels. *Phys. Rev. E - Stat. Nonlinear, Soft Matter Phys.* **2006**, *74* (6), 1–4.
- (79) Sendekie, Z. B.; Bacchin, P. Colloidal Jamming Dynamics in Microchannel Bottlenecks. *Langmuir* **2016**, *32* (6), 1478–1488.
- (80) Dersoir, B.; de Saint Vincent, M. R.; Abkarian, M.; Tabuteau, H. Clogging of a Single Pore by Colloidal Particles. *Microfluid. Nanofluidics* **2015**, *19* (4), 953–961.

- (81) Zuriguel, I.; Parisi, D. R.; Hidalgo, R. C.; Lozano, C.; Janda, A.; Gago, P. A.; Peralta, J. P.; Ferrer, L. M.; Pugnali, L. A.; Clément, E.; et al. Clogging Transition of Many-Particle Systems Flowing through Bottlenecks. *Sci. Rep.* **2014**, *4*, 1–8.
- (82) Zhou, L.; Zhuang, S.; He, C.; Tan, Y.; Wang, Z.; Zhu, J. Self-Assembled Spectrum Selective Plasmonic Absorbers with Tunable Bandwidth for Solar Energy Conversion. *Nano Energy* **2017**, *32*, 195–200.

CHAPTER 4

MOSAIC ANISOTROPY MODEL FOR MAGNETIC INTERACTIONS IN MESOSTRUCTURED CRYSTALS*

4.1 Abstract

We propose a new model for interpreting the magnetic interactions in crystals with mosaic texture called the mosaic anisotropy (MA) model. We test the MA model using hematite as a model system, comparing mosaic crystals to polycrystals, single crystal nanoparticles, and bulk single crystals. Vibrating sample magnetometry confirms the hypothesis of the MA model that mosaic crystals have larger remanence (M_r/M_s) and coercivity (H_c) compared to polycrystalline or bulk single crystals. By exploring the magnetic properties of mesostructured crystals, like the mosaic crystals of hematite studied here, we may be able to develop new routes to engineering harder magnetic materials.

4.2 Manuscript

Biom mineralization produces materials with hierarchical mesostructures that impart improved functionality compared to their non-biogenic counterparts.[1,2] Much research has focused on translating biomineral growth strategies into the laboratory to produce crystalline materials with complex architectures.[3–6] One common architecture in biominerals is that of mesostructured crystals, whose crystalline order falls between the perfect order of a single crystal and the random order of a polycrystal.[7] Numerous studies make the critical connection between

* Reproduced from Goldman, A.R., Asenath-Smith, E., Estroff, L.A., Mosaic anisotropy model for magnetic interactions in mesostructured crystals, *APL Mater.* **2017**, 104901. doi:10.1063/1.5007794., with the permission of AIP Publishing

control of the crystallographic texture and manipulation of the mechanical, catalytic or electronic properties.[8–13] Magnetic properties are also highly sensitive to nanostructure, and others have already demonstrated how a variety of hierarchically-structured crystals enable emergent (often enhanced) magnetic properties compared to their single crystal or polycrystalline counterparts.[14–20] Though many examples have reported mesostructured crystals made from magnetic materials, there has been limited characterization of their bulk magnetic properties and there is no general framework for understanding the long-range magnetic interactions in these nanocrystalline, mesostructured crystals.[21–23] In this work, we describe a generalized model for the magnetic interactions within one type of hierarchical architecture, mosaic crystals, in which the adjacent (coherent) crystalline domains are separated by small angle ($< 15^\circ$) grain boundaries. Using mosaic crystals of hematite ($\alpha\text{-Fe}_2\text{O}_3$), we test our prediction that small angle grain boundaries in mosaic crystals allow for enhanced remanence and magnetic hardness compared to single or polycrystals.

The magnetic interactions in nanocrystalline materials are governed by competition between the magnetocrystalline anisotropy, which prefers to align spins along a particular crystallographic direction (the easy axis), and the ferromagnetic exchange energy, which prefers to align spins parallel to neighboring spins. The random anisotropy (RA) model, though first developed to describe amorphous ferromagnets[24], addresses this competition and can be broadly applied to the magnetic interactions in nanocrystalline materials.[25,26] The random anisotropy model states that for a randomly-oriented, polycrystalline material with grain sizes (D)

much smaller than the ferromagnetic exchange length (L_{ex}), the magnetic moments across many grains will be forced to align in a mutually parallel direction (Fig. 4.1a, black dashed circle). This mutual alignment of spins within one exchange length minimizes the exchange energy at the cost of the magnetocrystalline anisotropy energy. Therefore, in a polycrystal, the effective magnetocrystalline anisotropy is reduced. A smaller effective anisotropy means the material is likely to demagnetize a greater amount once the magnetic field is removed (the remnant to saturation magnetization ratio, M_r/M_s , will be reduced) and it will require a smaller magnetic field to fully demagnetize the material (the coercivity, H_c , will be reduced), meaning the material will be a softer magnet. Here, we consider the magnetic interactions in a mosaic crystal and propose the mosaic anisotropy (MA) model to describe the magnetic properties of this class of materials. We test our new model using mosaic crystals of hematite.

In contrast to a polycrystalline material with randomly-oriented grains described in the RA model, a mosaic crystal can be thought of as a highly anisotropic, oriented grain structure with less than 15° of misorientation between neighboring grains.[27] Similar to the RA model, the MA model requires a magnetic material with a relatively high uniaxial magnetocrystalline anisotropy, such as hematite.[28] For a mosaic crystal, the exchange and magnetocrystalline anisotropy energy can be simultaneously minimized if the magnetic moments align along the well-oriented easy axes of the mosaic crystal (Fig. 4.1b). Based only upon the crystallographic alignment of the grains, we would expect the mosaic crystals to have a higher M_r/M_s than random polycrystals. Indeed, in bulk polycrystalline materials, increasing the

alignment of the easy axes of grains has been shown to increase the remnant to saturation magnetization ratio.[29–38] In most of these examples, increased alignment leads to more exchange coupling between the grains. Then, once one grain reverses its magnetization direction, all of the neighboring grains will also reverse their magnetization, leading to a lower H_c than for random polycrystals. However, in a few studies, where secondary phases were present at the grain boundaries to impede the exchange coupling, there was a concurrent enhancement of M_r/M_s and H_c . [29,33] The extent to which the grains are magnetically exchange coupled is determined by grain size, grain alignment, and inter-grain spacing, each of which will affect the coercivity of the material.[35–45] Therefore, depending on the nature of the exchange coupling between the crystallites in mosaic crystals, we can predict the effect on the coercivity. If the grains of the mosaic crystal perfectly exchange couple to each other, then similar to the other examples of textured polycrystalline ferromagnets, we would expect to observe a low H_c , close to that of a single crystal. However, mosaic crystals contain large concentrations of individual dislocations at the grain boundaries between crystallites (Fig. 4.1b, yellow). If there is enough crystallographic misorientation at the grain boundaries to disrupt the exchange coupling between grains, preventing the avalanche of magnetization reversal by pinning domain wall propagation, then we would expect to observe an increase in H_c compared to single crystals or polycrystals. However, if there is too much misorientation at the grain boundaries, then the barrier to nucleate a reverse domain will be lowered, and we would expect to see less of an increase in H_c than for the more oriented grains. To test these hypotheses, we must examine a series of samples with textures spanning random polycrystals, mosaic

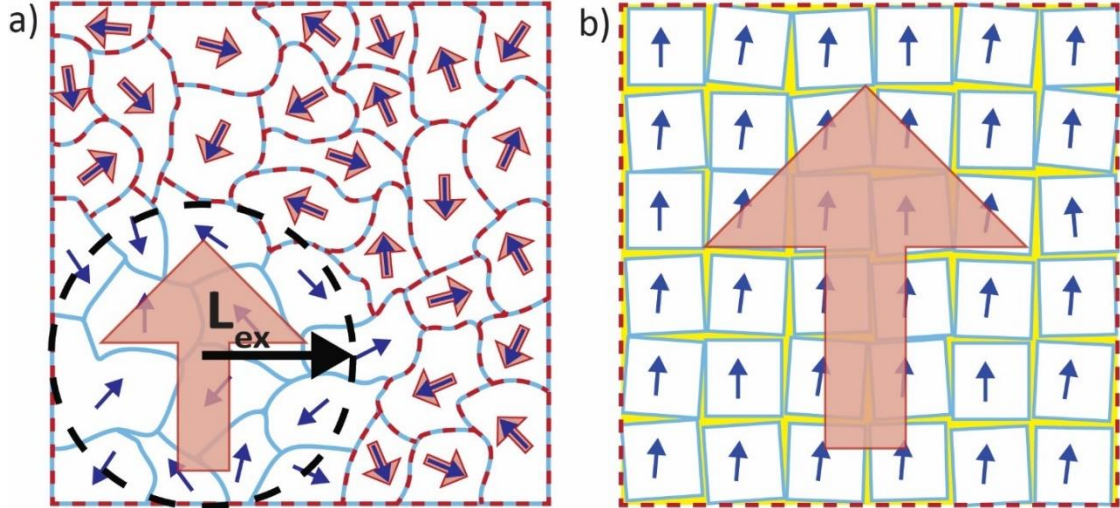


Figure 4.1 Schematic of the alignment of magnetic moments (a) in a polycrystalline material as described by the random anisotropy (RA) model and (b) in a mosaic crystal as described by the mosaic anisotropy (MA) model proposed in this paper. For the RA model, we discuss only the case where the grain size (D) is smaller than the ferromagnetic exchange length (L_{ex}), the length within which neighboring spins must align parallel. A circle with radius L_{ex} is shown in black. Crystalline grain boundaries are shown in blue solid lines and the high magnetocrystalline anisotropy axis is shown in blue arrows. Magnetic domain boundaries are shown in red dashed lines and the direction of the magnetic moment is shown in red arrows. For clarity, each arrow depicts only one high anisotropy/spin direction, though the antiparallel direction is energetically degenerate. (a) For the polycrystalline material, the high anisotropy axes of the crystalline grains are randomly oriented, and in the region outside the black dashed circle, the magnetic moments (red) always follow the high anisotropy axes (blue). Magnetic moments within one exchange length (within the black dashed circle) must align parallel to one another (large red arrow), though the magnetic moments now do not align with the high anisotropy axes. (b) For the mosaic crystal, the crystalline grains, and thus the high anisotropy axes, are highly oriented, with small angle grain boundaries (shown in yellow) between neighboring grains. Therefore, magnetic moments can align parallel to one another, while simultaneously aligning with the high anisotropy axes.

crystals, and single crystals.

Hematite makes an excellent model system, both because it is a well-studied magnetic material and because mosaic crystals of hematite have already been prepared synthetically and thoroughly characterized.[46–49] The two key features of the magnetic properties of bulk hematite are its canted antiferromagnetic order at room temperature and its spin-flop transition to collinear antiferromagnetism (AFM), called the Morin transition, at ~260 K.[50] The canted antiferromagnetic order at room temperature endows hematite with a large pseudo-uniaxial magnetocrystalline anisotropy.[28] Additionally, due to the canting, the net ferromagnetic moment in hematite is tiny ($\sim 0.01 \mu_B/\text{Fe}^{3+}$), meaning there is little driving force to break into domains and L_{ex} is $\sim 10\text{-}100 \mu\text{m}$.[51,52] This huge ferromagnetic exchange length means that only large-grained polycrystalline hematite will not experience reduced effective anisotropy as described by the random anisotropy model.

The mosaic crystals studied here form pseudo-cubes ranging in size from 2-4 μm , and are synthesized following procedures adapted from Matijevic, et al. (Fig 4.2a,b).[46,53,54] Investigation into the internal structure of the mosaic crystals by our group revealed that the pseudo-cubes are composed of nanoscale crystalline subunits that are separated by low angle grain boundaries and are thus highly oriented with respect to one another, such that there is a single orientation of the hematite lattice across each pseudo-cube.[46] The mosaic spread (the angular range of the low-angle grain boundaries) for these mosaic crystals ranged from 0-12.8° depending on the crystallographic direction. Additionally, we reported that the mosaic crystals of hematite have an average crystallite size of $\sim 25\text{-}45 \text{ nm}$, determined by Scherrer

analysis, which disregards the contributions of strain and therefore may over/underestimate the crystallite size by up to 50%. [46,55] Regardless of the large error in the estimate of the crystallite size, the grain size (D) in the mosaic crystals (25-45 nm) is orders of magnitude smaller than L_{ex} of hematite (10-100 μm). [51] This knowledge of the internal crystalline structure of the mosaic crystals allows us to use this model system to expand the understanding of textured magnetic materials into mesostructured crystals, where the grain sizes are often orders of magnitude smaller.

To test the prediction of the MA model that mosaic crystals will have enhanced magnetic hardness compared to polycrystals and bulk single crystals, we enlist a series of control samples with increasing amounts of orientation between crystallites, from single crystal nanoparticles to polycrystals to mosaic crystals to bulk single crystals. Bulk single crystals present a highly-oriented crystalline structure, which contains no grain boundaries and few crystallographic defects compared to the mosaic crystal. However, most large single crystal hematite is geologic in origin and contains many atomic impurities, complicating its use as a control sample. The study by Flanders, et al. on the magnetic properties of single crystals of synthetic, flux-grown hematite is used in place of our own single crystal control sample. [56] The polycrystalline hematite, which was purchased from Fisher Scientific, is composed of polydisperse, irregularly-shaped particles (Fig. 4.2c). The polycrystalline nanoparticles serve as the control sample with a randomly-oriented grain structure (Fig. 4.1a) to contrast the highly anisotropic, well-oriented grain structure of the mosaic crystals (Fig. 4.1b). The single crystal nanoparticles, which are synthesized following procedures adapted from Raming, et al. (see Supplementary Methods), form faceted, rhombohedral-shaped

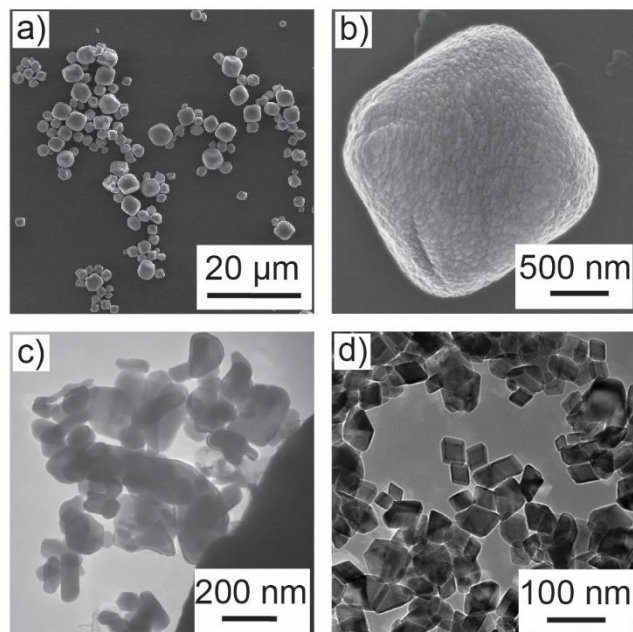


Figure 4.2. (a) SEM of mosaic crystals of hematite shows pseudo-cubes with edge lengths ranging from 2-4 μm . (b) The rough surface of the pseudocubes, seen to be composed of anisotropic nanoparticles, reveals their mosaic internal structure. In order to better visualize the surface texture, contrast limited adaptive histogram equalization (CLAHE) in ImageJ was applied here.[58] The original image can be found in Fig. 4.S1. (c) TEM of hematite purchased from Fisher Scientific shows irregular shaped particles, many of which are polycrystalline, ranging in size from 50 nm to >100 nm. (d) TEM of hematite nanoparticles shows that each nanoparticle is a faceted, 25-50 nm, rhombohedral, single crystal.

crystals (Fig. 4.2d).[57] The control sample of isolated single crystal nanoparticles help confirm that the crystallites in the mosaic crystal do not behave like independent non-interacting crystallites. In this set of four samples, we tested the hypotheses of the MA model and provide a more complete description of the magnetic properties of mosaic crystals.

To determine the magnetic hardness of each sample, isothermal field-dependent magnetization measurements were performed using a vibrating sample magnetometer (VSM) (see Supplementary Methods). The mosaic crystal hematite has an open hysteresis loop at 300 K that becomes a wider loop at 15 K (Fig. 4.3a), while the polycrystalline hematite has an open hysteresis loop at 300 K that transitions to a closed line at 15 K (Fig. 4.3b). Finally, the single crystal nanoparticle hematite has a tiny open hysteresis loop at 300 K that remains open at 15 K (Fig. 4.3c).

From the field-dependent magnetization, we can extract the coercivity (H_c), remnant to saturation magnetization ratio (M_r/M_s) and antiferromagnetic susceptibility (χ_{AFM}) from the 300 K data (Fig. 4.S2). The field-dependent magnetization for hematite is a superposition of a ferromagnetic (FM) hysteresis loop and a sloped antiferromagnetic (AFM) background whose slope is χ_{AFM} . Because the χ_{AFM} is an intrinsic material property determined by the crystal structure, we can use it as a measure of whether the mosaic crystals of hematite behave according to the canted antiferromagnetic order of hematite, or if uncompensated spins at the grain boundaries, instead, dominate the magnetic behavior. χ_{AFM} is assumed to be linear with magnetic field at 300 K and thus can be easily calculated by fitting the slope of the field-dependent magnetization data in the high field (40-50 kOe) region

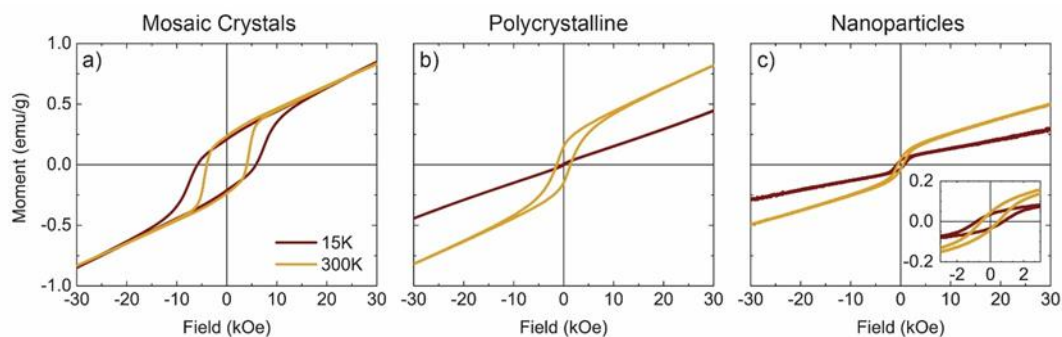


Figure 4.3. Field-dependent magnetization is measured at two temperatures 300 K (yellow) and 15 K (red) for (a) the mosaic crystals shown in Fig. 4.2 a,b, (b) the polycrystalline hematite shown in Fig. 4.2c, and (c) the single crystal nanoparticles shown in Fig. 4.2d, with the inset showing a small open hysteresis loop.

The hysteresis loops at 300 K show a drastic difference in coercivity between the three samples (Fig. 4.3, yellow, Table 4.1). The mosaic crystal has a coercivity of 4.40 kOe, which is more than twice as large as that of polycrystalline hematite (1.70 kOe) and orders of magnitude larger than that of the single crystal nanoparticles (0.6 kOe) and bulk single crystal (0.006 kOe) (Table 4.1).

(Fig. 4.S2).[56]

We find that χ_{AFM} for both the polycrystalline and mosaic crystal hematite is close to that of bulk hematite (Fig. 4.S2, Table 4.S1). However, the single crystal nanoparticles have drastically different χ_{AFM} suggesting that the nanoparticles do not behave like bulk hematite, but rather behave magnetically like surface spins (Table 4.S1). This result is critical to validating the applicability of the MA model to our mosaic crystals of hematite because the MA model describes only the interactions of spins in the crystallites and not the “free” surface spins.

Other studies on pseudocubes or mesocrystals of hematite that appear similar in shape and surface morphology to our mosaic crystals report similarly large coercivity values.[59,60] However, none of these reports provide an explanation for the size of H_c based on a detailed understanding of the internal grain structure. Assuming the samples studied in these previous reports were also mosaic crystals, the MA model can also be used to explain their results.

We also observe differences in the shape of the FM loops across the samples. The 300 K hysteresis loop for the mosaic crystal of hematite (Fig. 4.3a, yellow) is squarer than that of the polycrystalline or single crystal nanoparticle hematite (Fig. 4.3b,c). The squareness can be quantified by the remnant to saturation magnetization ratio (M_r/M_s). In order to compare M_r/M_s values across samples, the antiferromagnetic susceptibility was subtracted (Fig. 4.S2). In order of increasing squareness, the M_r/M_s for the single crystal nanoparticles is 0.22, for the polycrystal is 0.54, for the bulk single crystal is 0.63, and for the mosaic crystal is 0.86 (Table 4.1). It has been shown that the portion of the hysteresis loop between M_s and M_r is especially dependent on

Table 4.1. Magnetic data for the four hematite samples.

Increasing		M_r/M_s^*	H_c (kOe)*	T_m (K)†	ΔT_m (K) †	$\Delta M/M_{300K}^\dagger$
Amount of Orientation	Single Crystal	0.22	0.6	247 [◊]	15 [◊]	38 % [◊]
	Nanoparticle					
Between Crystallites	Polycrystalline	0.54	1.70	265	12	87 %
↓	Mosaic	0.86	4.40	181	125	14 %
	Crystal					
	Bulk Single Crystal [§]	0.63	0.006	262.3	2.3	Not reported

[§]Data for the bulk single crystal is from Ref. [56]. * See Fig. 4.S2 for explanation of how M_r/M_s and H_c (Oe) are extracted from the 300 K field-dependent magnetization measurements. † See Fig. 4.S3 for explanation of how T_m (K), ΔT_m (K), and $\Delta M/M_{300K}$ are extracted from the ZFC temperature-dependent magnetization measurements. [◊]Value from single measurement, otherwise the value is the average of three measurements.

crystalline texture of the material.[61] The small (less than 0.5) M_r/M_s in the nanoparticles confirms that broken bonds and structural disorder dominate the magnetic behavior of the nanoparticles. The M_r/M_s for the polycrystals is close to the expected 0.5 for a randomly-oriented collection of hard, non-interacting crystallites.[62] The reduced M_r/M_s for the polycrystals compared to the mosaic crystals indicates that indeed some of the anisotropy has been lost as predicted by the random anisotropy model. The M_r/M_s of pure bulk single crystals is likely lower than that of the mosaic crystals because the bulk single crystals are multi-domain magnets.[56] Though reports of the single domain/multi-domain cut-off size in hematite vary from 15 μm to $> 100 \mu\text{m}$, the size of the mosaic crystals falls safely below this limit, while the synthetic bulk single crystals of Flanders, et al. (though not reported) likely falls above this limit.[56,63–65] The M_r/M_s of multi-domain magnets is generally lower than that of single domain magnets due to the lower energetic cost of magnetization reversal in a material that already contains domain walls. The large M_r/M_s for the mosaic crystals is consistent with the remanence enhancement predicted for highly aligned grain structures. [29–32,34–38]

From the 300 K field-dependent magnetization behavior alone, we can conclude that as predicted by the MA model, the mosaic crystals of hematite are harder magnets than polycrystalline or single crystal hematite (Fig. 4.3, yellow). The high degree of alignment between neighboring crystallites in the mosaic crystal allows for the magnetic moments to align with the high magnetocrystalline anisotropy axis, while still aligning with one another. Therefore, the mosaic crystal is able to retain its large effective anisotropy, which can be seen in the large M_r/M_s , which is higher for the mosaic crystals

than for all of the other control samples (Table 4.1). If alignment of crystalline grains was the only concern, then the mosaic crystal should perform similarly to the bulk single crystal, but the mosaic crystal has a coercive field that is $\sim 10^3$ times larger than that of the bulk single crystal. Because of the large H_c compared to the bulk single crystal and random polycrystal, we can conclude that there is a disruption of the exchange coupling between the grains. Additionally, because the magnetization reversal does not seem to occur as an avalanche (Fig. 4.3a), we can conclude that the grain boundaries must pin domain wall propagation during magnetization reversal. It is possible that a mosaic crystal with less misorientation between the crystallites could further increase H_c because the large misorientation in these hematite mosaic crystals (up to 12.8°) may provide lower energetic barriers to nucleate reverse domains. The framework presented here lays the groundwork for further modeling to explore the quantitative dependence of misorientation angle on magnetization reversal in textured materials.[35–38] Future studies should grow mesostructured crystals with different degrees of misorientation in order to test the competition between the propagation and nucleation of reverse domains. Not only are mosaic crystals a unique platform to explore the magnetic interactions in materials with high degrees of alignment, but the nanometric grain sizes allow us to explore different regimes of exchange coupling effects than in textured, bulk ferromagnets.

The 15 K field-dependent magnetization reveals further differences between the mosaic crystals and the polycrystalline and single crystal nanoparticle reference materials (Fig. 4.3, red). By 15 K, the polycrystalline hematite exhibits collinear antiferromagnetic order, expected for hematite that has undergone the Morin transition

(Fig 4.3b, red). The mosaic crystal not only retains its open hysteresis loop down to 15 K, but the coercive field is larger at 15 K than at 300 K (Fig. 4.3a, red). The single crystal nanoparticles retain a small open hysteresis loop, though the AFM susceptibility decreased from 300 K to 15 K, together continuing to indicate they behave like isolated nanoparticles with uncompensated surface spins (Fig. 4.3c, red).

Temperature-dependent, zero-field cooled/field cooled (ZFC/FC), magnetization measurements were performed to study the Morin transition of the hematite samples (Fig. 4.4). The Morin transition temperature (T_m), sharpness of the transition (ΔT_m), and the percent decrease in magnetization from 300 K to 15 K ($\Delta M/M_{300K}$) are extracted from the ZFC temperature-dependent magnetization measurements for all three samples (Table 4.1, Fig. 4.S3). These measurements confirm the well-defined Morin transition in the polycrystalline hematite (Fig. 4.4b), which occurs at the expected ~ 260 K for bulk hematite, and the lack of a Morin transition in the mosaic crystal hematite, which shows almost no decrease in magnetization from 300 K to 15 K (Fig. 4.4a). The polycrystalline hematite loses 87% of its initial magnetization after going through the Morin transition, while the mosaic crystals lose only 14% of their initial magnetization (Table 4.1). A partial Morin transition occurs in the single crystal nanoparticles (Fig. 4.4c), which reduce their initial magnetization by 38%. Additionally, the range of temperatures over which the Morin transition occurs (ΔT_m) is much larger for the mosaic crystals than for the polycrystals, single crystal nanoparticles or bulk single crystal (Table 4.1).

The Morin transition arises due to the differing temperature dependencies of the single ion (also called fine structure) anisotropy and dipolar anisotropy.[66] The Morin

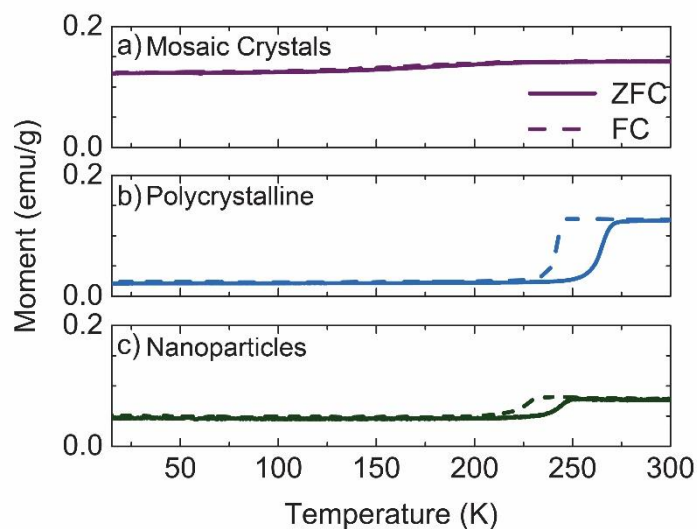


Figure 4.4. Temperature-dependent, zero-field cooled/field cooled (ZFC/FC), magnetization measurements collected with an applied field of 1 kOe. (a) Mosaic crystal hematite shows only a gradual and broad decrease in magnetization across the whole temperature range. (b) Polycrystalline hematite exhibits a sharp Morin transition centered near 260 K, the transition temperature for bulk hematite. (c) Single crystal nanoparticle hematite shows a partial Morin transition slightly below the expected T_m .

transition has been shown to be sensitive to strain[67,68], size[18,69–73], non-magnetic impurities[56,74], shape[75,76] and inter-particle interactions[77,78], each of which has been shown to depress T_m to lower temperatures or eliminate it entirely. It should be noted that the mosaic crystals have 32.5 ppm atomic Si impurities due to their growth in a borosilicate glass vessel.[54] However, Flanders, et al. found that 1 wt% (10,000 ppm) Si impurity in bulk single crystals of hematite did not shift the Morin transition temperature from its bulk value.[56] As a result, we believe that the absence of a Morin transition in the mosaic crystals of hematite is neither due to non-magnetic impurities, nor to size given that the mosaic crystals (Fig. 4.3a, 4.4a) behave distinctly from the collection of isolated hematite nanoparticles (Fig. 4.3c, 4.4c). The Si impurities, however, do impact the hematite lattice and there is an anisotropic expansion of the c axis by 0.19%.[54] Using the empirical relationships that relate the Morin transition temperature, particle diameter and strain, the mosaic crystals would need between 0.1-0.29% strain in order to depress T_m to 181 K, which is in the ballpark of the lattice strain for the hematite mosaic crystals.[67,76] Thus, it is likely that the Morin transition is suppressed in the mosaic crystals due to strain.

In summary, we developed the mosaic anisotropy model to predict that mosaic crystals will have a larger remanence and be harder magnetic materials than polycrystals or single crystals. The MA model hypothesizes that the crystallographic alignment of grains and the small angle grain boundaries between them, both contribute to the higher H_c and larger M_r/M_s ratio. We tested these predictions using mosaic crystals of hematite and showed that their coercivity and M_r/M_s ratio are significantly higher than those of polycrystals, single crystal nanoparticles and bulk

single crystals. Hematite served as an excellent model system for this study, though our model can generally describe the magnetic interactions in other hierarchically-structured materials whose crystalline order falls between that of single crystals and polycrystals.[9,21] By continuing to explore the magnetic properties of mesostructured crystalline architectures, particularly those with small angle grain boundaries, we may be able to develop new routes to engineering harder magnetic materials without relying on scarce rare earth magnets.

4.3 Acknowledgements

We acknowledge support from the NSF (DMR-1210304) and A.R.G. acknowledges the NSF Graduate Research Fellowship Program (GRF, DGE-1144153). This work made use of the Cornell Center for Materials Research Shared Facilities which are supported through the NSF MRSEC program (DMR-1120296). We would like to thank Professors Bruce van Dover and Gregory Fuchs for many helpful discussions and insights on this work.

4.4 Supplementary Methods

4.4.1 Materials

All materials were used without further purification.

Ferric oxide powder, Lot #: 997109 (Fisher Scientific).

Iron(III) chloride hexahydrate, $\geq 99\%$ (Sigma-Aldrich)

Hydrochloric acid, 36.5–38%; Certified ACS Plus Reagent (Fisher Scientific)

4.4.2 Synthesis

Mosaic crystals of hematite were synthesized following methods described in Asenath-Smith and Estroff.^{46,54}

Single crystal hematite nanoparticles were synthesized using adapted procedures from Raming, et al.⁵⁷ Briefly, a 250 mL Pyrex media bottle containing 250 mL of 1 mM HCl solution was heated while stirring to 98 °C. Then, 0.1351 g FeCl₃•6H₂O powder (for a final concentration of 2 mM FeCl₃ in the 250 mL solution) was added to the heated HCl solution. A pipette was used to rinse all of the FeCl₃ powder out of the weigh boat using the heated 1 mM HCl. The bright orange, transparent solution stirred for 5 minutes before a lid was placed on the Pyrex bottle and it was moved into a pre-heated 100 °C furnace for 6 days. Upon removal from the furnace and cooling, the reddish-orange solution now containing α -Fe₂O₃ nanoparticles remained transparent. The nanoparticles were rinsed by dialysis (MWCO = 3.5K) with deionized water with four exchanges over the course of 48 hours. The nanoparticle solution was transferred into 50 mL centrifuge tubes and placed into the freezer to force the particles to settle out of solution. After defrosting, the nanoparticle solutions were centrifuged (3600 g, 5 min) and supernatant disposed of. The red-orange nanoparticle powder was lyophilized to dryness.

4.4.3 Magnetic Characterization

Vibrating Sample Magnetometry measurements were performed on a Quantum Design Physical Properties Measurement System (PPMS). Powder samples (< 10 mg) were weighed to 0.00001 g precision and loaded into a polypropylene powder sample holder. All measurements of magnetization are normalized to the mass of powder. Each set of ZFC/FC and field-dependent measurements was performed on a fresh sample. First, zero-field cooled/field cooled (ZFC/FC) measurements were performed by first cooling the sample to 15 K in zero field to lock in the magnetization state.

Then a 1 kOe field was applied and the sample magnetization was recorded as a function of temperature upon warming to 300 K and upon cooling to 15 K. Following the ZFC/FC measurements, isothermal, field-dependent measurements were performed at 15 K and 300 K with a ramp rate of 100 Oe/second to ± 70 kOe.

4.4.4 Structural and Phase Characterization

Carbon-coated mosaic crystals of hematite were imaged using using a Mira3 LM field emission scanning electron microscopy (SEM) at 10 keV.

Fisher Scientific Fe₂O₃ particles and our own nanoparticles were imaged under bright-field conditions in a Tecnai T12 transmission electron microscope (TEM) equipped with a LaB₆ filament operating at 120 kV.

Phase analysis was performed via powder x-ray diffraction (XRD) using a Bruker D8 Advance ECO powder diffractometer with Cu K α radiation, operating at 40 kV and 25 mA with scan rates of 1-3°/minute. Phase purity of all three hematite samples and crystallite size determinations of the two nanoparticle samples are shown in Fig. 4.S4 and Table 4.S2.

4.5 Supporting Information

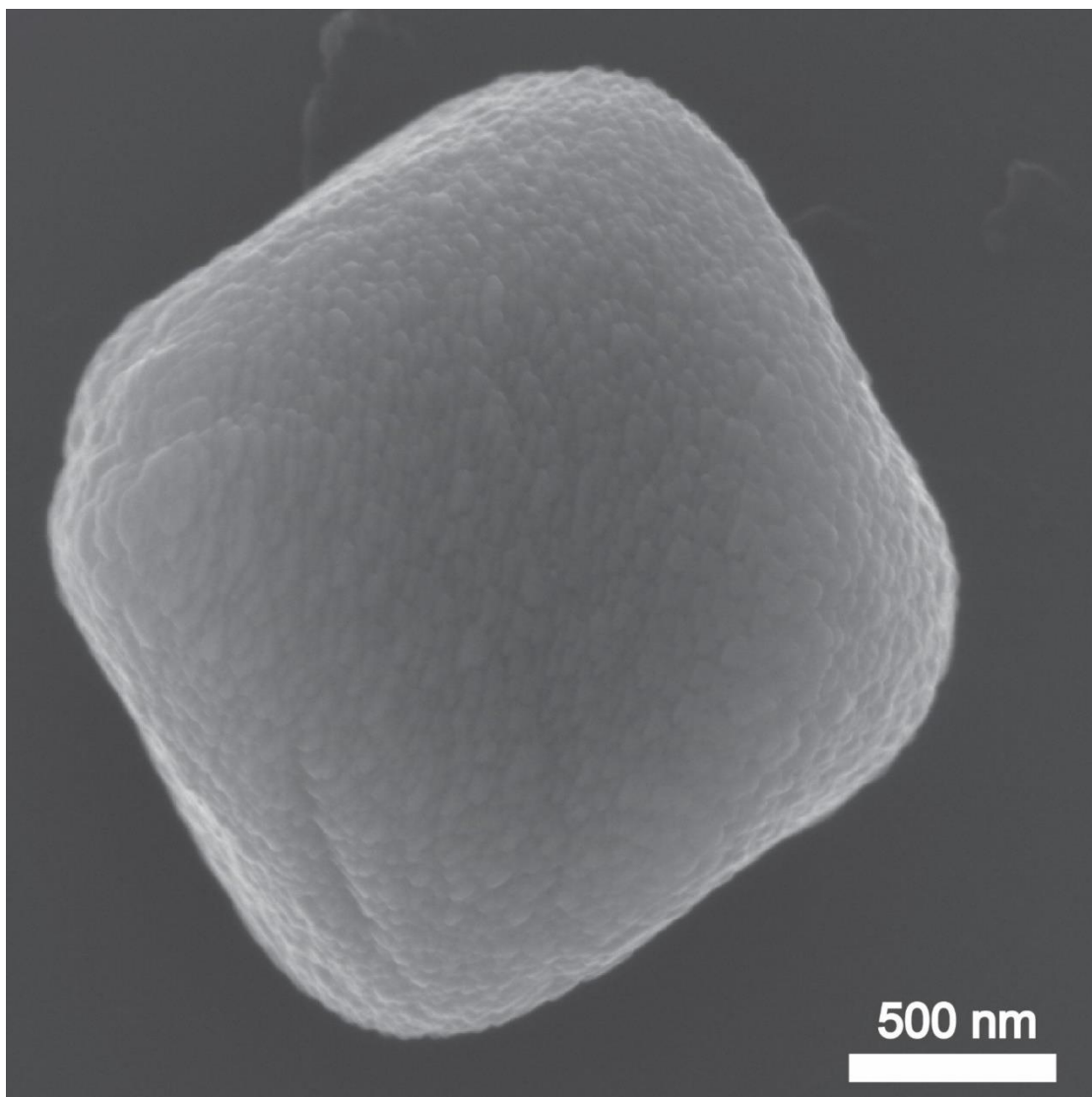


Figure 4.S1. Original SEM image of Fig. 4.2b. In Figure 4.2b, to better visualize the surface texture, contrast limited adaptive histogram equalization (CLAHE) in ImageJ was applied.⁵⁸

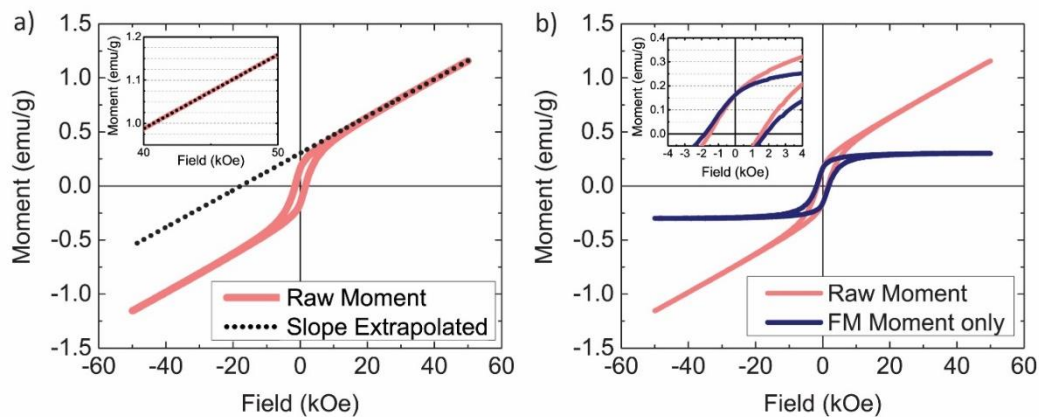


Figure 4.S2. Method for calculating and subtracting the antiferromagnetic (AFM) susceptibility (χ_{AFM}) from the 300 K field-dependent magnetization data in order to extract the remnant to saturation magnetization ratio (M_r/M_s) and coercive field (H_c). In this figure, the method is demonstrated for the polycrystalline hematite sample. (A, inset) First we fit the slope of the raw magnetization curve, shown in pink, in the high-field region from 40 to 50 kOe. This slope is χ_{AFM} and the average of three measurements is reported in Table 4.S1 below. (a) Next, we extrapolate this fit over the total magnetic field range, shown in the dotted black line. (b) The magnetization curve with the χ_{AFM} subtracted, shown in blue, now reflects only the ferromagnetic (FM) component of the magnetization. The saturation magnetization (M_s) is defined by the value of the FM magnetization curve at a 50 kOe. (B, inset) The remnant magnetization (M_r) is defined by the y-intercept of the FM magnetization curve. The coercive field (H_c) is defined by the x-intercept of the FM magnetization curve.

Table 4.S1. Calculated antiferromagnetic (AFM) susceptibility (χ_{AFM}) values for the 4 hematite samples.

Sample	χ_{AFM} (emu/g/kOe)
Mosaic Crystal	0.019*
Polycrystalline	0.018*
Single Crystal Nanoparticle	0.011
Bulk Single Crystal	0.022 [§]

[§] Data for bulk single crystal from Ref. ⁵⁶. *Values are the average of 3 measurements.

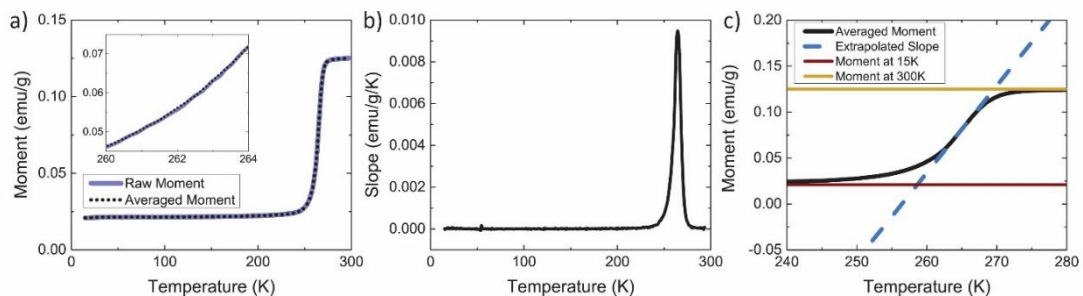


Figure 4.S3. Method based on Ref. ⁷¹ for calculating the Morin transition temperature (T_m), the sharpness of the Morin transition (ΔT_m), and the percent decrease in magnetization from 300 K to 15 K ($\Delta M/M_{300K}$) from the zero field-cooled temperature-dependent magnetization data. In this figure, the method is demonstrated for the polycrystalline hematite sample. (a) First the raw magnetization data is averaged using a binning method with the minimum bin size necessary to achieve a single maximum in the slope versus temperature. (A, inset) The average magnetization does not deviate significantly from the raw magnetization. (b) We calculate $\Delta M/\Delta T$ for sequential data points of the averaged magnetization data. The Morin transition temperature is defined as the temperature at which the slope is maximum. (c) To define the percent decrease in magnetization from 300 K to 15 K ($\Delta M/M_{300K}$), we define M_{300K} as the averaged magnetization value at 300 K (shown as horizontal line in yellow) and ΔM as the averaged magnetization value at 300 K minus the averaged magnetization value at 15 K (shown as a horizontal line in red). We define the sharpness of the Morin transition (ΔT_m) by the difference in temperature between the intersections of the extrapolated slope (blue dashed line) with M_{300K} (yellow line) and M_{15K} (red line).

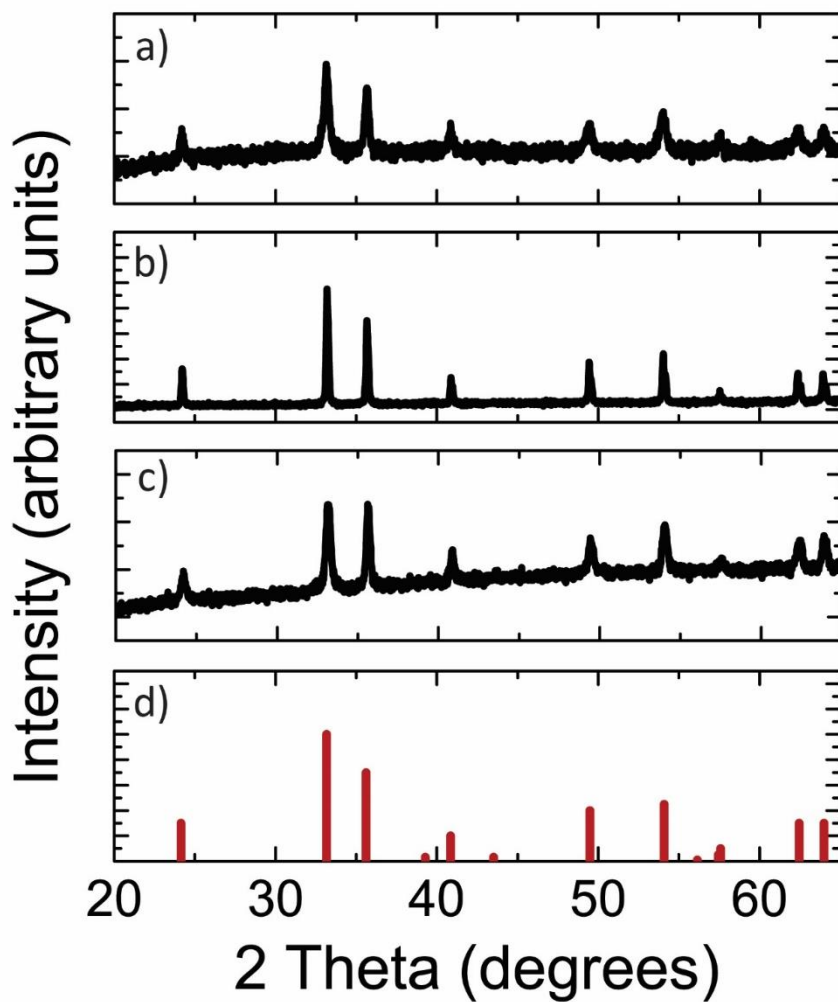


Figure 4.S4. Powder x-ray diffraction (XRD) of the (a) mosaic crystals of hematite, (b) polycrystalline hematite and (c) single crystal nanoparticles of hematite. (d) For reference, PDF (#00-033-0664) for hematite is shown to confirm that all three samples are single phase.

Table 4.S2. Crystallite sizes analysis (Scherrer) from Powder x-ray diffraction data (Fig. S4).

2 Theta (degrees)	(h k l)	Crystallite Size (Å)		
		Mosaic Crystal*	Polycrystalline	Single Crystal Nanoparticle
24.1	(0 1 2)	294 (8)	>1000	329 (34)
33.1	(1 0 4)	243 (4)	>1000	312 (11)
35.6	(1 1 0)	335 (6)	>1000	460 (19)
40.9	(1 1 3)	245 (8)	>1000	401 (43)
49.4	(0 2 4)	231 (6)	>1000	333 (38)
54.0	(1 1 6)	241 (4)	>1000	382 (34)

* Data for mosaic crystal is from Ref. ⁴⁶.

REFERENCES

- (1) Dunlop, J. W. C.; Fratzl, P. Multilevel Architectures in Natural Materials. *Scr. Mater.* **2013**, *68* (1), 8–12.
- (2) Weiner, S.; Addadi, L. Design Strategies in Mineralized Biological Materials. *J. Mater. Chem.* **1997**, *7* (5), 689–702.
- (3) Meldrum, F. C.; Cölfen, H. Controlling Mineral Morphologies and Structures in Biological and Synthetic Systems. *Chem. Rev.* **2008**, *108* (11), 4332–4432.
- (4) Nudelman, F.; Sommerdijk, N. A. J. M. Biomineralization as an Inspiration for Materials Chemistry. *Angew. Chemie - Int. Ed.* **2012**, *51* (27), 6582–6596.
- (5) Imai, H.; Oaki, Y. Bioinspired Hierarchical Crystals. *MRS Bull.* **2010**, *35*, 138.
- (6) Weber, E.; Pokroy, B. Intracrystalline Inclusions within Single Crystalline Hosts: From Biomineralization to Bio-Inspired Crystal Growth. *CrystEngComm* **2015**, *17* (31), 5873–5883.
- (7) Imai, H. Mesostructured Crystals : Growth Processes and Features. *Prog. Cryst. Growth Charact. Mater.* **2016**, *62* (2), 212–226.
- (8) Oaki, Y.; Imai, H. Recent Advances in Mesocrystals and Their Related Structures. *Nanoscience* **2013**, *1*, 1–28.
- (9) Kokubu, T.; Oaki, Y.; Hosono, E.; Zhou, H.; Imai, H. Biomimetic Solid-Solution Precursors of Metal Carbonate for Nanostructured Metal Oxides: MnO/Co and MnO-CoO Nanostructures and Their Electrochemical Properties. *Adv. Funct. Mater.* **2011**, *21* (19), 3673–3680.

- (10) Brif, A.; Ankonina, G.; Drathen, C.; Pokroy, B. Bio-Inspired Band Gap Engineering of Zinc Oxide by Intracrystalline Incorporation of Amino Acids. *Adv. Mater.* **2014**, *26* (3), 477–481.
- (11) Kim, Y.-Y.; Carloni, J. D.; Demarchi, B.; Sparks, D.; Reid, D. G.; Kunitake, M. E.; Tang, C. C.; Duer, M. J.; Freeman, C. L.; Pokroy, B.; et al. Tuning Hardness in Calcite by Incorporation of Amino Acids. *Nat. Mater.* **2016**, *15*, 903–910.
- (12) Koumoto, K.; Wang, Y.; Zhang, R.; Kosuga, A.; Funahashi, R. Oxide Thermoelectric Materials : A Nanostructuring Approach. *Annu. Rev. Mater. Res.* **2010**, *40*, 363–394.
- (13) Uchiyama, H.; Hosono, E.; Zhou, H.; Imai, H. Three-Dimensional Architectures of Spinel-Type LiMn₂O₄ Prepared from Biomimetic Porous Carbonates and Their Application to a Cathode for Lithium-Ion Batteries. *J. Mater. Chem.* **2009**, *19* (23), 4012.
- (14) Yao, R.; Cao, C.; Bai, J. Self-Assembly of Magnetite Mesocrystal Microdisks with Hierarchical Architectures. *CrystEngComm* **2013**, *15* (1), 3279.
- (15) Zhu, Y.; Zhan, Q.; Yang, J. C.; Bitla, Y.; Liu, P.; Li, C. I.; Liu, H. J.; Kumar, V. S.; Arenholz, E.; He, Q.; et al. Enhanced Structural and Magnetic Coupling in a Mesocrystal-Assisted Nanocomposite. *ACS Appl. Mater. Interfaces* **2016**, *8* (2), 1104–1111.
- (16) Yang, J.; Cheng, N. Mesocrystal-Embedded Functional Oxide Systems. *MRS Commun.* **2016**, *6* (3), 167–181.

- (17) Yang, J. C.; He, Q.; Zhu, Y. M.; Lin, J. C.; Liu, H. J.; Hsieh, Y. H.; Wu, P. C.; Chen, Y. L.; Lee, S. F.; Chin, Y. Y.; et al. Magnetic Mesocrystal-Assisted Magnetoresistance in Manganite. *Nano Lett.* **2014**, *14* (11), 6073–6079.
- (18) Jiao, F.; Harrison, A.; Jumas, J.; Chadwick, A. V; Kockelmann, W.; Bruce, P. G. Ordered Mesoporous Fe₂O₃ with Crystalline Walls. *J. Am. Ceram. Soc.* **2006**, *128* (17), 5468–5474.
- (19) Ganga, B. G.; Varma, M. R.; Santhosh, P. N. Evidence of Reduced Antiferromagnetic Transition in Mesocrystals of CuO Synthesized by a Surfactant-Free Solution Phase Method †. *CrystEngComm* **2015**, *17*, 7086–7093.
- (20) Scola, J.; Boullay, P.; Noun, W.; Popova, E.; Dumont, Y.; Fouchet, A.; Keller, N. Microstructure and Self-Exchange Coupling in a YFeO₃ Film. *J. Appl. Phys.* **2011**, *110* (4), 043928.
- (21) Reichel, V.; Kovács, A.; Kumari, M.; Bereczk-Tompa, É.; Schneck, E.; Diehle, P.; Pósfai, M.; Hirt, A. M.; Duchamp, M.; Dunin-Borkowski, R. E.; et al. Single Crystalline Superstructured Stable Single Domain Magnetite Nanoparticles. *Sci. Rep.* **2017**, *7* (October 2016), 45484.
- (22) Wetterskog, E.; Agthe, M.; Mayence, A.; Grins, J.; Wang, D.; Rana, S.; Ahniyaz, A.; Salazar-alvarez, G.; Bergström, L. Precise Control over Shape and Size of Iron Oxide Nanocrystals Suitable for Assembly into Ordered Particle Arrays. *Sci. Technol. Adv. Mater.* **2014**, *15*.

- (23) Ahniyaz, A.; Sakamoto, Y.; Bergstro, L. Magnetic Field-Induced Assembly of Oriented Superlattices from Maghemite Nanocubes. *Proc. Natl. Acad. Sci.* **2007**, *104* (45), 17570–17574.
- (24) Alben, R.; Becker, J. J.; Chi, M. C. Random Anisotropy in Amorphous Ferromagnets. *J. Appl. Phys.* **1978**, *49* (3), 1653–1658.
- (25) Herzer, G. Grain Structure and Magnetism of Nanocrystalline Ferromagnets. *IEEE Trans. Magn.* **1989**, *25* (5), 3327–3329.
- (26) Herzer, G. Soft-Magnetic Nanocrystalline Materials. *Scr. Metall. Mater.* **1995**, *33* (10–11), 1741–1756.
- (27) Darwin, C. G. XCII. The Reflexion of X-Rays from Imperfect Crystals. *Philos. Mag. Ser. 6* **1922**, *43* (257), 800–829.
- (28) Dunlop, D. J.; Özdemir, Ö. *Rock Magnetism: Fundamentals and Frontiers*; Cambridge University Press, 1997.
- (29) Legrand, A.; Chateigner, D. Orientation by Solidification in a Magnetic Field A New Process to Texture SmCo Compounds Used as Permanent Magnets. *J. Magn. Magn. Mater.* **1997**, *173*, 20–28.
- (30) Khlopkov, K.; Gutfleisch, O.; Hinz, D.; Müller, K.; Schultz, L.; Khlopkov, K.; Gutfleisch, O.; Hinz, D.; Müller, K.; Schultz, L. Evolution of Interaction Domains in Textured Fine-Grained Nd₂Fe₁₄B Magnets. *J. Appl. Phys.* **2007**, *102*.
- (31) Huy, N.; Thi, P.; Hai, N.; Thi, N.; Huyen, T. Inducing Anisotropy in Bulk Nd –

- Fe – Co – Al – B Nanocrystalline Alloys by Quenching in Magnetic Field. *J. Magn. Magn. Mater.* **2012**, *324* (7), 1435–1439.
- (32) Yan, A.; Zhang, W.; Zhang, H.; Shen, B. Melt-Spun Magnetically Anisotropic SmCo Ribbons with High Permanent Performance. *J. Magn. Magn. Mater.* **2000**, *210*, 10–14.
- (33) Zhang, T.; Liu, H.; Ma, Z.; Jiang, C. Single Crystal Growth and Magnetic Properties of 2 : 17-Type SmCo Magnets. *J. Alloys Compd.* **2015**, *637*, 253–256.
- (34) Zhang, D.; Yuan, X.; Yue, M.; Zhou, D.; Zhu, J.; Gao, X. Crystallographic Orientation-Dependent Magnetic Properties of a PrCo₅ Permanent Magnet Prepared by Hot Deformation. *CrystEngComm* **2016**, *18*, 2632–2641.
- (35) Crew, D. C.; Lewis, L. H. Effect of Grain Alignment on Magnetic Structure in Nanoscale Material. *IEEE Trans. Magn.* **2001**, *37* (4), 2512–2514.
- (36) He, S.; Zhang, H.; Rong, C.; Chen, R. Studies on the Magnetic Properties for Single-Phase Nanocrystalline FePt Magnets with Different Orientation Degrees. *J. Magn.* **2007**, *312*, 1–5.
- (37) Yao, Q.; Liu, W.; Zhang, Z. D. Effective Anisotropy Field in Anisotropic Nanostructured Ferromagnetic Materials. *Phys. Status Solidi* **2009**, *1715* (7), 1709–1715.
- (38) Jin, Y. M.; Wang, Y. U.; Kazaryan, A.; Wang, Y.; Laughlin, D. E. Magnetic Structure and Hysteresis in Hard Magnetic Nanocrystalline Film : Computer

- Simulation. *J. Appl. Phys.* **2002**, 92 (10), 6172–6181.
- (39) Kneller, E. F.; Hawig, R. The Exchange-Spring Magnet: A New Material Principle for Permanent Magnets. *IEEE Trans. Magn.* **1991**, 27 (4), 3588–3600.
- (40) Skomski, R. Giant Energy Product in Nanostructured Two-Phase Magnets. *Phys. Rev. B* **1993**, 48 (21), 15812–15816.
- (41) Skomski, R.; Manchanda, P.; Takeuchi, I. Geometry Dependence of Magnetization Reversal in Nanocomposite Alloys. **2014**, 66 (7), 1144–1150.
- (42) Fischer, R.; Schrefl, T.; Kronmüller, H.; Fidler, J. Grain-Size Dependence of Remanence and Coercive Field of Isotropic Nanocrystalline Composite Permanent Magnets. *J. Magn. Magn. Mater.* **1996**, 153 (1–2), 35–49.
- (43) Cui, W.; Takahashi, Y. K.; Hono, K. Nd₂Fe₁₄B / FeCo Anisotropic Nanocomposite Films with a Large Maximum Energy Product. *Adv. Mater.* **2012**, 24, 6530–6535.
- (44) Quesada, A.; Granados-Miralles, C.; López-Ortega, A.; Erokhin, S.; Lottini, E.; Pedrosa, J.; Bollero, A.; Aragón, A. M.; Rubio-Marcos, F.; Stingaciu, M.; et al. Energy Product Enhancement in Imperfectly Exchange-Coupled Nanocomposite Magnets. *Adv. Electron. Mater.* **2016**, 2 (4), 1500365.
- (45) Hernando, A. Exchange Interactions and Coercitivity in Multi-Phase Magnets. *J. Magn. Magn. Mater.* **1992**, 117 (1–2), 154–162.
- (46) Asenath-Smith, E.; Estroff, L. A. Sectioning of Individual Hematite Pseudocubes with Focused Ion Beam Enables Quantitative Structural

- Characterization at Nanometer Length Scales. *Microsc. Microanal.* **2014**, *20* (2), 1–10.
- (47) Sugimoto, T.; Muramatsu, A.; Sakata, K.; Shindo, D. Characterization of Hematite Particles of Different Shapes. *J. Colloid Interface Sci.* **1993**, *158*, 420–428.
- (48) Shindo, D.; Aita, S.; Park, G.-S.; Sugimoto, T. High-Voltage High-Resolution Electron Microscopy on Thin Films of Monodispersed Pseudocubic and Peanut-Typ Hematite Particles. *Mater. Trans.* **1993**, *34* (12), 1226–1228.
- (49) Park, G.; Shindo, D.; Waseda, Y.; Sugimoto, T. Internal Structure Analysis of Monodispersed Pseudocubic Hematite Particles by Electron Microscopy. *J. Colloid Interface Sci.* **1996**, *177* (1), 198–207.
- (50) Morrish, A. H. *Canted Antiferromagnetism: Hematite*; World Scientific Publishing Co. Pte. Ltd, 1994.
- (51) Eaton, J. A.; Morrish, A. H. Magnetic Domains in Hematite At and Above the Morin Transition. *J. Appl. Phys.* **1969**, *40* (8), 3180.
- (52) Maartense, I.; Searle, C. W. Domain Wall and Magnetoelastic Resonances in Hematite. *J. Appl. Phys.* **1971**, *42* (1971), 2349–2355.
- (53) Matijević, E.; Scheiner, P. Ferric Hydrous Oxide Sols. *J. Colloid Interface Sci.* **1978**, *63* (3).
- (54) Asenath-Smith, E.; Hovden, R.; Kourkoutis, L. F.; Estroff, L. A. Hierarchically Structured Hematite Architectures Achieved by Growth in a Silica Hydrogel. *J.*

Am. Chem. Soc. **2015**, *137* (15), 5184–5192.

- (55) Kim, Y.-Y.; Schenk, A. S.; Ihli, J.; Kulak, A. N.; Hetherington, N. B. J.; Tang, C. C.; Schmahl, W. W.; Griesshaber, E.; Hyett, G.; Meldrum, F. C. A Critical Analysis of Calcium Carbonate Mesocrystals. *Nat. Commun.* **2014**, *5*, 1–14.
- (56) Flanders, P. J.; Remeika, J. P. Magnetic Properties of Hematite Single Crystals. *Philos. Mag.* **1965**, *11* (114), 1271–1288.
- (57) Raming, T. P.; Winnubst, A. J. A.; van Kats, C. M.; Philipse, A. P. The Synthesis and Magnetic Properties of Nanosized Hematite (α -Fe₂O₃) Particles. *J. Colloid Interface Sci.* **2002**, *249* (2), 346–350.
- (58) Zuiderveld, K. Contrast Limited Adaptive Histogram Equalization. In *Graphic gems IV*; Heckbert, P. S., Ed.; Academic Press Professional, Inc., 1994; pp 474–485.
- (59) Yao, R.; Cao, C. Self-Assembly of α -Fe₂O₃ Mesocrystals with High Coercivity. *RSC Adv.* **2012**, *2* (5), 1979.
- (60) Rath, C.; Sahu, K. K.; Kulkarni, S. D.; Anand, S.; Date, S. K.; Das, R. P.; Mishra, N. C. Microstructure-Dependent Coercivity in Monodispersed Hematite Particles. *Appl. Phys. Lett.* **1999**, *75* (26), 4171.
- (61) Morris, P. R.; Flowers, J. W. Texture and Magnetic Properties. *Texture Cryst. Solids* **1981**, *4* (3), 129–141.
- (62) Skomski, R.; Coey, J. M. D. Magnetic Anisotropy — How Much Is Enough for a Permanent Magnet? *Scr. Mater.* **2016**, *112* (October), 3–8.

- (63) Özdemir, Ö.; Dunlop, D. J. Hysteresis and Coercivity of Hematite. *J. Geophys. Res. Solid Earth* **2014**, *119*, 2582–2594.
- (64) Kletetschka, G.; Wasilewski, P. J. Grain Size Limit for SD Hematite. *Phys. Earth Planet. Inter.* **2002**, *129* (1–2), 173–179.
- (65) Banerjee, S. New Grain Size Limits for Paleomagnetic Stability in Haematite. *Nat. Phys. Sci.* **1971**, *232*, 15–16.
- (66) Artman, J. O.; Murphy, J. C.; Foner, S. Magnetic Anisotropy in Antiferromagnetic Corundum-Type Sesquioxides. *Phys. Rev.* **1965**, *138* (3A), 912–917.
- (67) Muench, G. J.; Arajs, S.; Matijević, E. The Morin Transition in Small. *Phys.Stat.Sol.(a)* **1985**, *92* (187).
- (68) Schroerer, D.; Nininger Jr., R. C. Morin Transition in Alpha-Fe₂O₃ Microcrystals. *Phys. Rev. Lett.* **1967**, *19* (11), 632.
- (69) Frandsen, C.; Mørup, S. Spin Rotation in Alpha-Fe₂O₃ Nanoparticles by Interparticle Interactions. *Phys. Rev. Lett.* **2005**, *94* (2), 027202.
- (70) Gee, S.; Hong, Y.; Sur, J. C.; Erickson, D. W.; Park, M. H.; Jeffers, F. Spin Orientation of Hematite Nanoparticles During the Morin Transition. *IEEE Trans. Magn.* **2004**, *40* (4), 2691–2693.
- (71) Muench, G. J.; Arajs, S.; Matijević, E. Effects of Magnetic Field, Strain, and Size on the Morin Temperature of Spherical α -Fe₂O₃ Particles. *IEEE Trans. Magn.* **1982**, *18* (6), 1583–1585.

- (72) Özdemir, Ö.; Dunlop, D. J.; Berquó, T. S. Morin Transition in Hematite: Size Dependence and Thermal Hysteresis. *Geochemistry, Geophys. Geosystems* **2008**, *9* (10), 1.
- (73) Gallagher, P. K.; Gyorgy, E. M. Morin Transition and Lattice Spacing of Hematite as a Function of Particle Size. *Phys. Rev.* **1969**, *180* (2), 622.
- (74) Besser, P. J.; Morrish, A. H.; Searle, C. W. Magnetocrystalline Anisotropy of Pure and Doped Hematite. *Phys. Rev.* **1967**, *153* (2), 632.
- (75) Mitra, S.; Das, S.; Basu, S.; Sahu, P.; Mandal, K. Shape- and Field-Dependent Morin Transitions in Structured α -Fe₂O₃. *J. Magn. Magn. Mater.* **2009**, *321* (18), 2925–2931.
- (76) Wang, J.; Aguilar, V.; Li, L.; Li, F.; Wang, W.; Zhao, G. Strong Shape-Dependence of Morin Transition in α -Fe₂O₃ Single-Crystalline Nanostructures. *Nano Res.* **2015**, *8* (6), 1906–1916.
- (77) Bengoa, J. F.; Alvarez, A. M.; Bianchi, A. E.; Punte, G.; Vandenberghe, R. E.; Mercader, R. C.; Marchetti, S. G. The Morin Transition in Nanostructured Pseudocubic Hematite: Effect of the Intercrystallite Magnetic Exchange. *Mater. Chem. Phys.* **2010**, *123* (1), 191–198.
- (78) Mørup, S.; Hansen, M. F.; Frandsen, C. Magnetic Interactions between Nanoparticles. *Beilstein Journal of Nanotechnology*. 2010, pp 182–190.

CHAPTER 5

EXPLORING REACTION PATHWAYS IN THE HYDROTHERMAL GROWTH OF PHASE-PURE BISMUTH FERRITES*

5.1 Abstract

Phase-pure bismuth ferrites (BiFeO_3 and $\text{Bi}_2\text{Fe}_4\text{O}_9$) are grown using hydrothermal synthesis. In addition to varying the KOH, bismuth, and iron salt concentrations to tune which crystalline phases are formed, we identified that a 48-hour, pre-furnace, room temperature reaction is critical for the formation of phase-pure BiFeO_3 . To understand the reaction pathways leading to the different bismuth ferrite phases, we investigate the changes in composition of the intermediate products as a function of reagent concentrations and room temperature reaction times. During the syntheses that included a room temperature reaction, $\text{Bi}_{25}\text{FeO}_{40}$ is formed in the intermediate products, and BiFeO_3 is the majority phase of the final products. The BiFeO_3 crystals grown using this method are clusters of faceted sub-units. These results indicate that forming $\text{Bi}_{25}\text{FeO}_{40}$ is a productive route to the formation of BiFeO_3 . $\text{Bi}_2\text{Fe}_4\text{O}_9$ is formed via an alternate reaction pathway that proceeded via an amorphous precursor. This improved understanding of how hydrothermal synthesis can be used to control the phase-purity and morphology of bismuth ferrites opens doors to explore the multiferroic properties of BiFeO_3 with complex morphologies.

5.2 Introduction

BiFeO_3 has gained much attention for its promise as the only known room-

* Reproduced from Goldman, A.R., Fredricks, J.L., Estroff, L.A. Exploring reaction pathways in the hydrothermal growth of phase-pure bismuth ferrites, *J. Cryst. Growth* .2017 468, 104–109. doi:10.1016/j.jcrysgro.2016.09.054, with the permission of Elsevier.

temperature, single-phase magnetoelectric multiferroic material ^{1,2}. One of the largest challenges to exploring the magnetoelectric properties of BiFeO₃ has been the phase-pure growth of BiFeO₃, as often other ternary phases such as Bi₂Fe₄O₉ and Bi₁₂₅FeO₄₀ are also produced. Recently, it has been reported that BiFeO₃ is amenable to growth by hydrothermal synthesis, which allows for simultaneous control of phase and crystal morphology ³⁻⁶. A plethora of experimental variables have been used to achieve phase-pure BiFeO₃ in the literature ⁷⁻¹⁴, however, further understanding of which variables control which phases are formed is needed to establish robust and tunable syntheses.

By systematically controlling multiple experimental variables, we developed a robust, tunable, additive-free synthesis that yields two different bismuth iron oxides in phase-pure form, dependent on well-defined parameters. We achieved phase-pure BiFeO₃ by adding a 48 hour room temperature reaction time to the synthesis. By characterizing the intermediate products prior to furnace treatment in conjunction with the final products, we elucidate elements of the growth pathways for different bismuth iron oxides.

5.3 Experimental Methods

5.3.1 Materials

All reagents were used as received without further purification: Bismuth (III) nitrate pentahydrate (≥98.0%, ACS reagent, Sigma Aldrich), Iron (III) nitrate nonahydrate

($\geq 98.0\%$, ACS reagent, Sigma Aldrich), Potassium hydroxide ($\sim 45\%$, for HPLC, Sigma Aldrich), Nitric acid (70%, ACS reagent, Sigma Aldrich).

5.3.2 Methods

Bismuth ferrite crystals were grown using hydrothermal synthesis. Crystallization solutions were prepared in various concentrations (Table 1). Bismuth and iron salts were first dissolved in a minimum volume of HNO_3 to produce a concentration of 10 mM or 100 mM in the final 80 mL reaction volume. For the 10 mM final concentration, 0.388 g $\text{Bi}(\text{NO}_3)_3 \cdot 5\text{H}_2\text{O}$ and 0.323 g $\text{Fe}(\text{NO}_3)_3 \cdot 9\text{H}_2\text{O}$ were dissolved in 2 mL of 5 M HNO_3 and for the 100 mM final concentration, 3.881 g $\text{Bi}(\text{NO}_3)_3 \cdot 5\text{H}_2\text{O}$ and 3.232 g $\text{Fe}(\text{NO}_3)_3 \cdot 9\text{H}_2\text{O}$ were dissolved in 4 mL of 5 M HNO_3 . The nitric acid, bismuth and iron salt solution was stirred (covered) for at least one hour to allow for complete dissolution of the salts. Deionized water was added to reach a volume of 18 mL and the solution stirred for at least an additional 10 minutes. For a final KOH concentration of 6 M or 9 M in the final 80 mL volume, 62 mL of the appropriate concentration KOH solution was prepared separately and added to a 125 mL Teflon liner of a Parr vessel (Parr Instrument Company, USA). Using a syringe pump, the Bi^{3+} and Fe^{3+} solution was added drop-wise at 0.3 mL/min to the KOH solution under vigorous stirring. For the synthesis with no room temperature reaction, after completion of the drop-wise addition, the brown solution was sealed in the Parr vessel and immediately transferred to the furnace. For the synthesis with 48 hours of room temperature reaction time, after completion of the drop-wise addition, the solution stirred (covered) at room temperature under vigorous stirring before furnace treatment. The furnace conditions remained constant for all experiments with a

1°C/min ramp rate to 200°C for 12 hours. The furnace was allowed to cool naturally to room temperature prior to washing the products in 1 M HNO₃ and deionized water via centrifugation. Powders were lyophilized prior to analysis. Between syntheses the Teflon Parr vessel liner needed to be soaked in concentrated hydrochloric acid in order to remove any trace bismuth ferrites that would otherwise preferentially seed growth during subsequent reactions.

In experiments where the intermediate products were analyzed, after the drop-wise addition of the bismuth and iron solution to the base solution, the brown slurry was centrifuged to separate the solid intermediate products from the supernatant. To identify the intermediate products, x-ray diffraction was performed. For the synthesis where the soluble salts were removed, the intermediate solid precipitate was washed three times in deionized water by centrifugation and then lyophilized prior to resuspension in 80 mL of 9 M KOH and furnace treatment.

5.3.3 Characterization

Phase analysis was performed via powder x-ray diffraction (XRD) using a Scintag theta-theta diffractometer with Cu K α (1.54 Å) radiation, operating at 40 kV and 40 mA with scan rates of 2.5-4°/min. XRD patterns were compared with the Joint Committee on Powder Diffraction Standards (JCPDS) database. The lyophilized powders were carbon-coated and imaged using a Mira3 LM field emission scanning electron microscopy (SEM) at 10 keV.

5.4 Results

The goal of this research was to develop a robust synthesis of BiFeO₃. Table 1 provides a summary of the reaction conditions used for each synthesis. Briefly, after

complete dissolution of the bismuth and iron salts in concentrated nitric acid, this transparent, light yellow solution is added drop-wise to a concentrated base solution under vigorous stirring. During the drop-wise addition, an opaque brown slurry forms, which lightens in color with prolonged stirring at room temperature (room temperature reaction time). After hydrothermal treatment, the resulting powders are analyzed by XRD and SEM. Visually, the BiFeO_3 powders appear black, while $\text{Bi}_2\text{Fe}_4\text{O}_9$ appears orange. In some syntheses, trace amounts of yellow Bi_2O_3 or red Fe_2O_3 were also present, but these binary products could be removed by a dilute nitric acid wash.

Table 5.1. Summary of hydrothermal growth conditions and intermediate and final phases present as identified by powder x-ray diffraction.

Experiment Label	[Bi³⁺] = [Fe³⁺]	[KOH]	Room Temperature Reaction Time	Intermediate Phases	Final Phases
10mM/0hr	10 mM	6 M	0 hours	Amorphous	Bi ₂ Fe ₄ O ₉
10mM/48hr	10 mM	6 M	48 hours	Amorphous + unidentified crystalline	BiFeO ₃ + α -Fe ₂ O ₃ + unidentified
100mM/0hr	100 mM	9 M	0 hours	Bi ₂₅ FeO ₄₀	BiFeO ₃ + Bi ₂ Fe ₄ O ₉
100mM/48hr	100 mM	9 M	48 hours	Bi ₂₅ FeO ₄₀ + unidentified crystalline	BiFeO ₃

Powder x-ray diffraction of the products formed using the 10mM/0hr reaction conditions indicates that phase-pure $\text{Bi}_2\text{Fe}_4\text{O}_9$ crystals are produced (Fig. 5.1a). In contrast, XRD of the products formed using the 100mM/48hr reaction conditions reveals that phase-pure BiFeO_3 crystals are formed at the higher salt concentrations with a 48 hour room temperature reaction (Fig. 5.1d). Morphologies of both phase-pure samples were imaged by SEM. $\text{Bi}_2\text{Fe}_4\text{O}_9$ forms flat, plate-like crystals that are on average 500 nm long and 100 nm thick (Fig. 5.S1). These morphologies are consistent with those from other reports^{15,16}. The BiFeO_3 particles are large 150-200 μm clusters of smaller faceted crystals, which are 20-40 μm (Fig. 5.2a).

To understand the impact of each variable (e.g., salt concentration, room temperature reaction time, and KOH concentration) in the synthesis, we analyzed samples grown under “exchanged” conditions (Table 5.1). In contrast to the XRD patterns of phase-pure samples (Fig.5.1a,d), the 100mM/0hr and the 10mM/48hr products exhibit clear evidence of secondary phases along with a majority BiFeO_3 phase (Fig. 5.1b,c). To confirm the necessity of pairing 100mM/48hr with 9 M KOH, and 10mM/0hr with 6 M KOH to obtain phase-pure crystals of BiFeO_3 and $\text{Bi}_2\text{Fe}_4\text{O}_9$ respectively, we also performed experiments under “exchanged” KOH concentrations. The growths using 100mM/48hr with 6 M KOH and 10mM/0hr with 9 M KOH both produced BiFeO_3 with several impurity phases (Fig. 5.S2).

Based upon these results, it is clear that there are specific criteria under which the different phase-pure bismuth iron oxide phases form. By studying the trends between samples grown under systematically-varied growth conditions, we aimed to learn about the crystal growth pathways that favor the formation of one bismuth iron

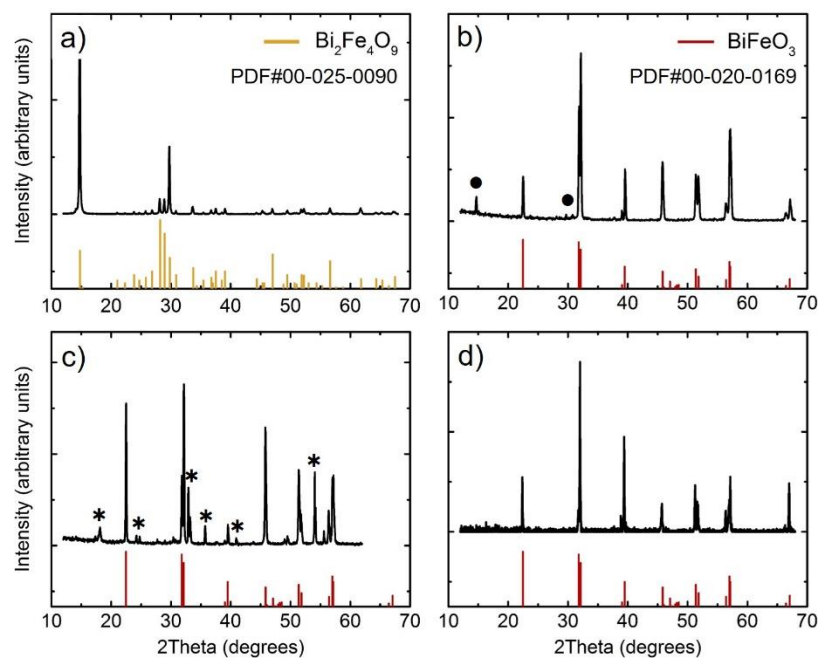


Figure 5.1. Powder x-ray diffraction patterns of the final products of bismuth iron oxide hydrothermal synthesis experiments. a) The 10mM/0hr reaction conditions yield phase-pure $\text{Bi}_2\text{Fe}_4\text{O}_9$. b) The 100mM/0hr conditions produce a majority phase BiFeO_3 with small amounts of $\text{Bi}_2\text{Fe}_4\text{O}_9$ (indicated by ●). c) The 10mM/48hr conditions produce a majority phase BiFeO_3 with several impurity phases (indicated by *). d) The 100mM/48hr conditions yield phase-pure BiFeO_3 .

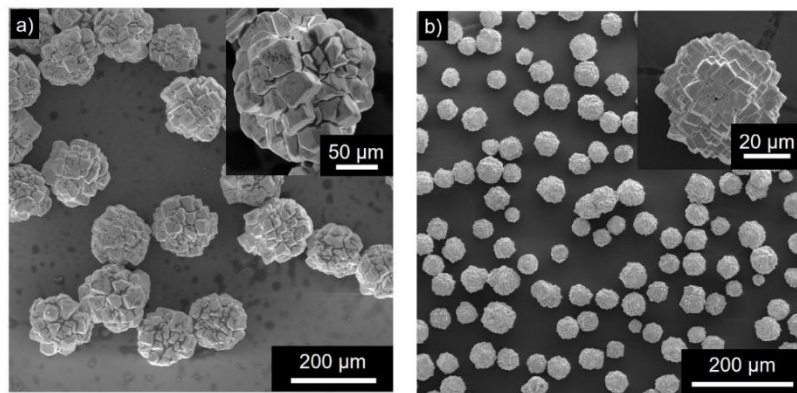


Figure 5.2. SEM images of (a) Phase-pure BiFeO₃ formed by the 100mM/48hr reaction conditions and (b) Phase-pure BiFeO₃ formed by a modified 100mM/48hr synthesis during which the soluble ions present after the room temperature reaction are removed and replaced with pure KOH.

oxide over another. Phase-pure $\text{Bi}_2\text{Fe}_4\text{O}_9$ is only formed at 10 mM $[\text{Bi}^{3+}]=[\text{Fe}^{3+}]$ and 6 M KOH with no room temperature reaction (Fig. 5.1a). Altering the phase-pure $\text{Bi}_2\text{Fe}_4\text{O}_9$ synthesis by adding a room temperature reaction step to the procedure eliminates any trace of $\text{Bi}_2\text{Fe}_4\text{O}_9$ from the final products and instead the majority phase becomes BiFeO_3 (Fig. 5.1c).

Both syntheses at 100 mM $[\text{Bi}^{3+}]=[\text{Fe}^{3+}]$ and 9 M KOH favor the formation of BiFeO_3 (Fig. 5.1b,d). This data suggests that higher concentrations of the bismuth, iron and hydroxide salts appear to promote the formation of BiFeO_3 over other bismuth iron oxide phases. However, use of higher concentrations of precursor salts does not guarantee phase-pure BiFeO_3 formation as evidenced by the 100mM/0hr growth, which yielded inconsistent results from growth to growth, and often contained $\text{Bi}_2\text{Fe}_4\text{O}_9$ (Fig. 5.1b). The inclusion of a room temperature reaction step (for 12-48 hours) to the synthesis prior to the hydrothermal treatment ensured that the final products will be phase-pure BiFeO_3 .

We aimed to understand why the prolonged room temperature reaction is required for growing phase-pure BiFeO_3 , but is unfavorable for growing $\text{Bi}_2\text{Fe}_4\text{O}_9$. To investigate the role of the room temperature reaction time, we isolated and characterized the solid intermediate products formed in solution prior to furnace treatment (Fig. 5.3). There are striking differences between the intermediate phases that lead to phase-pure $\text{Bi}_2\text{Fe}_4\text{O}_9$ and phase-pure BiFeO_3 . The intermediate products that lead to phase-pure $\text{Bi}_2\text{Fe}_4\text{O}_9$ are amorphous (Fig. 5.3a), while those that lead to phase-pure BiFeO_3 are a mixture of crystalline $\text{Bi}_{25}\text{FeO}_{40}$, amorphous material, and

unidentified crystalline phases (Fig. 5.3d). More surprisingly, the 10mM/48hr reaction conditions, which produced a multi-phase mixture of final products, yield intermediate products that contain only one crystalline phase, $\text{Bi}_{25}\text{FeO}_{40}$ (Fig. 5.3c). The intermediate products for the 100mM/0hr growth do not contain any $\text{Bi}_{25}\text{FeO}_{40}$, but instead are a mixture of amorphous and unidentified crystalline phases (Fig. 5.3b), which further confirms that a prolonged room temperature reaction is necessary for growth of $\text{Bi}_{25}\text{FeO}_{40}$.

To further investigate the reaction pathway for phase-pure BiFeO_3 following the 100mM/48hr reaction, we considered the composition of the isolated intermediates. The crystalline intermediate product, $\text{Bi}_{25}\text{FeO}_{40}$, is highly Bi-rich. If all of the bismuth in the flask is converted into $\text{Bi}_{25}\text{FeO}_{40}$ and the $\text{Bi}_{25}\text{FeO}_{40}$ alone transformed to BiFeO_3 , we would expect the final yield of BiFeO_3 to be 1/25 of the theoretical yield. However, the yield of phase-pure BiFeO_3 for the 100mM/48hr reaction is greater than 90% of the theoretical yield, so nearly all of the bismuth and iron in the original reaction mixture is converted into BiFeO_3 . Therefore, the Fe^{3+} in the final BiFeO_3 must come from either soluble Fe^{3+} or an Fe-rich solid phase.

We next endeavored to determine whether or not the solid intermediates contain all of the necessary ions to form phase-pure BiFeO_3 or if soluble ions in the supernatant are also necessary. Beginning with the 100mM/48hr reaction conditions, we isolated and rinsed the solid intermediate product by centrifugation and disposed of the supernatant, which would contain any soluble ions. We then redispersed the solid intermediate products in 80 mL of 9 M KOH and proceeded with hydrothermal treatment. The final product remained phase-pure BiFeO_3 (Fig. 5.S3) and the yield of

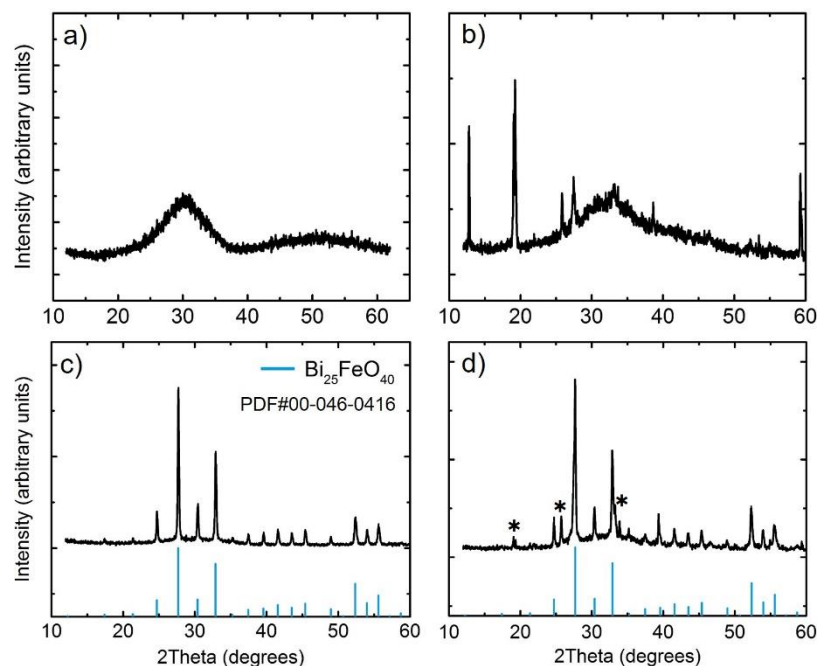


Figure 5.3. Powder x-ray diffraction patterns of the intermediate products formed prior to furnace treatment. (a) Amorphous intermediate isolated from the 10mM/0hr reaction, which leads to the formation of phase-pure $\text{Bi}_2\text{Fe}_4\text{O}_9$. (b) A mixture of amorphous and unidentified crystalline products isolated from the 100mM/0hr reaction. (c) Crystalline $\text{Bi}_{25}\text{FeO}_{40}$ isolated prior to furnace treatment for the reaction condition 10mM/48hr. (d) A mixture of crystalline $\text{Bi}_{25}\text{FeO}_{40}$, amorphous material and unidentified crystalline products isolated from the 100mM/48hr reaction, which forms phase-pure BiFeO_3 after furnace treatment.

BiFeO₃ was 90% of the theoretical yield, confirming that all of the necessary ions were present in the solid intermediate product.

The morphology of the BiFeO₃ formed after removal of the soluble ions is different than the particles formed by the original 100mM/48hr reaction conditions (Fig. 5.2). The BiFeO₃ particles formed from the washed intermediates are much smaller (~50 μm, with the subunits less than 10 μm) than those from the original reaction conditions (Fig. 5.2b). In addition, the subunits within an individual cluster appear to be more oriented with respect to one another as compared to the larger, more disordered clusters formed by the original reaction conditions (insets in Fig. 5.2a,b).

5.5 Discussion

In this work, we developed a robust, highly reproducible and tunable synthesis of two different phase-pure compositions of bismuth iron oxide. The concentrations of the iron and bismuth salts and the length of the room temperature reaction time control whether phase-pure BiFeO₃ or Bi₂Fe₄O₉ is produced. By investigating the intermediate products formed during the room temperature reaction, we conclude that there are distinct reaction pathways leading to each phase (Fig. 5.4). Upon mixing the lower salt concentrations (10 mM) with concentrated base, an amorphous solid forms (Fig. 5.3a), which upon hydrothermal treatment transforms to phase-pure Bi₂Fe₄O₉ (Fig. 5.1a). When a room temperature reaction is added, there is an alternate growth pathway that proceeds via crystalline intermediates, the major phase being Bi₂₅FeO₄₀ (Fig. 5.3c,d). Upon hydrothermal treatment of the higher salt concentrations (100 mM) with the addition of a room temperature reaction, this reaction pathway yields phase-pure BiFeO₃ (Fig. 5.1d). These results are consistent with those of Cai, et al., who

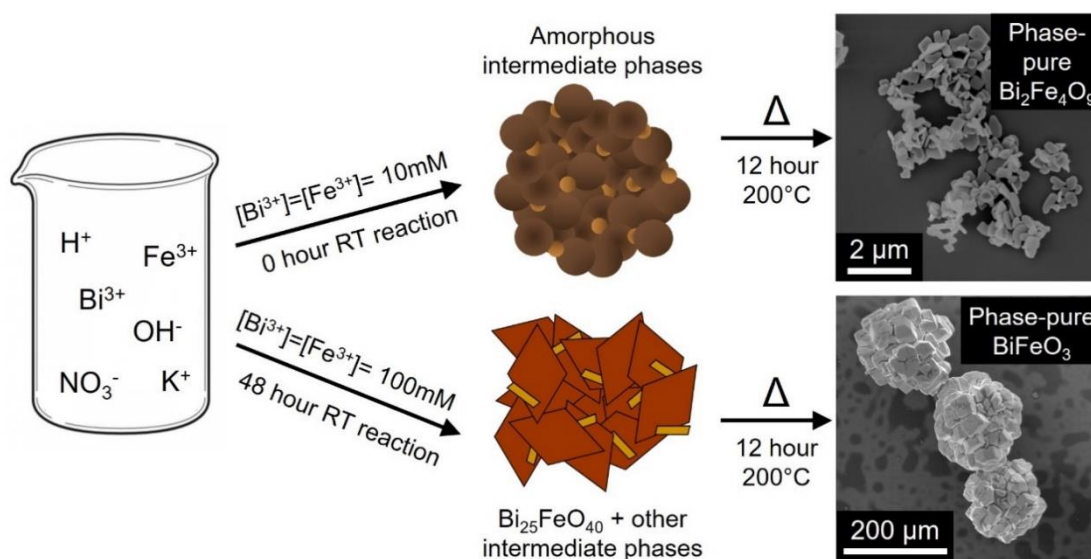


Figure 5.4. Schematic representation of the proposed reaction pathways that lead to phase-pure $\text{Bi}_2\text{Fe}_4\text{O}_9$ and BiFeO_3 . By choosing the top pathway, using 10mM/0hr, the reaction proceeds via an amorphous intermediate, which upon furnace treatment forms phase-pure platelets of $\text{Bi}_2\text{Fe}_4\text{O}_9$. By choosing the bottom pathway, using 100mM/48hr, the reaction proceeds via a crystalline intermediate product that includes $\text{Bi}_{25}\text{FeO}_{40}$ and other crystalline phases, which after furnace treatment transform to well-defined, large aggregates of phase-pure BiFeO_3 .

proposed a reaction mechanism where solid $\text{Bi}_{25}\text{FeO}_{40}$ reacts with the less soluble $[\text{Fe}(\text{OH})_4]^-$ to ultimately form BiFeO_3 ¹⁷, and with others who observe that $\text{Bi}_{25}\text{FeO}_{40}$ often forms at lower $[\text{OH}^-]$, shorter furnace reaction times, or lower furnace temperatures, but that increasing any of these three variables will instead yield BiFeO_3 ^{18–20}. Further investigation is necessary to reveal how the $\text{Bi}_{25}\text{FeO}_{40}$ and other solid intermediates, some of which must be Fe-rich, transform during hydrothermal treatment in concentrated base to ultimately form faceted BiFeO_3 particles.

The morphologies of the BiFeO_3 particles are interesting both from a mechanistic as well as a properties perspective. While rinsing away the soluble ions from the solid intermediate did not change the phase (Fig. 5.S3), it significantly alters the particle morphology (Fig. 5.2). The blocky BiFeO_3 aggregates grown following the 100mM/48hr reaction conditions with no rinsing (Fig. 5.2a) are ~3 times larger than most of those grown by others^{5,7,19}. When we washed away the soluble ions prior to furnace treatment, the BiFeO_3 aggregates become smaller, ~50 μm , and similar in size to those of Suzuki, et al., who also removed the soluble ions via washing prior to furnace treatment⁵. In addition to the change in overall size, the faceted sub-units become more well-organized, again consistent with previous reports [5]. While there are literature reports of individual BiFeO_3 micro-cubes^{3,9,21,22} or disorganized aggregates of BiFeO_3 particles^{4,18}, there are only a few reports of well-organized aggregates of faceted sub-units^{5,7,19}, like those that we grow (Fig. 5.2b). These oriented aggregates are suggestive of an oriented-attachment growth mechanism, as suggested by others, [5,18] in which pre-formed crystalline or amorphous clusters come together during growth²³. By removing the soluble ions, the crystallographic fidelity of this

aggregation is improved, hinting at an important role for the solution chemistry in directing the growth. Further studies are required to understand how washing away the soluble ions in the intermediate product affects the orientation of the subunits with respect to one another within the BiFeO_3 aggregates. These unique architectures of nanostructured BiFeO_3 will allow us to access physical (magnetoelectric, photocatalytic, photovoltaic, etc.) properties that may not be accessible with bulk or thin film BiFeO_3 ⁶.

5.6 Conclusion

Hydrothermal synthesis was used to grow phase-pure BiFeO_3 and $\text{Bi}_2\text{Fe}_4\text{O}_9$ crystals. Phase-pure $\text{Bi}_2\text{Fe}_4\text{O}_9$ is formed using 10 mM Bi^{3+} and Fe^{3+} , 6 M KOH and no room temperature reaction time. Phase-pure BiFeO_3 is formed using 100 mM Bi^{3+} and Fe^{3+} , 9 M KOH and a 12-48 hour room temperature reaction. To understand the role of the room temperature reaction time, we investigated the intermediate products formed with and without the room temperature reaction. During the room temperature reaction, $\text{Bi}_{25}\text{FeO}_{40}$ forms and upon furnace treatment forms BiFeO_3 . The BiFeO_3 crystals formed are aggregates of faceted subunits. When the soluble ions in the intermediate product are removed by washing, the size of the aggregate and of the faceted subunits both shrink by a factor of 2-3 and the subunits appear more oriented with respect to one another. Further studies will investigate how the $\text{Bi}_{25}\text{FeO}_{40}$ transforms to BiFeO_3 as well as how the aggregates of faceted subunits form. With the improved understanding of how to control the selective growth of phase-pure BiFeO_3 or $\text{Bi}_2\text{Fe}_4\text{O}_9$, our work can be expanded to further develop synthesis-morphology relations for bismuth ferrites or other complex oxides. Our development of a tunable

growth of oriented aggregates of BiFeO_3 allows for us to begin to explore the multiferroic properties of BiFeO_3 with complex morphologies.

5.7 Acknowledgements

We acknowledge support from the NSF (DMR 1210304) and A.R.G. acknowledges the NSF Graduate Research Fellowship Program (GRF, DGE-1144153). We also acknowledge the Engineering Learning Initiatives Undergraduate Research Program at Cornell University for their support of J.L.F. This work made use of the Cornell Center for Materials Research Shared Facilities which are supported through the NSF MRSEC program (DMR-1120296).

5.8 Supporting Information

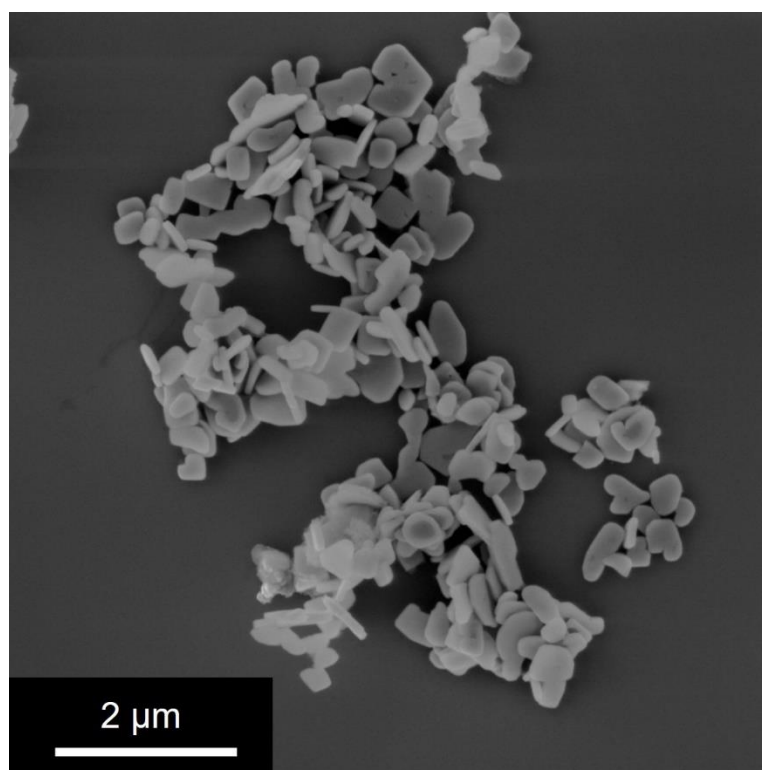


Figure 5.S1. Scanning electron micrograph of phase-pure $\text{Bi}_2\text{Fe}_4\text{O}_9$ formed by the 10mM/0hr reaction conditions.

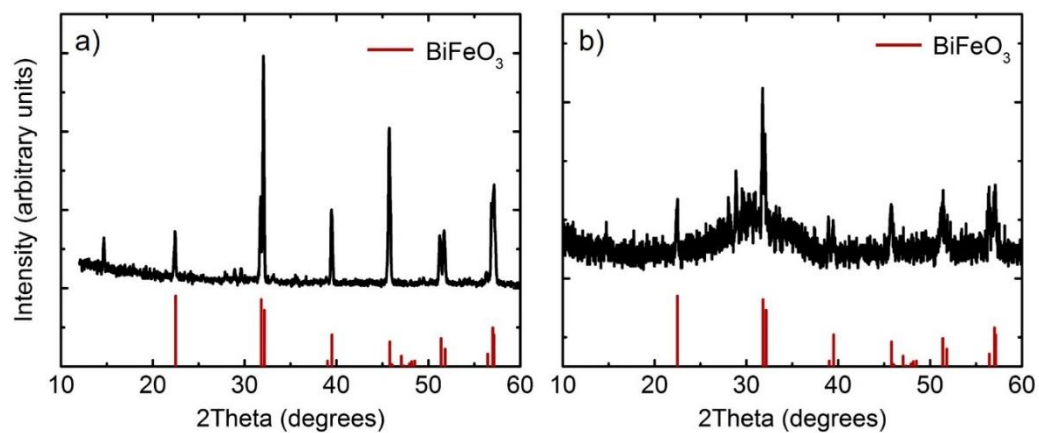


Figure 5.S2. Powder x-ray diffraction patterns of (a) 100mM/48hr with 6 M KOH and (b) 10mM/0hr with 9 M KOH, both of which form majority BiFeO_3 , but both contain impurity phases. PDF#00-020-0169 of BiFeO_3 shown for reference.

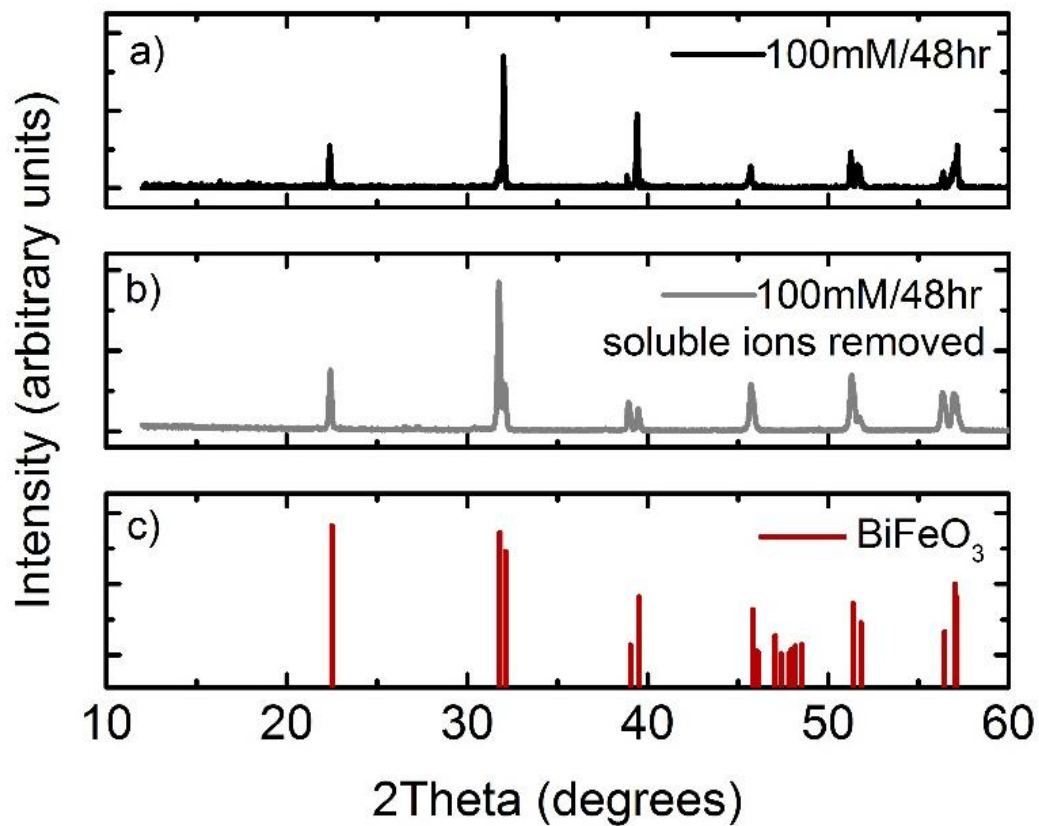


Figure 5.S3. Powder x-ray diffraction patterns of (a) phase-pure BiFeO₃ grown following the 100mM/48hr reaction conditions, (b) phase-pure BiFeO₃ grown following 100mM/48hr with the soluble ions in the intermediate products removed. (c) PDF#00-020-0169 of BiFeO₃ shown for reference.

REFERENCES

- (1) Catalan, G.; Scott, J. F. Physics and Applications of Bismuth Ferrite. *Adv. Mater.* **2009**, *21* (24), 2463–2485.
- (2) Ederer, C.; Spaldin, N. A. Weak Ferromagnetism and Magnetoelectric Coupling in Bismuth Ferrite. *Phys. Rev. B - Condens. Matter Mater. Phys.* **2005**, *71* (6), 1–4.
- (3) Li, S.; Lin, Y. H.; Zhang, B. P.; Wang, Y.; Nan, C. W. Controlled Fabrication of BiFeO₃ Uniform Microcrystals and Their Magnetic and Photocatalytic Behaviors. *J. Phys. Chem. C* **2010**, *114* (7), 2903–2908.
- (4) Chen, C.; Cheng, J.; Yu, S.; Che, L.; Meng, Z. Hydrothermal Synthesis of Perovskite Bismuth Ferrite Crystallites. *J. Cryst. Growth* **2006**, *291* (1), 135–139.
- (5) Suzuki, K.; Tokudome, Y.; Tsuda, H.; Takahashi, M. Morphology Control of BiFeO₃ Aggregates via Hydrothermal Synthesis. *J. Appl. Crystallogr.* **2016**, *49* (1), 168–174.
- (6) Zhang, Q.; Sando, D.; Nagarajan, V. Chemical Route Derived Bismuth Ferrite Thin Films and Nanomaterials. *J. Mater. Chem. C* **2016**, *4*, 4092–4124.
- (7) Xu, X.; Xu, Q.; Huang, Y.; Hu, X.; Huang, Y.; Wang, G. Control of Crystal Phase and Morphology in Hydrothermal Synthesis of BiFeO₃ Crystal. *J. Cryst. Growth* **2016**, *437*, 42–48.
- (8) Han, J. T.; Huang, Y. H.; Wu, X. J.; Wu, C. L.; Wei, W.; Peng, B.; Huang, W.;

- Goodenough, J. B. Tunable Synthesis of Bismuth Ferrites with Various Morphologies. *Adv. Mater.* **2006**, *18* (16), 2145–2148.
- (9) Zhou, J.-P.; Yang, R.-L.; Xiao, R.-J.; Chen, X.-M.; Deng, C.-Y. Structure and Phase Transition of BiFeO₃ Cubic Micro-Particles Prepared by Hydrothermal Method. *Mater. Res. Bull.* **2012**, *47* (11), 3630–3636.
- (10) Hou, L.; Lu, Z. Y.; Dai, Y. C.; Zuo, K. H.; Xia, Y. F.; Ren, Z. M.; Wu, J.; Lu, X. G.; Zeng, Y. P.; Li, X. Self-Assembled Growth of BiFeO₃ Meso-Octahedral Particles Synthesized by a Facile Surfactant-Free Hydrothermal Method. *J. Cryst. Growth* **2016**, *434*, 42–46.
- (11) Ponzoni, C.; Rosa, R.; Cannio, M.; Buscaglia, V.; Finocchio, E.; Nanni, P.; Leonelli, C. Optimization of BFO Microwave-Hydrothermal Synthesis: Influence of Process Parameters. *J. Alloys Compd.* **2013**, *558*, 150–159.
- (12) Chen, Y.; Wu, Q.; Zhao, J. Selective Synthesis on Structures and Morphologies of Bi_xFe_yO_z Nanomaterials with Disparate Magnetism through Time Control. *J. Alloys Compd.* **2009**, *487* (1–2), 599–604.
- (13) Wang, Y.; Xu, G.; Ren, Z.; Wei, X.; Weng, W.; Du, P.; Shen, G.; Han, G. Mineralizer-Assisted Hydrothermal Synthesis and Characterization of BiFeO₃ Nanoparticles. *J. Am. Ceram. Soc.* **2007**, *90* (8), 2615–2617.
- (14) Yang, X.; Zhang, Y.; Xu, G.; Wei, X.; Ren, Z.; Shen, G.; Han, G. Phase and Morphology Evolution of Bismuth Ferrites via Hydrothermal Reaction Route. *Mater. Res. Bull.* **2013**, *48* (4), 1694–1699.

- (15) Ruan, Q.; Zhang, W. Tunable Morphology of Bi₂Fe₄O₉ Crystals for Photocatalytic Oxidation. *J. Phys. Chem. C* **2009**, 4168–4173.
- (16) Zhang, X.; Bourgeois, L.; Yao, J.; Wang, H.; Webley, P. A. Tuning the Morphology of Bismuth Ferrite Nano- and Microcrystals: From Sheets to Fibers. *Small* **2007**, 3 (9), 1523–1528.
- (17) Cai, D.; Li, J.; Tong, T.; Jin, D.; Yu, S.; Cheng, J. Phase Evolution of Bismuth Ferrites in the Process of Hydrothermal Reaction. *Mater. Chem. Phys.* **2012**, 134 (1), 139–144.
- (18) Lopes, A. M.; Araujo, J. P.; Ferdov, S. Room Temperature Synthesis of Bi₂₅FeO₃₉ and Hydrothermal Kinetic Relations between Sillenite- and Distorted Perovskite-Type Bismuth Ferrites. *Dalt. Trans* **2014**, 43 (48), 18010–18016.
- (19) Wei, J.; Li, H.; Mao, S.; Zhang, C.; Xu, Z.; Dkhil, B. Effect of Particle Morphology on the Photocatalytic Activity of BiFeO₃ Microcrystallites. *J. Mater. Sci. Mater. Electron.* **2012**, 23 (10), 1869–1874.
- (20) Chen, X. Z.; Qiu, Z. C.; Zhou, J. P.; Zhu, G.; Bian, X. B.; Liu, P. Large-Scale Growth and Shape Evolution of Bismuth Ferrite Particles with a Hydrothermal Method. *Mater. Chem. Phys.* **2011**, 126 (3), 560–567.
- (21) Liu, Y.; Zuo, R. Tunable Morphology and Optical Absorption of Bismuth Ferrite Synthesized by Sol-Gel-Hydrothermal Method. *J. Mater. Sci. Mater. Electron.* **2012**, 23 (12), 2276–2281.

- (22) Yan, D.; Sun, C.; Jian, J.; Sun, Y.; Wu, R.; Li, J. Structure and Phase Transition of BiFeO₃ Particles Prepared by Hydrothermal Method and the Verification of Crystallization–dissolution–crystallization Mechanism. *J. Mater. Sci. Mater. Electron.* **2013**, *25* (2), 928–935.
- (23) De Yoreo, J. J.; Gilbert, P. U. P. A.; Sommerdijk, N. A. J. M.; Penn, R. L.; Whitlam, S.; Joester, D.; Zhang, H.; Rimer, J. D.; Navrotsky, A.; Banfield, J. F.; et al. Crystallization by Particle Attachment in Synthetic, Biogenic, and Geologic Environments. *Science*. **2015**, *349* (6247), aaa6760-aaa6760.

CHAPTER 6

CONCLUSIONS

This thesis begins to make the critical connections between the complex crystalline architectures we can achieve using bio-inspired crystal growth and the effect of that these new types of structuring can have on electromagnetic properties. To do this, throughout this thesis, we apply a physics-based perspective to the field of bio-inspired crystal growth. In doing so, we expand upon current understanding of how new types of complex crystalline architectures, like composite single crystals can be synthesized. (Chapters 2) We then apply this understanding to begin to develop a generalizable method for composite semiconductor/plasmonic nanoparticle nanorod growth (Chapter 3) We also utilize our physics-based perspective to develop a model for how a different type of complex crystalline architecture, that of the mosaic crystal, changes the magnetic interactions of a material. (Chapter 4) To further test our model for the magnetic interactions in mosaic crystals, we synthesized bismuth ferrite and studied its growth pathways, with the goal of growing other types of magnetic mosaic crystals. (Chapter 5) In addition to measuring the magnetic properties of bismuth ferrite crystals, we also measured the magnetic properties of a variety of other (possible) mosaic crystal materials (Appendix 1).

In Chapter 2, we proposed a theoretical framework for the forces at play in the creation of single crystal composites, focusing on particle incorporation into crystals. In short, the crystallization pressure provides a large repulsive force that prevents impurities from incorporating into the crystal. To create single crystal composites, we

must introduce additional forces to counter this repulsive force. Packing particles together or loading them into a template generates normal forces that can be used to oppose the crystallization pressure. Alternatively, attractive intermolecular forces can be introduced to overcome the repulsive crystallization pressure. We shed light on these complex intermolecular interactions, by framing the way they depend on the crystal surface, particle surface and solution chemistry. Our hope is that this framework will give synthetic chemists and materials scientists new perspectives in the design of new functional composite materials.

In Chapter 3, we present the beginnings of a generalizable method for composite nanorod growth. Our approach uses physical confinement to trap arrays of nanoparticles within the pores of track-etched membranes. Then, borrowing concepts from Chapter 4, when we grow crystalline materials in the membrane pores, the particle-particle and particle-membrane pore normal forces oppose the crystallization pressure, allowing for the encapsulation of many nanoparticles into a single crystalline nanorod. This approach had been applied successfully by a previous group member to form Cu_2O nanorods with entrapped Au nanoparticles.¹ In this chapter, we determine the growth mechanism of the Cu_2O in the confinement of the track-etched membrane pores and find that the Cu_2O nanorods form by overgrowth off of bulk crystals. We then apply our understanding of the nanorod growth mechanism to grow ZnO nanorods that can also entrap arrays of Au nanoparticles. While further work is needed to determine the mechanism by which the nanoparticles get stuck during loading into the pores, we did discover a way to tune their dispersion within the nanorod. In our normal synthesis, we largely formed Cu_2O nanorods with “plugs” of Au nanoparticles

that are localized within one region of the nanorod. However, by introducing a prolonged degas step into our synthesis, we can form composite nanorods with dispersed chains of nanoparticles incorporated throughout the length of the nanorod. This work represents the first steps towards a versatile method whereby many new nanoparticle/nanorod pairings can be created.

Future work should continue to grow more nanorod materials in the membrane pores. Specifically, I believe our approach would be simpler if we moved to conventional solution growth methods, rather than vapor diffusion growth, which adds another level of complexity to the growth. Given the wealth of published low temperature syntheses for micrometer-sized solution growth crystals, we should be able to grow a large number of nanorod materials. With our own group's knowledge of conventional zinc oxide solution growth, that would be a rational material to start out with. Another alternative to vapor diffusion growth is to electrodeposit nanorod materials into the membrane pores. Electrodeposition has been successful in generating single crystal composites of ZnO or Cu₂O with incorporated polymer particle packings.²

In order to both increase our efficiency of loading membrane pores with Au nanoparticles and to expand to other nanoparticle materials, we need a better grasp on the ways that concentration, flow rate and solution chemistry (ionic strength and specific ion effects) can aid in clogging pores with particles. Finally, we need a better understanding of the intermolecular forces that allow for the reorganization of nanoparticles during the degas step. We hypothesized that during degassing the particles may become electrostatically stabilized rather than physically packed

together. If that is indeed the case, then we may need to modify our understanding of the types of forces that can oppose the crystallization pressure as we would no longer have traditional normal forces at play.

A long term goal for this work is to change the template for our physical confinement-based approach for composite growth from a track-etched polycarbonate membrane to an anodic aluminum oxide (AAO) membrane. AAO membranes can be easily synthesized in the lab to achieve regular pore densities with tunable pore diameters. Switching to AAO membranes gives us additional temperature stability that will allow us to grow a much wider range of nanorod materials. Finally, commercial polycarbonate membranes are functionalized with secretive proprietary coatings which makes getting a complete picture of the forces involved in crystal growth challenging.

In Chapter 4, we present the mosaic anisotropy model for the magnetic interactions in one type of mesostructured crystalline architecture, the mosaic crystal, which is composed of highly oriented grains separated by small angle grain boundaries. We predict that mosaic crystals will be harder magnets, meaning they have a larger remnant to saturation magnetization ratio (M_r/M_s) and a larger coercive field (H_c), than single crystals or polycrystals. The alignment of the grains in the mosaic crystal should allow for an enhancement of M_r/M_s compared to single crystals or polycrystals, as predicted by studies of textured magnetic materials. Usually this alignment of the grains also causes a decrease in H_c due to exchange coupling between the grains. However, in the mosaic crystal, the presence of small angle grain boundaries between grains allows the grains to be aligned without coupling to one another. Therefore, we predict the mosaic crystals should be harder magnets with

larger M_r/M_s and H_c than single crystals or polycrystals. We validate the hypotheses of our model using a series of hematite ($\alpha\text{-Fe}_2\text{O}_3$) samples. We synthesized and then measured the magnetic properties of hematite single crystals*, mosaic crystals, polycrystals and nanoparticles and found that the mosaic crystals had the largest M_r/M_s and H_c . (*For the single crystal, we used data from the literature.)

Future work should test the applicability of the mosaic anisotropy model for other mosaic crystal systems. The two major challenges to advancing this work are 1) our limited ability to characterize the mosaicity of samples and 2) the complexity of magnetic interactions in nanostructured materials.

The characterization of mosaicity, defined as the degree of misorientation between grains, of micron-sized particles with nanometric grains is difficult as it requires careful tracking of the crystallographic orientation within individual particles. To obtain such information, Dr. Asenath-Smith, a previous member of the Estroff group, developed a new method involving sectioning and TEM imaging and diffraction of individual particles with known geometric orientation.³ Only with this detailed internal structural characterization could we determine with certainty the net crystallographic orientation of the hematite lattice across each mosaic crystal and the degree of crystallographic misorientation between the grains. Unfortunately, both the experimental methods and the interpretation of this data are extremely time consuming, so this is not the kind of routine characterization we would perform on every sample. For larger mosaic crystals with larger grain sizes, it is possible that x-ray diffraction with a narrow beam size could obtain similar information about the net orientation and mosaicity of other potential mosaic crystal materials. Though Dr.

Asenath-Smith synthesized a variety of hematite mosaic crystals during her tenure in the Estroff group, she only characterized the mosaicity of two different growth conditions, one solution-grown and one gel-grown.⁴ The other growth conditions also produce variations to the mosaic crystals we measure in Chapter 4, and from their outward appearance, they seem to have different grain sizes. However, we cannot say for certain that they are mosaic crystals and we have no knowledge of the degree of misorientation between them. If we could synthesize and characterize a series of mosaic crystals with varying degrees of misorientation, we might be able to further refine the mosaic anisotropy model. Currently, the mosaic anisotropy model suggests that there is a “sweet spot” for the degree of misorientation between grains that allows both M_r/M_s and H_c to be enhanced. A set of samples with varying mosaicities could allow us to measure the trade-off between enhanced M_r/M_s due to grain alignment and decreased H_c due to exchange coupling.

We do have information about the net crystallographic orientation and mosaicity of the gel-grown hematite mosaic crystals, which we call quasi-spheres due to their unique shape. Even with this structural information, the magnetic properties of the quasi-spheres are not well-described by the predictions of the mosaic anisotropy model. Due to the complexity of magnetic interactions in nanostructured materials, there seem to be other factors that dominate the magnetic behavior of the gel-grown mosaic crystals over the interactions between the misoriented grains. Part of the complexity of this system comes from the fact that hematite is a highly irregular magnetic material with a canted antiferromagnetic ordering.

Future work, ideally, would grow mosaic crystals of normal ferromagnetic

materials, however, this proves challenging. Ferromagnetic materials are pretty much exclusively metals or alloys, which cannot be grown using the types of solution growth experiments that produce mesostructured crystals. However, some “mesocrystals” are made by assembling pre-formed, functionalized nanoparticles into 3D crystalline structures.⁵⁻⁷ This route for the formation of mesostructured crystals may yield a greater degree of control over the order between grains. We do not know yet, but it is possible that those types of architectures might have magnetic properties well described by the mosaic anisotropy model. Although magnetic interactions are long range, the presence of organic stabilizers at the particle interfaces may play a role in (and actually may impede) the exchange coupling between grains. One caveat of using ordered superstructures of nanoparticles is that typically the sizes of nanoparticles are typically so small that the magnetic properties of the particles may be superparamagnetic instead of ferromagnetic.

Another possibility is to grow ferrimagnetic oxide materials, which have magnetic properties that are more complex than those of the normal ferromagnets, but more straightforward than those of hematite and other canted antiferromagnets. Additionally, some of our knowledge for low to moderate temperature solution crystal growth could be applicable to the growth of these oxide materials. It may take a significant amount of optimization to the synthesis to achieve mosaic crystal architectures.

In Chapter 5, we characterize the growth pathways for the formation of two different bismuth ferrite phases. We found that to form phase-pure samples of BiFeO_3 , high salt concentrations and a prolonged, pre-furnace, room temperature reaction were

required. Without the room temperature reaction step and at low salt concentrations, we form phase-pure samples of $\text{Bi}_2\text{Fe}_4\text{O}_9$. By studying the intermediate products formed after the mixing of reagents as well as after the prolonged room temperature reaction, we can gain insight into why these different growth conditions lead to different final products. We find that a purely amorphous intermediate product later forms $\text{Bi}_2\text{Fe}_4\text{O}_9$, while crystalline $\text{Bi}_{25}\text{FeO}_{40}$ was present in the intermediate product that later forms BiFeO_3 . Interestingly, the BiFeO_3 crystals form as aggregates of faceted subunits, which may or may not be oriented, but it is suggestive of the possibility of mosaic crystal order.

Future work would need to develop a methodology to characterize the (potential) mosaicity of these BiFeO_3 crystals. Our experiments varying the presence or absence of specific spectator ions in solution seemed to suggest that we have some control over the externally apparent degree of order in the crystals. Given the larger size of these crystals, x-ray diffraction-based techniques may be suitable. We did perform some preliminary experiments to determine mosaicity at CHESS in 2017, however, the data has not been analyzed. At first look, it seemed problematic to deconvolute the effects of grain size from the apparent misorientation of the grains in our different BiFeO_3 samples.

In conclusion, the field of bio-inspired crystal growth has developed a wealth of synthetic strategies that can produce some highly unique and unusual crystalline structures. While many of these strategies have been used to produce materials with functional properties, often there are no measurements made or even if there are, the analysis can be superficial. More cross-disciplinary communication and research is

needed for real progress to occur.

REFERENCES

- (1) Asenath-Smith, E.; Noble, J. M.; Hovden, R.; Uhl, A. M.; DiCorato, A.; Kim, Y.-Y.; Kulak, A. N.; Meldrum, F. C.; Kourkoutis, L. F.; Estroff, L. A. Physical Confinement Promoting Formation of Cu₂O–Au Heterostructures with Au Nanoparticles Entrapped within Crystalline Cu₂O Nanorods. *Chem. Mater.* **2017**, *29* (2), acs.chemmater.6b03653.
- (2) Li, X.; Jiang, Y.; Shi, Z.; Xu, Z. Two Growth Modes of Metal Oxide in the Colloidal Crystal Template Leading to the Formation of Two Different Macroporous Materials. *Chem. Mater.* **2007**, *19* (22), 5424–5430.
- (3) Asenath-Smith, E.; Estroff, L. A. Sectioning of Individual Hematite Pseudocubes with Focused Ion Beam Enables Quantitative Structural Characterization at Nanometer Length Scales. *Microsc. Microanal.* **2014**, 1–10.
- (4) Asenath-Smith, E.; Hovden, R.; Kourkoutis, L. F.; Estroff, L. A. Hierarchically Structured Hematite Architectures Achieved by Growth in a Silica Hydrogel. *J. Am. Chem. Soc.* **2015**, *137* (15), 5184–5192.
- (5) Sturm (née Rosseeva), E. V.; Cölfen, H. Mesocrystals: Structural and Morphogenetic Aspects. *Chem. Soc. Rev.* **2016**, *45* (21), 5821–5833.
- (6) Imai, H. Mesostructured Crystals : Growth Processes and Features. *Prog. Cryst. Growth Charact. Mater.* **2016**, *62* (2), 212–226.
- (7) Song, R.-Q.; Cölfen, H. Mesocrystals--Ordered Nanoparticle Superstructures. *Adv. Mater.* **2010**, *22* (12), 1301–1330.

APPENDIX 1

MAGNETIC PROPERTIES OF OTHER MOSAIC CRYSTAL SYSTEMS

A.1 Introduction

In Chapter 4, we proposed the mosaic anisotropy (MA) model to describe the magnetic interactions in mosaic crystals.¹ Briefly, the alignment of grains increases the remnant to saturation magnetization ratio (M_r/M_s) because exchange interactions between neighboring grains keep their magnetic moments aligned even in the absence of a magnetic field.²⁻¹¹ This increase in exchange interactions can also lead to a decrease in the coercive field (H_c) of the magnet, as once one grain flips its magnetization, all the neighboring grains will be quick to follow.^{8,9,18,10-17} To increase H_c , we need to introduce some barriers to fast propagation of magnetization reversal.^{2,6} Therefore, the MA model predicts that the alignment of crystalline grains in the mosaic crystal and the presence of small angle grain boundaries that separate those grains together can yield larger M_r/M_s and larger H_c than for single crystals and polycrystals.

In Chapter 4, we additionally tested the hypotheses of the MA for a series of hematite ($\alpha\text{-Fe}_2\text{O}_3$) samples. We compared the magnetic properties single crystals, mosaic crystals, polycrystals and nanoparticles of hematite and found that the mosaic crystals indeed have the highest M_r/M_s and H_c than any of the other samples. To broaden the applicability of the MA model, here we explore the generalizability and the limitations of the model.

A.2 Refining the MA model – The effect of varying mosaicity

To refine the MA model, we need to explore the behavior of mosaic crystal samples with different degrees of misorientation between the neighboring grains (also called the mosaicity). Currently the MA model suggests that more misorientation between grains (more polycrystal-like) may decrease M_r/M_s while increasing H_c and less misorientation between grains (more single crystal-like) may increase M_r/M_s while decreasing H_c . A series of samples with varying mosaicities will allow us to measure this trade-off and identify the ideal misorientation spread where both M_r/M_s and H_c are highest.

Characterizing the mosaicity of micron-sized crystals with nanoscale grains is a great challenge. Previous work from our group developed methods to use a focused ion beam to create thin sections of known geometric orientation from within single mosaic crystals.¹⁹ When these thin sections are imaged in a TEM and electron diffraction is performed, we can learn the net crystallographic orientation across the mosaic crystal as well as the mosaicity of the sample. Due to the time intensive nature of the sample preparation, data collection and analysis, we only have mosaicity data for two different types of hematite mosaic crystals, a solution-grown pseudocube sample and a gel-grown quasisphere sample.^{19,20} However, we know that varying other aspects of the hematite mosaic crystal growth, like the $[Fe^{3+}]$ or the amount of Si in the growth environment (determined by whether a PTFE or borosilicate glass growth vessel is used), change the “apparent mosaicity.” The apparent order of the grains at the surface is a poor proxy for the internal order, so here we only present data for hematite samples that we know something about their mosaicity.

A.2.1. Gel-grown mosaic crystals (quasispheres)

We first consider the magnetic properties of the one other hematite mosaic crystal for which we do know the mosaicity, the gel-grown quasi-sphere. (Fig A.1a) When hematite mosaic crystals form in a silica hydrogel, their growth is modified across many length scales.²⁰ For example, silicon from the hydrogel incorporates into the hematite lattice as interstitial Si. The incorporation of Si causes the individual grains of the gel-grown mosaic crystal to become elongated along the [110] hematite axis, whereas they are slightly elongated along the [001] for the solution-grown mosaic crystal. These elongated [110]-oriented grains then pack radially to ultimately form the quasisphere shape. (Fig. A.1c) When the quasispheres are sectioned and electron diffraction performed, we again see a single crystal-like diffraction pattern from which we can calculate the mosaicity of 1.9-6.6°, depending on the crystallographic plane. (Fig. A.1b, inset) For reference, the mosaicity for the pseudocubes studied in Chapter 4 was 4.3-12.8°.¹⁹

Field-dependent magnetization measurements of the quasispheres show a hysteresis loop that is constricted near zero field, which is known as a wasp-waisted hysteresis loop. The quasisphere has $M_r = 0.21$ emu/g and $H_c = 61$ Oe. (Fig. A.1c) Temperature-dependent magnetization measurements reveal no change in the magnetization down to 2K. (Fig. A.1d)

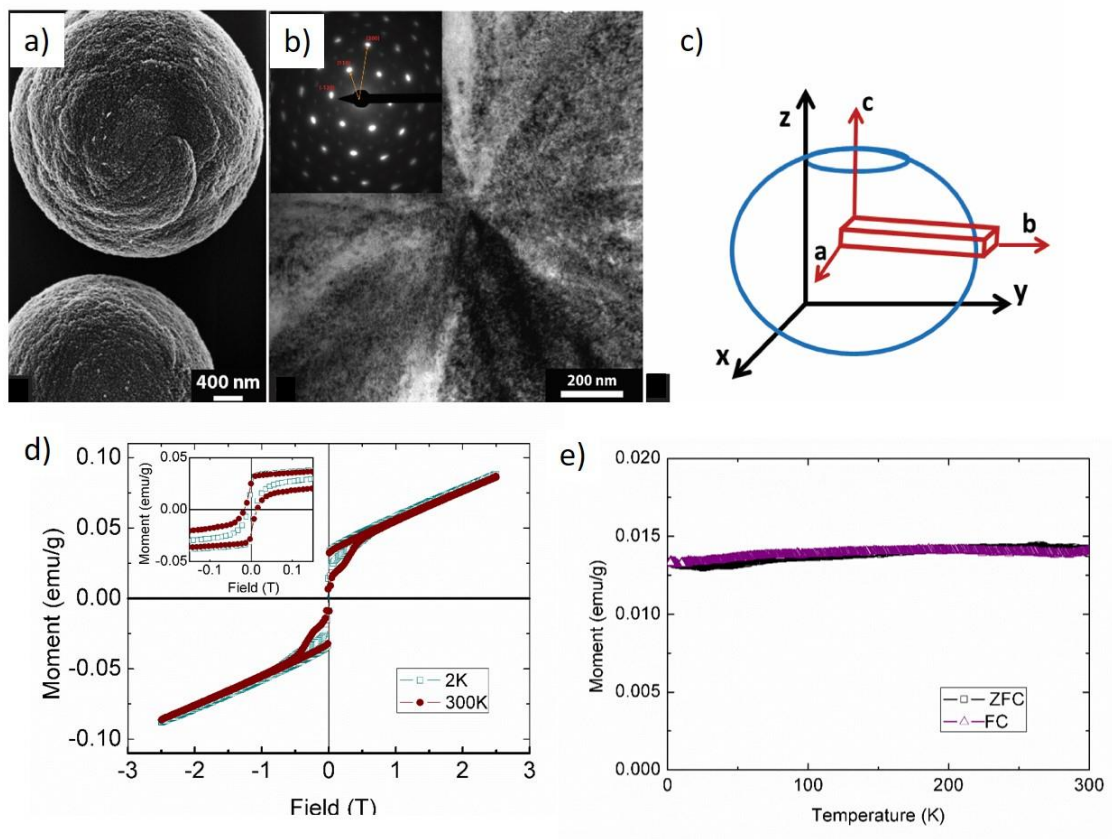


Figure A1. (a) SEM of gel-grown mosaic crystals that form spherical particles with flat tops and bottoms, hence we call them quasispheres (b) Bright field TEM and electron diffraction (inset) of a thin slice from a known orientation within the quasisphere reveals a single crystal-like diffraction pattern, from which mosaicity can be calculated. (c) Schematic for the crystallographic arrangement of grains elongated along the b axis, which form the quasisphere mosaic crystal. Reprinted (adapted) with permission from Asenath-Smith, E.; Hovden, R.; Kourkoutis, L. F.; Estroff, L. A. Hierarchically Structured Hematite Architectures Achieved by Growth in a Silica Hydrogel. *J. Am. Chem. Soc.* **2015**, 137 (15), 5184–5192.. Copyright 2015 American Chemical Society. (d) Field-dependent magnetization measurements at 300K and 2K show a wasp-waisted hysteresis loop at both temperatures, meaning the hysteresis loop looks constricted near the origin. (e) Temperature-dependent magnetization measurements show that the Morin transition is completely suppressed in the quasispheres.

Overall, we still do not know how to interpret the magnetic properties of the gel-grown quasispheres of hematite. The one element of the MA model that seems consistent with our measurement of the magnetic properties of the quasispheres is that we see a smaller amount of misalignment (lower mosaicity) as well as a much smaller coercive field than for the pseudocubes (Table A.1).

There are many features of the quasisphere magnetic behavior we do not understand. For example, the magnitude of the magnetic moment for the gel-grown quasispheres is an order of magnitude lower than that of the solution-grown pseudocubes. Wasp-waisted hysteresis loops have been seen for nanostructured mixed hard-soft systems.^{14,21} We do not know if we see wasp-waisted behavior for these same reasons and if so, we do not quite know what the two “components” are. We can posit several possible explanations for why the crystallographic order of the quasispheres differs so significantly from that of the pseudocubes. Magnetic properties are highly sensitive to shape anisotropy, such that magnetic moments often prefer to align with the longer direction.²² Additionally, the crystallographic orientation along which the grains of the pseudocubes and quasispheres are elongated are different, [001] and [110] respectively. In bulk hematite, due to the canted antiferromagnetic order, the net magnetic moment points along the [001] crystallographic direction, known as the easy axis. Therefore, we hypothesize that there is some competition between the magnetic moments that want to align with the elongated axis of the grains [110] and the magnetic moments that want to align with the easy axis [001]. This competition could contribute both to the overall reduced net magnetization due to

cancellation and could also possibly explain the two “components” we see in the wasp-waisted hysteresis loop.

A.1.2.2 Acid-etched, gel-grown mosaic crystals

Additionally, as part of her study to understand their growth, Dr. Asenath-Smith performed etching experiments, where pseudocubes or quasispheres were immersed in a dilute acid (HCl) solution and gently spun on a rotating agitator for one month.²⁰

Gentle etching in an acidic solution is presumed to preferentially dissolve the more soluble, less stable regions of the crystal, so in the case of mosaic crystals, we assume that the small angle grain boundary areas dissolve preferentially. After one month, the quasispheres have become porous, though they have not lost their single-crystal like nature (Fig. A.2a,b). The pseudocubes were exposed to identical etching conditions, but there was very little change to their appearance (not shown).

We measure the field- and temperature-dependent magnetic properties of the acid-etched quasispheres and see dramatically different hysteresis behavior (Fig. A.2c). The hysteresis loop is no longer wasp-waisted and it is much squarer in shape. The coercivity of the acid-etched quasispheres is 5.2 kOe, which is not only an order of magnitude larger than the as-grown quasispheres, but it is also larger than that of the solution grown pseudocubes (Table A.1)

Upon etching, the remnant magnetization of the quasisphere sample decreases by an order of magnitude (from 0.21 to 0.04 emu/g). We do not calculate M_r/M_s ratios for the quasisphere samples because when we follow our method described in Ch. 4 for calculating the antiferromagnetic susceptibility of the sample, we find a value for the

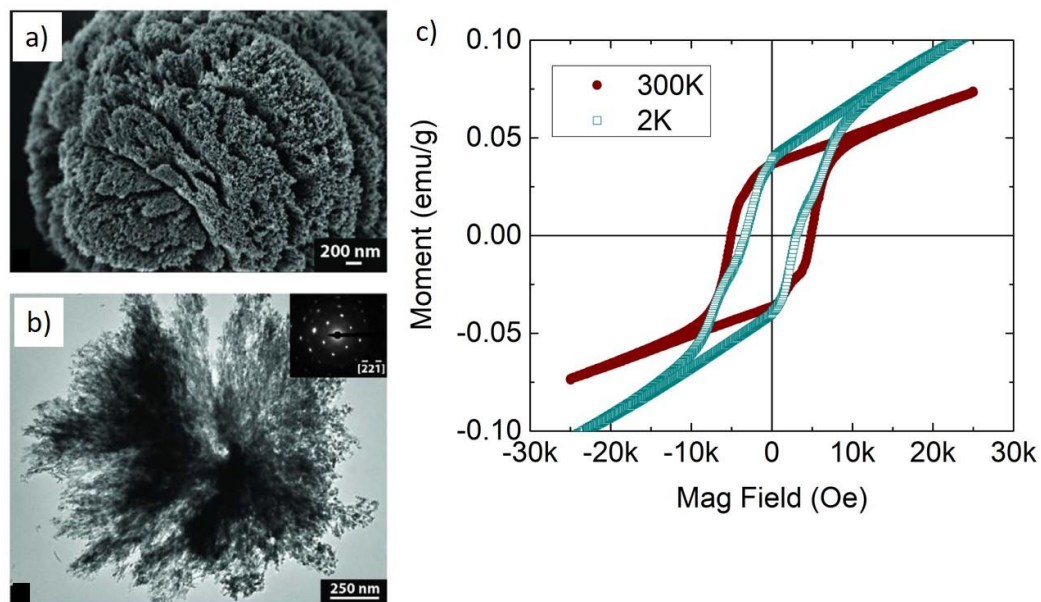


Figure A1.2 (a) SEM of acid-etched gel-grown mosaic crystals reveals that selective etching has caused porosity. (b) TEM of the acid-etched, gel-grown crystal also reveals the extent of the etching, but electron diffraction (inset) shows that it is still single crystal-like. Reprinted (adapted) with permission from Asenath-Smith, E.; Hovden, R.; Kourkoutis, L. F.; Estroff, L. A. Hierarchically Structured Hematite Architectures Achieved by Growth in a Silica Hydrogel. *J. Am. Chem. Soc.* **2015**, 137 (15), 5184–5192.. Copyright 2015 American Chemical Society. (c) Field-dependent magnetization measurements at 300K and 2K reveal an open hysteresis loop that is distinctly different from that of the un-etched gel-grown mosaic crystals (Fig A1.1d).

quasispheres that differs from that of “normal” hematite and instead is more similar to that of nanoparticle hematite (Table 4.S1). We can’t compare the unnormalized remnant magnetization values between the samples, so we don’t have any good explanation for the small value of M_r for the acid-etched quasispheres compared to the as-grown crystals.

We have not calculated the mosaicity of the acid-etched quasispheres, but we would presume that the degree of misorientation between grains does not change during etching. What has changed is the nature of the interaction between those grains. It could be that by removing the small angle grain boundaries of the quasisphere mosaic crystal we impeded the exchange coupling between the grains and thus increased the coercivity. But questions remain about the nature of the grain boundaries in the quasispheres that enabled exchange coupling between grains, while the grain boundaries in the pseudocubes seem not to.

Table A.1. Magnetism data for other mosaic crystals of hematite

Sample	M_s (emu/g)	M_r (emu/g)	M_r/M_s	H_c (kOe)	Slope in the high field region (emu/g/Oe)
Pseudocubes	0.280	0.24	0.85	4.3	0.1814
Gel-grown quasispheres	Not calculated	0.21	Not calculated	0.6	0.1611
Acid-etched gel-grown quasispheres	Not calculated	0.04	Not calculated	5.2	0.1631

REFERENCES

- (1) Goldman, A. R.; Asenath-smith, E.; Estroff, L. A.; Goldman, A. R.; Asenath-smith, E.; Estroff, L. A. Mosaic Anisotropy Model for Magnetic Interactions in Mesostructured Crystals Mosaic Anisotropy Model for Magnetic Interactions in Mesostructured Crystals. *APL Mater.* **2017**, *104901* (5).
- (2) Legrand, A.; Chateigner, D. Orientation by Solidification in a Magnetic Field A New Process to Texture SmCo Compounds Used as Permanent Magnets. *J. Magn. Mater.* **1997**, *173*, 20–28.
- (3) Khlopkov, K.; Gutfleisch, O.; Hinz, D.; Müller, K. H.; Schultz, L. Evolution of Interaction Domains in Textured Fine-Grained Nd₂Fe₁₄B Magnets. *J. Appl. Phys.* **2007**, *102*, 023912.
- (4) Huy, N.; Thi, P.; Hai, N.; Thi, N.; Huyen, T. Inducing Anisotropy in Bulk Nd – Fe – Co – Al – B Nanocrystalline Alloys by Quenching in Magnetic Field. *J. Magn. Mater.* **2012**, *324* (7), 1435–1439.
- (5) Yan, A.; Zhang, W.; Zhang, H.; Shen, B. Melt-Spun Magnetically Anisotropic SmCo Ribbons with High Permanent Performance. *J. Magn. Mater.* **2000**, *210*, 10–14.
- (6) Zhang, T.; Liu, H.; Ma, Z.; Jiang, C. Single Crystal Growth and Magnetic Properties of 2 : 17-Type SmCo Magnets. *J. Alloys Compd.* **2015**, *637*, 253–256.
- (7) Zhang, D.; Yuan, X.; Yue, M.; Zhou, D.; Zhu, J.; Gao, X. Crystallographic Orientation-Dependent Magnetic Properties of a PrCo₅ Permanent Magnet Prepared by Hot Deformation. *CrystEngComm* **2016**, *18*, 2632–2641.
- (8) Crew, D. C.; Lewis, L. H. Effect of Grain Alignment on Magnetic Structure in Nanoscale Material. *IEEE Trans. Magn.* **2001**, *37* (4), 2512–2514.
- (9) He, S.; Zhang, H.; Rong, C.; Chen, R. Studies on the Magnetic Properties for Single-Phase Nanocrystalline FePt Magnets with Different Orientation Degrees. *J. Magn.* **2007**, *312*, 1–5.
- (10) Yao, Q.; Liu, W.; Zhang, Z. D. Effective Anisotropy Field in Anisotropic Nanostructured Ferromagnetic Materials. *Phys. Status Solidi* **2009**, *1715* (7), 1709–1715.
- (11) Jin, Y. M.; Wang, Y. U.; Kazaryan, A.; Wang, Y.; Laughlin, D. E. Magnetic Structure and Hysteresis in Hard Magnetic Nanocrystalline Film : Computer Simulation. *J. Appl. Phys.* **2002**, *92* (10), 6172–6181.
- (12) Kneller, E. F.; Hawig, R. The Exchange-Spring Magnet: A New Material Principle for Permanent Magnets. *IEEE Trans. Magn.* **1991**, *27* (4), 3588–3600.
- (13) Skomski, R. Giant Energy Product in Nanostructured Two-Phase Magnets. *Phys. Rev. B* **1993**, *48* (21), 15812–15816.

- (14) Skomski, R.; Manchanda, P.; Takeuchi, I. Geometry Dependence of Magnetization Reversal in Nanocomposite Alloys. **2014**, *66* (7), 1144–1150.
- (15) Fischer, R.; Schrefl, T.; Kronmüller, H.; Fidler, J. Grain-Size Dependence of Remanence and Coercive Field of Isotropic Nanocrystalline Composite Permanent Magnets. *J. Magn. Magn. Mater.* **1996**, *153* (1–2), 35–49.
- (16) Cui, W.; Takahashi, Y. K.; Hono, K. Nd₂Fe₁₄B / FeCo Anisotropic Nanocomposite Films with a Large Maximum Energy Product. *Adv. Mater.* **2012**, *24*, 6530–6535.
- (17) Quesada, A.; Granados-Miralles, C.; López-Ortega, A.; Erokhin, S.; Lottini, E.; Pedrosa, J.; Bollero, A.; Aragón, A. M.; Rubio-Marcos, F.; Stingaciu, M.; et al. Energy Product Enhancement in Imperfectly Exchange-Coupled Nanocomposite Magnets. *Adv. Electron. Mater.* **2016**, *2* (4), 1500365.
- (18) Hernando, A. Exchange Interactions and Coercivity in Multi-Phase Magnets. *J. Magn. Magn. Mater.* **1992**, *117* (1–2), 154–162.
- (19) Asenath-Smith, E.; Estroff, L. A. Sectioning of Individual Hematite Pseudocubes with Focused Ion Beam Enables Quantitative Structural Characterization at Nanometer Length Scales. *Microsc. Microanal.* **2014**, 1–10.
- (20) Asenath-Smith, E.; Hovden, R.; Kourkoutis, L. F.; Estroff, L. A. Hierarchically Structured Hematite Architectures Achieved by Growth in a Silica Hydrogel. *J. Am. Chem. Soc.* **2015**, *137* (15), 5184–5192.
- (21) Roberts, A. P.; Cui, Y.; Verosub, K. L. Wasp-Waisted Hysteresis Loops: Mineral Magnetic Characteristics and Discrimination of Components in Mixed Magnetic Systems. *J. Geophys. Res.* **1995**, *100* (B9), 17909–17924.
- (22) Master, O.; In, S.; Matter, C. Magnetism in Condensed Matter.